POLITECNICO DI TORINO

Master's Degree in Mechanical Engineering



Master's Degree Thesis

Bridging numerical and experimental modal analysis: experimental validation of a spindle dynamic model for high-precision applications

Supervisors

Prof. Alessandro FASANA

Industrial Supervisor

Ing. Angelico APPROSIO

Candidate

Daniele ACCOTO

A.Y. 2025/2026

A mio fratello Roberto,
per avermi insegnato l'arte dell'impegno, della dedizione
e che grandi sacrifici portano grandi risultati.
A mamma Enza e papà Savio,
per aver fatto l'impossibile per realizzare ogni mio desiderio
e per avermi strigliato e motivato, sempre.
A Fabiana,
per avermi guidato con saggezza,
per essere stata la mia spalla e il mio riferimento,
ma, soprattutto,
per avermi inondato d'amore puro dal primo giorno.

Summary

This thesis validates a numerical model of high precision spindle assemblies, focusing on the challenges that arise when several mechanical components interact within an integrated system. While numerical modal analysis is reliable for isolated parts, significant discrepancies appear when analysing full spindle assemblies, especially in axial modes or in configurations with preload and floating bearings. These differences stem from an incomplete representation of bearing–housing boundary conditions in n the tools dedicated to numerical dynamic analysis, as for example, SKF SimPro Spindle. Since bearing stiffness strongly affects the eigenstructure and the Campbell diagrams, inaccurate constraint modelling reduces the reliability of numerical predictions. This issue is relevant for industry, where numerical tools are increasingly expected to reduce or replace time consuming experimental modal tests. Impact based experimental modal analysis requires specialised equipment and must be repeated for each configuration, whereas a validated model capable of reproducing locating and non locating bearing behaviour would enable more efficient virtual prototyping and faster product iterations. The main objective is to establish physically consistent boundary conditions between numerical and experimental models. Additional goals include tuning the numerical model based on test evidence and extracting the operating deflection shape during rotation to validate the stationary response. The methodology combines roving hammer tests with PCB accelerometers, instrumented hammers and the SQuadriga acquisition system, supported by fixtures approximating free–free conditions. Modal parameters were extracted through ArtemiS Suite. In parallel, numerical analyses were performed using SKF SimPro Spindle and SKF SimPro Expert, which implement Component Mode Synthesis and elastohydrodynamic contact formulations. A hierarchical modelling strategy was adopted, studying single components first, then sub assemblies and finally the full spindle. This approach clarified the contribution of each element to the global dynamic response and helped localise the source of mismatches. Results show that numerical predictions are accurate for simple geometries, with deviations below 10%. However, as assembly complexity increases, assuming a fixed boundary for a bearing that behaves as free or floating introduces artificial stiffness and shifts axial modes. Correcting this assumption

leads to a much closer agreement with experimental data and produces a more realistic representation of the system dynamics. Overall, the work shows that while the modal behaviour of individual parts is straightforward, the dynamics of assembled systems are dominated by component interactions, preload conditions and mounting strategies. These aspects represent the main challenge in modelling. Through iterative testing and simulation, the thesis clarifies how bearing boundary conditions must be modelled to obtain accurate predictions. Although developed in a proprietary environment, the methodology is general and applicable to other mechanical systems, such as electric motors, where internal clearances and constraint strategies similarly affect dynamic behaviour. The results highlight how accurate boundary modelling significantly enhances prediction robustness and supports a more reliable virtual design process.

Acknowledgements

Desidero esprimere la mia sincera gratitudine ai miei supervisori, il professore Alessandro Fasana e l'ingegnere Angelico Approsio, per la loro preziosa guida e disponibilità durante tutto il percorso di stesura di questa tesi.

A Sofia, amica sincera e leale. Grazie per aver condiviso con me tanti momenti, pranzi, cene, caffè ma soprattutto per essere stata una persona con cui potermi confrontare senza filtri o paura di essere giudicato.

A Speppo, Luigia, Mattia Stirato, Mattia Giaccaglia, Luigia, Riccardo De Matteis, Riccardo Antolino, Mattia Fasiello, Maicol e tutti gli amici e amiche del terzo piano Crocetta. Un grazie di cuore per aver fatto parte della mia quotidianità, per le vacanze, uscite serali, Carmen, Santa Giulia, pranzi e cene. Vi ringrazio per avermi accettato, incluso e fatto sentire parte di una grande famiglia nonostante tutti i miei difetti. A Roberto, Matteo e tutti gli amici e amiche del quarto piano Po, grazie per avermi integrato e subito fatto sentire uno di voi. Vi porterò per sempre nel mio cuore e vi auguro di realizzare tutti i vostri sogni e desideri.

A **Luca**, *Il porco*, grazie per avere illuminato la mia vita con la tua intelligenza, profondità e passione. Grazie per avermi polarizzato risvegliando la mia curiosità in tanti ambiti della vita, grazie per tutte le partite di calcetto che hai giocato con me, per tutte le partite viste in diretta sul tablet in cucina, le analisi tattiche sulla lavagna e le feste in grande stile alla Po. Continua ad essere la persona d'oro che sei, la tua passione, motivazione e brillantezza ti consentiranno di realizzare il tuo sogno. Grazie soprattutto per avermi insegnato quali sono i principi della vita e a gestire il tempo, identificando quali attività sono effettivamente inutili (pulire, ad esempio), perchè *"solo chi ha tempo da perdere può perdere tempo"*.

IL PORCO É IL PORCO, TU SEI TU

Al **VATE 32**, grazie per essere stata la prima persona in assoluto ad avermi accolto già dal primo giorno a Torino. Mi hai fatto sempre sentire apprezzato e non mi hai mai fatto mancare nulla come solo un vero padre sa fare. Grazie per condiviso con me letteralmente tutto: colazioni, pranzi, cene, feste, momenti no,

partite di calcetto, vacanze, letto e soprattutto viaggi in macchina. Grazie per l'energia che hai portato, porti e porterai nella mia vita, per la tua instancabile positività e spiccata intelligenza. Grazie per avermi insegnato IL metodo di studio: studiare tutto solo in sessione. Grazie per tutti i souvatir e per rendere ogni esperienza indimenticabile. Grazie per essere la nostra ancora di salvezza con le tue Vatemove e per ultimo, ma non importanza, grazie per essere IL VATE.

DOPO IL 3 C' É SEMPRE IL 2

A **Vinz**, il mio compagno di avventure. Grazie per aver condiviso tanto con me, per avermi incluso in ogni cosa che hai organizzato senza nemmeno chiedermi se fossi disponibile, tanto *"non hai mai un cazzo da fare, mo vedi tu se stasera devi fare altro"*. Grazie per tutte le vacanze che hai organizzato minuziosamente (in Puglia, a NY, in Sicilia, Toscana etc etc), capodanno, pasquetta e soprattutto per avermi fatto conoscere da vicino la tribù abruzzese. Grazie per tutte le colazioni romantiche alle 7:30 di mattina da soli in cucina in collegio, per tutti i pranzi, le cene, i dolci di tua madre, i caffè nespresso, starbucks e tutte le stirate. Grazie per avermi fatto riscoprire il fascino del power nap post pranzo e l'importanza di leggere le descrizioni dei quadri nei musei. Grazie soprattutto per essere un amico vero, sincero, con il cuore grande e sempre presente. Sono sicurissimo che con la tua determinazione, intelligenza e metodo riuscirai a diventare l'ingegnere elettrico migliore del mondo - anche perchè sei l'unico. Per ultimo ma non per importanza, grazie per avermi insegnato la Vinzmove dei resi su Amazon, ma soprattutto che

NON SI STIRA MAI

A **Piero**, infintamente grazie per essere stata la persona con cui ho trascorso ogni singolo attimo della mia vita torinese, il mio braccio destro e il mio complice. Grazie per avere la capacità di comprendermi in una frazione di secondo con uno sguardo, senza bisogno di parole. Senza di te questi 5 anni e mezzo non sarebbero mai stati gli stessi, abbiamo fatto di tutto e ogni tanto abbiamo anche studiato (da mezzanotte alle cinque di mattina in aula studio a -1 a crocetta). Grazie per tutte le volte che mi hai accompagnato a prendere il gelato da Giovanni e abbiamo fatto un'ora di fila con 40 gradi all'ombra, grazie per tutte le partite di calcetto che abbiamo giocato e che abbiamo visto insieme allo stadio (sia San Siro, sia allo stadio del Toro). Grazie per aver creato con me la coppia più amata e temuta in Collegio e per essere stato la mente, il braccio e complice di scherzi epici. Grazie per essere stato, insieme a me, CEO & Co-founder del VATE 32 e per aver creato una nuova lingua. Grazie per aver allietato le sessioni di studio più intense e disperate con la tua creatività, gioia e intelligenza. Rimani sempre la persona speciale che sei, dolce, gentile ed eccellente. Sono convinto che le tua genialità, la tua motivazione e passione ti consentiranno di realizzarti in ogni ambito della vita quotidiana e professionale. Grazie anche per avermi fatto sentire al sicuro anche quando tutto intorno tremava.

TRENTADUE E SIAMO OTTIMIIIIIII

Table of Contents

List of Tables xiii

List of Figures xv

Acronyms xx

1 Introduction 1

2 Numerical model of the spindle 3
2.1 General Information and Current State of the Tool 3
2.2 Problem Statement 3
2.3 Need for Additional Study and Validation 4
2.4 Expected Outcome 6
2.5 Validation 6
2.6 Expected Outcomes and Further Actions 6

3 Overview of the investigated model 7
3.1 Stator 7
3.2 Rotor 9

4 Experimental Setup for Modal Analysis 15
4.1 Modal Analysis: principles, applications, and validity conditions . . 15
4.2 Industrial Applications 15
4.3 Benefits of Modal Analysis 16
4.4 Conditions for the Validity of Modal Analysis 16
4.4.1 Theoretical Assumptions 16
4.4.2 Experimental Requirements 17
4.4.3 Signal Processing and Data Acquisition 17
4.4.4 Data Consistency 18
4.4.5 Validation Criteria 18
4.5 Parameter Estimation Techniques 18

4.6 Real vs Complex Modes . . . 19
4.7 Correlation with Analytical Models . . . 19
4.8 Experimental Setup . . . 19
4.8.1 Support Configuration . . . 19
4.8.2 Instrumentation and Data Acquisition . . . 21

5 Results of the Experimental modal analysis 28
5.1 Shaft . . . 29
5.2 Shaft Accessories . . . 31
5.3 Rotating components . . . 32
5.3.1 Radial vibrations . . . 33
5.3.2 Axial vibrations - Da Capire se mettere o meno . . . 34
5.4 Casing . . . 36
5.5 Spindle assembly . . . 38
5.5.1 Radial vibrations . . . 38
5.5.2 Axial vibrations . . . 40
5.6 Decoupling the shaft and casing motion . . . 42
5.6.1 Radial vibrations . . . 42
5.6.2 Axial vibrations . . . 49
5.7 Spindle in rotation . . . 55
5.7.1 Campbell diagram . . . 57
5.7.2 Operating deflection shapes . . . 59

6 Numerical modeling of the case study 62
6.1 Introduction . . . 62
6.2 Governing Equations of the System . . . 63
6.3 Contact Mechanics . . . 63
6.3.1 Hertzian Elastic Contact . . . 63
6.3.2 Elastohydrodynamic Lubrication . . . 64
6.3.3 Dimensionless EHL Stiffness Model . . . 64
6.3.4 Viscous Damping in the Lubricated Contact . . . 65
6.4 Geometrical Imperfections and Waviness . . . 65
6.4.1 High-Order Waviness . . . 66
6.5 Component Mode Synthesis for Bearings . . . 66
6.5.1 Limitations of Classical CMS . . . 66
6.5.2 SKF Analytical CMS Method . . . 66
6.6 Matrix Formulation of Component Mode Synthesis . . . 67
6.7 Schematic Representation of the CMS Method . . . 68
6.7.1 Mode Decomposition in CMS . . . 68
6.7.2 Moving Contact Loads and Analytical Shape Functions . . . 69
6.8 Local Defects and Indentations . . . 69

6.9 Hybrid Bearings and Large Ball Sets . . . 69
6.10 Linearisation, Modal Analysis and Transient Simulation . . . 70
6.11 Conclusion . . . 70

7 Results of the numerical modal analysis 71
7.1 Shaft . . . 72
7.1.1 Beam shaft . . . 75
7.1.2 Fourier shaft . . . 76
7.2 Shaft accessories . . . 76
7.3 Rotating components . . . 78
7.3.1 Beam shaft . . . 78
7.3.2 Fourier shaft . . . 79
7.3.3 Fourier shaft with connection on the side surfaces of bearings inner rings . . . 80
7.4 Casing . . . 81
7.5 Spindle assembly . . . 81
7.6 Spindle in rotation . . . 83
7.6.1 Beam shaft . . . 83
7.6.2 Fourier shaft . . . 85

8 Comparison between experiments and numerical model 87
8.1 Introduction . . . 87
8.2 Shaft . . . 88
8.3 Shaft accessories . . . 90
8.4 Rotating components . . . 94
8.5 Casing . . . 97
8.6 Spindle assembly . . . 99
8.7 Spindle in operation . . . 102
8.8 Overall assessment . . . 106

9 Future developements 108

10 Conclusions 112

A Geometrical characterization of the components 115
A.1 Ring . . . 115
A.2 Bearing . . . 116
A.3 Bezel . . . 117
A.4 Bushing . . . 118
A.5 Flange . . . 119
A.6 Spring . . . 120
A.7 Shaft . . . 121

A.8 Casing 122
A.8.1 Cup 122
A.8.2 Cylinder 122
A.8.3 Electric Motor 123

Bibliography 125

List of Tables

4.1 Industrial sectors and their applications of modal analysis 16
4.2 Performance parameters PCB 352A25 22
4.3 Physical Characteristics PCB 352A25 22
4.4 Performance parameters KS78C 23
4.5 Physical Characteristics of KS78C100 Accelerometer 23
4.6 Performance Parameters PCB 086E80 24
4.7 Physical Characteristics PCB 086E80 24
4.8 Performance Parameters PCB 086C03 25
4.9 Physical Characteristics PCB 086C03 25

5.1 Modal parameters of the shaft 31
5.2 Modal parameters of the bezel 32
5.3 Modal parameters of the bushing 32
5.4 Modal parameters of the ring 32
5.5 Modal parameters of the rotating components - radial vibrations . . 34
5.6 Modal parameters of the rotating components - axial vibrations . . 36
5.7 Modal parameters of the casing 38
5.8 Modal parameters of the spindle - radial vibrations 40
5.9 Modal parameters of the spindle - axial 42
5.10 Modal parameters of the spindle - Casing to casing - radial 44
5.11 Modal parameters of the spindle - Casing to shaft - radial 46
5.12 Modal parameters of the spindle - Casing to shaft - radial 47
5.13 Modal parameters of the spindle - Casing to shaft - radial 49
5.14 Modal parameters of the spindle - Casing to casing - axial 50
5.15 Modal parameters of the spindle - Casing to shaft - axial 52
5.16 Modal parameters of the spindle - Casing to shaft - axial 54
5.17 Modal parameters of the spindle - Casing to shaft - axial 55
5.18 Operating Deflection Shape - radial 60
5.19 Operating Deflection Shape - axial 61

7.1 Material properties 72

7.2 Modal parameters of the beam shaft 76
7.3 Modal parameters of the Fourier shaft 76
7.4 Modal parameters of the bezel 77
7.5 Modal parameters of the bushing 77
7.6 Modal parameters of the ring 78
7.7 Modal parameters of the shaft and rotating components - beam model 79
7.8 Modal parameters of the shaft and rotating components - Fourier model 80
7.9 Modal parameters of the shaft and rotating components - Fourier model with connection 80
7.10 Modal parameters of the casing 81
7.11 Modal parameters of the spindle assembly - Fourier shaft 83
7.12 Operating deflection shapes - beam shaft model 85
7.13 Operating deflection shapes - Fourier shaft model 86

8.1 Experimental and numerical modal parameters of the shaft 88
8.2 Experimental and numerical modal parameters of the ring 91
8.3 Experimental and numerical modal parameters of the bushing . . . 91
8.4 Experimental and numerical modal parameters of the bezel 92
8.5 Experimental and numerical modal parameters of the shaft and accessories 94
8.6 Experimental and numerical modal parameters of the casing 97
8.7 Experimental and numerical modal parameters of the spindle assembly 99
8.8 Experimental and numerical modal parameters of the spindle at 0 rpm 103
8.9 Experimental and numerical modal parameters of the spindle at 60000 rpm 103

A.1 Geometrical and Physical Specifications of the Ring (NDE) 116
A.2 Geometrical and Physical Specifications of the Bearing 117
A.3 Geometrical and Physical Specifications of the Bezel 118
A.4 Geometrical and Physical Specifications of the Bushing 119
A.5 Geometrical and Physical Specifications of the Flange 120
A.6 Geometrical and Physical Specifications of the Cup 122
A.7 Geometrical and Physical Specifications of the Electric Motor . . . 123

List of Figures

2.1 An example of a support group containing four bearings 4
2.2 Examples of a locating and non-locating support group 4
2.3 The support on the right side is non-locating 5
2.4 Campbell diagram of a locating vs. the non-locating arrangement . 5

3.1 Front view of the housing 7
3.2 Top view of the housing 7
3.3 Top view of the cup 8
3.4 Front view of the cup 8
3.5 Front view of the housing 8
3.6 Top view of the housing 8
3.7 Electric motor 9
3.8 Aluminum shaft 9
3.9 Bearing section 10
3.10 Front view of the bushing 10
3.11 Side view of the bushing 10
3.12 Bezel - front view 11
3.13 Bezel - side view 11
3.14 Bezel - back view 11
3.15 Flange - front view 11
3.16 Flange - side view 11
3.17 Flange - back view 11
3.18 Ring - front view 12
3.19 Ring - side view 12
3.20 Spring disc 12
3.21 Ring 12
3.22 Characteristic line of the springs 13
3.23 Shaft and rotating components 14

4.1 Foam support for the shaft 20
4.2 Foam support for the rotating components 20

4.3 Two different experimental setup 20
4.4 Support for the rotation of the spindle 21
4.5 PCB 352A25 accelerometer 21
4.6 KS78C Accelerometer 23
4.7 PCB 086E0 impulse hammer 24
4.8 PCB 086C03 impulse hammer 25
4.9 Excitation range for different Tips 26
4.10 SQuadriga III 26

5.1 Experimental setup - Shaft 30
5.2 Measured transfer functions - Shaft 30
5.3 Transfer function and stability - Shaft 31
5.4 Experimental setup - Shaft and accessories - radial vibrations . . . 33
5.5 Measured transfer functions - Shaft and accessories - radial vibrations 33
5.6 Transfer function and stability diagram - Shaft and accessories - radial vibrations 34
5.7 Measured transfer function - Shaft and accessories - axial vibrations 35
5.8 Transfer function and stability diagram - shaft and accessories - axial vibrations 35
5.9 Experimental setup casing radial vibrations 36
5.10 Measured transfer functions - Casing 37
5.11 Transfer function and stability diagram - Casing 37
5.12 Experimental setup - Spindle - radial vibrations 38
5.13 Measured transfer functions - Spindle - radial vibrations 39
5.14 Transfer function and stability diagram - Spindle - radial vibrations 39
5.15 Experimental setup - Spindle - axial vibrations 40
5.16 Measured transfer functions - Spindle - axial vibrations 41
5.17 Transfer function and stability diagram - Spindle - axial vibrations . 41
5.18 Sensors placement on the casing in the radial direction 43
5.19 Measured transfer functions - Casing to casing - radial vibrations . 43
5.20 Transfer function and stability diagram - Casing to casing - radial vibrations 44
5.21 Sensors placement on the shaft in the radial direction 44
5.22 Measured transfer functions - Casing to shaft - radial 45
5.23 Transfer function and stability diagram - Casing to shaft - radial direction 45
5.24 Measured transfer functions - Shaft to casing - radial direction . . . 46
5.25 Transfer function and stability diagram - Shaft to casing - radial . . 47
5.26 Measured transfer functions - shaft to shaft - radial 48
5.27 Transfer function and stability diagram - shaft to shaft - radial . . . 48
5.28 Sensors placement on the casing in the axial direction 49

5.29 Measured transfer functions - Casing to casing - axial vibrations . . 49
5.30 Transfer function and stability diagram - Casing to casing - axial vibrations 50
5.31 Sensors placement on the shaft in the axial direction 51
5.32 Measured transfer functions - Casing to shaft - axial 51
5.33 Transfer function and stability diagram - Casing to shaft - axial direction 52
5.34 Measured transfer functions - Shaft to casing - axial direction . . . 53
5.35 Transfer function and stability diagram - Shaft to casing - axial . . 53
5.36 Measured transfer functions - shaft to shaft - axial 54
5.37 Transfer function and stability diagram - shaft to shaft - axial . . . 55
5.38 Experimental setup - Rotating spindle 56
5.39 Sensors positioning for radial vibrations 57
5.40 Campbell diagram in radial direction 58
5.41 Sensors positioning for radial vibrations 58
5.42 Campbell diagram in axial direction 59
5.43 Auto spectrum for radial excitations 60
5.44 Auto spectrum for axial excitations 61

6.1 Waviness excitation in ball bearings 65
6.2 Decomposition of the finite element model into a reduced set of CMS component modes 68
6.3 Representation of moving contact loads and analytical basis functions used in the SKF CMS method 69

7.1 2D Fourier components 73
7.2 Fourier shaft: 3D mesh 73
7.3 Fourier shaft: interfaces and connections 74
7.4 Fourier shaft model 74
7.5 Beam shaft model 75
7.6 Bezel: model and mesh 76
7.7 Bushing: model and mesh 77
7.8 Ring: model and mesh 78
7.9 Shaft and accessories: beam shaft model 79
7.10 Shaft and accessories: Fourier shaft model 79
7.11 Casing: model and mesh 81
7.12 Spindle assembly: Fourier shaft model 82
7.13 Fourier discs for the spindle in operation - beam shaft 83
7.14 Fourier discs: model and meshing 84
7.15 Numerical Campbell diagram for the undamped model - beam shaft 84
7.16 Spindle in rotation: Fourier model and mesh 85

7.17 Numerical Campbell diagram for the undamped model - Fourier shaft 86

8.1 Shaft: mode shape 1 comparison 89
8.2 Shaft: mode shape 2 comparison 89
8.3 Ring - mode shape 1: comparison 91
8.4 Bushing - mode shape 1: comparison 92
8.5 Bezel - mode shape 1: comparison 93
8.6 Shaft and accessories - mode 1: comparison 95
8.7 Shaft and accessories - mode 2: comparison 95
8.8 Spindle assembly - mode shape 1: comparison 100
8.9 Spindle assembly - mode shape 8: comparison 100

A.1 Front and side view of the ring 115
A.2 Front and side view of the bearing 116
A.3 Front, back and side view of bezel 117
A.4 Front, back and side view of the bushing 118
A.5 Front, back and side view of the flange 119
A.6 Caption 120
A.7 Front and side view of the ring 121
A.8 Cross section of the shaft 121
A.9 Front and side view of the cup 122
A.10 Cylinder cross section 123
A.11 Side and top view of the electric motor 123

Acronyms

DE
Driven End

DOF
Degrees of Freedom

IR
Inner Ring

NDE
Non Driven End

ODS
Operating Deflection Shape

OR
Outer Ring

TF
Transfer Function

Chapter 1

Introduction

The dynamic behaviour of high-speed spindles represents a critical aspect in the design and optimisation of precision machining systems, where increasingly stringent performance requirements demand accurate prediction of vibrational phenomena under both stationary and operating conditions. In this context, numerical modelling and experimental modal analysis constitute complementary methodologies: the former provides a controlled framework to analyse the system's structural response, while the latter offers a direct measurement of the real dynamic behaviour, capturing the influence of manufacturing tolerances, assembly conditions, and boundary constraints. Despite their complementary nature, achieving a consistent correlation between numerical and experimental results remains a significant challenge, particularly when the modelled system includes complex components such as rolling bearings and spindle–housing interfaces, whose dynamic response is sensitive to preload conditions, contact mechanics and assembly-induced deformations.

The numerical model investigated in this work is not a classical finite-element formulation. Instead, it is based on SKF SimPro, a proprietary multibody simulation environment specifically developed for the modelling of spindle systems and super-precision bearings. The software incorporates analytical formulations for rolling-element contacts, elastohydrodynamic lubrication (EHL), bearing waviness and moving load representations through SKF's specialised Component Mode Synthesis (CMS) approach. This modelling strategy offers substantial advantages in terms of computational efficiency and the physical fidelity of bearing behaviour, but it also introduces inherent limitations, particularly in the treatment of casing flexibility, boundary conditions, and the representation of certain axial deformation mechanisms. For these reasons, a rigorous experimental validation becomes indispensable to assess the predictive capability of the numerical model and to identify the conditions under which it can be reliably used.

The present thesis pursues two primary objectives.

The first is to evaluate the reliability of the experimental modal analysis workflow,

implemented through ArtemiS Suite, when applied to lightweight and geometrically complex components such as those constituting a high-speed spindle. Although experimental modal analysis is a well-established technique, its accuracy strongly depends on the quality of the excitation, sensor placement, boundary conditions, and the assumptions underlying parameter extraction. By conducting a complete campaign of modal tests on individual components, rotating subassemblies and the full spindle, this work aims to clarify the potential and limitations of the experimental procedure, ensuring that the extracted modal parameters represent a trustworthy benchmark for numerical correlation.

The second objective is to use the experimental results not only for the calibration of the numerical model, but also—crucially—to derive general guidelines for future users of the SKF SimPro environment regarding the appropriate boundary conditions to impose at the spindle bearings. In fact, boundary conditions represent the most delicate and influential aspect in the numerical simulation of spindle dynamics. Different assumptions concerning the axial freedom of the bearings, the preload distribution, and the manner in which the outer rings interact with the housing can lead to substantial variations in the predicted natural frequencies and mode shapes. By systematically comparing experimental and numerical modal parameters across multiple configurations, this thesis identifies the boundary-condition settings that most accurately reproduce the physical behaviour of the system. These findings provide essential recommendations for improving the fidelity of future simulations and for supporting the development team in refining the modelling of bearing–housing connections within the SKF software.

Through the combination of extensive experimental testing, detailed numerical modelling and a structured comparison across all levels of assembly, this work contributes to a deeper understanding of spindle dynamics and offers a validated methodological framework for the interpretation and prediction of vibration behaviour in high-speed applications.

Chapter 2

Numerical model of the spindle

2.1 General Information and Current State of the Tool

SKF SimPro Spindle is an advanced multibody simulation software designed to evaluate the performance of super precision bearings. The software enables users to model spindle applications by creating a mechanical system that includes a shaft, various types and combinations of super precision bearings arranged in specific configurations, and simplified housings. One of its most significant functionalities is the ability to generate a Campbell diagram for the spindle setup under investigation, which provides insight into the dynamic behavior of the system.

2.2 Problem Statement

In SKF SimPro Spindle, it is possible to model systems in which bearings are axially free with respect to the housing. This axially free configuration enables the creation of a floating support group, which may be preloaded either by using rigid spacers or by employing springs. When performing modal analysis in SKF SimPro tools, it has been observed that the eigenfrequencies can vary significantly depending on whether the bearings are set to be fixed or axially free. In certain cases, modes that are potentially non-existent have also been detected, raising questions about the accuracy of the boundary conditions applied in the simulations.

2.3 Need for Additional Study and Validation

In SKF SimPro Spindle, super precision bearings are grouped into support groups (Figure 2.1), which consist of bearings arranged in a specific order with a defined internal preload.

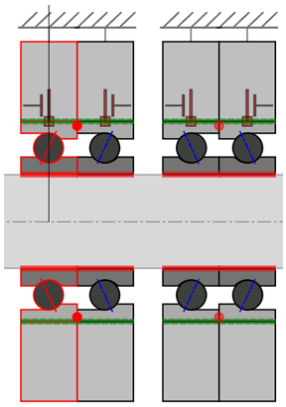


Figure 2.1: An example of a support group containing four bearings

These support groups vary according to application requirements, as shown in Figure 2.2, and are generally classified as locating, meaning axially fixed with respect to the housing, or non-locating, meaning axially free.

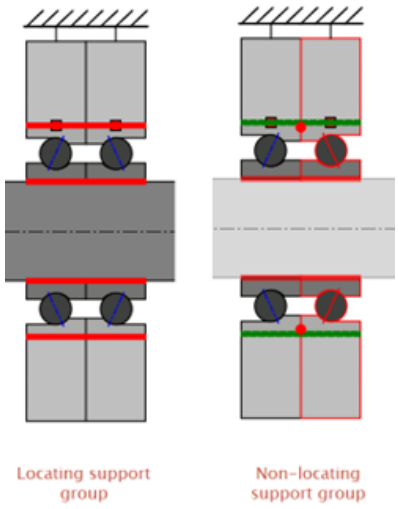


Figure 2.2: Examples of a locating and non-locating support group

To create these support groups with different arrangements and combinations

of bearings, the software considers complex connection mechanisms between the housing and the bearings in the background. When conducting a Campbell diagram study of spindle systems, the stiffness of the system changes depending on the type and arrangement of the support group. A comparison between two spindle systems—one with a locating configuration and one with a non-locating configuration—revealed that the frequency of the axial mode differs significantly between the two setups. In the spindle system in Figure 2.3, the bearing set on the right side is non-locating and therefore axially free with respect to the housing. This configuration exhibits an eigenfrequency of 168.23 Hz for the first eigenmode, which is axial.

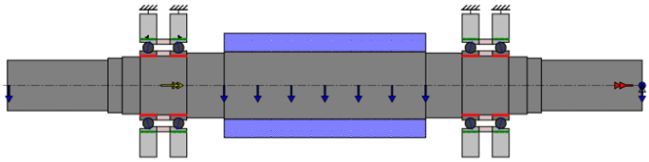


Figure 2.3: The support on the right side is non-locating

If the same set is analyzed as a locating configuration for the Campbell diagram, Figure 2.4 shows how the eigenfrequency for the first axial mode increases to 240.51 Hz.

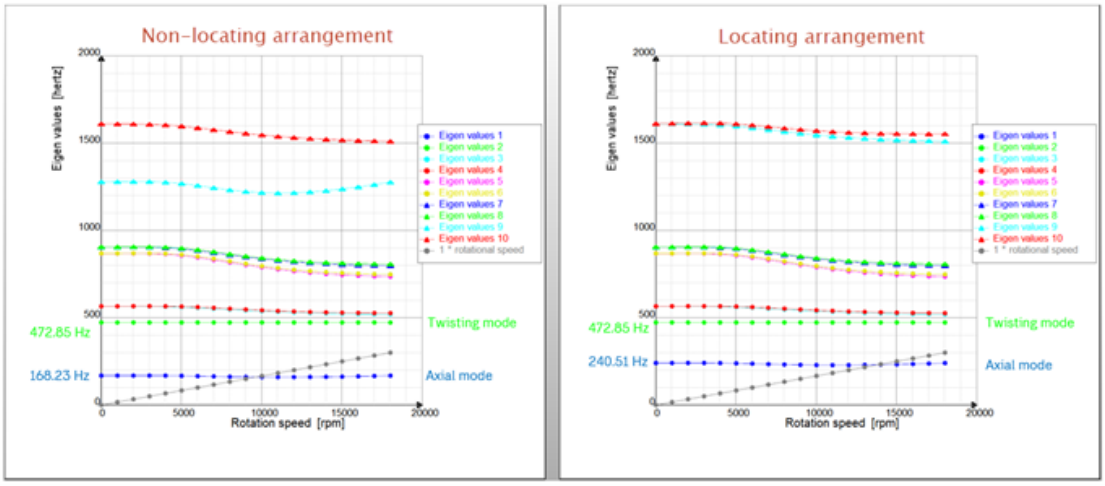


Figure 2.4: Campbell diagram of a locating vs. the non-locating arrangement

2.4 Expected Outcome

Experimental modal analyses will be conducted on spindle assemblies, while numerical modal analyses will be performed on similar models using SKF SimPro tools under different boundary condition setups. The results obtained from these two approaches will be compared in detail to identify the boundary condition that most closely aligns the numerical analysis with the experimental findings. Based on these comparisons, the most suitable boundary condition will be proposed to the development team to enhance the reliability and accuracy of future simulations.

2.5 Validation

To confirm these variations in eigenfrequencies, it is essential to compare the physical model with the simulation results and contrasting these findings with the Campbell diagram generated in SKF SimPro Spindle.

2.6 Expected Outcomes and Further Actions

defined Experimental modal analysis will be carried out on spindle setups, while numerical modal analysis will be performed on an identical virtual model using SKF SimPro Spindle and other SKF tools. The results from these two approaches will be thoroughly compared to identify any discrepancies. This detailed investigation aims to determine how closely the numerical modal analysis aligns with real-world behavior. Based on these findings, if necessary, recommendations will be made to update the methodology for connecting outer rings and housings in SKF SimPro Spindle, thereby improving the accuracy of Campbell diagram studies and bringing simulation results closer to reality.

Chapter 3

Overview of the investigated model

The subject of this study is the KL-60C-2 ball bearing spindle, produced by the company DAKE, designed for high-speed and high-precision applications. Its maximum rotational speed reaches 60,000 rpm, and it is intended for high-precision tasks, specifically for the surface finishing of mobile phone screens.

This device consists of two main sections: the housing, which forms the stator, and the shaft with its accessories, which forms the rotor. Rotation is driven by an electric motor that includes 24 bars in both the stator and rotor.

3.1 Stator

Figure 3.1 & 3.2 shows the cylindrical, hollow shape of the casing to ensure proper placement of all components and allow rotation.

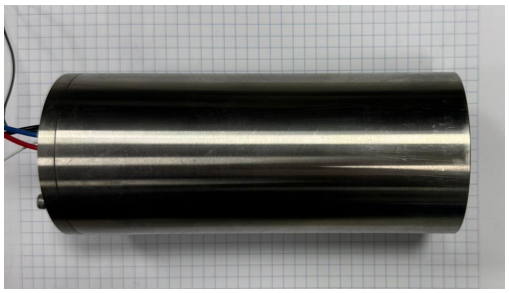


Figure 3.1: Front view of the housing

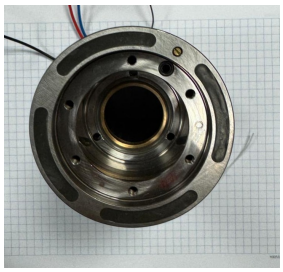


Figure 3.2: Top view of the housing

The large cylinder forming the stator consists internally of three main elements:

a cup (Figure 3.3 & 3.4), a cylindrical structure (Figure 3.5 & 3.6), and an electric motor Figure 3.7 positioned at the central section.

The cup is mounted on the non-driven end (NDE) side and features a series of holes: the outermost ones are designed to allow the circulation of a cooling fluid—either water or oil—while the three innermost holes serve as passages for the electrical wires that supply power to the motor.

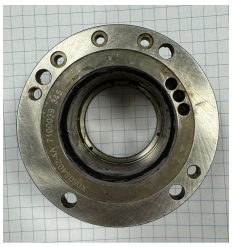


Figure 3.3: Top view of the cup

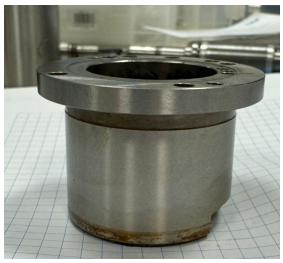


Figure 3.4: Front view of the cup

The cylindrical structure is illustrated in Figure 3.5 & Figure 3.6

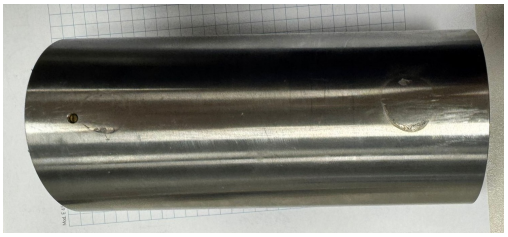


Figure 3.5: Front view of the housing

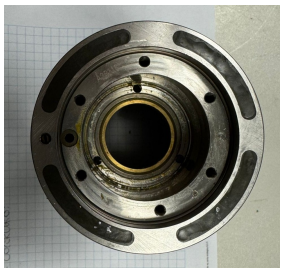


Figure 3.6: Top view of the housing

In the central part of the housing, the electric motor is placed.



Figure 3.7: Electric motor

It consists of 24 aluminum conducting bars, which are visible on the inner side of the housing, and is powered by alternating current.

3.2 Rotor

The rotor section consists of:

- a perfectly symmetrical hollow cylindrical shaft Figure 3.8



Figure 3.8: Aluminum shaft

- three identical bearings: **SKF 7003 CE RZ/1** Figure 3.9 belonging to the super-precision category and with a rubber seal (visible in the photo as the black circular ring between the inner and outer race).



Figure 3.9: Bearing section

- a bushing Figure 3.10 & 3.11



Figure 3.10: Front view of the bushing



Figure 3.11: Side view of the bushing

- a bezel - Figure 3.12 & 3.13 & 3.14

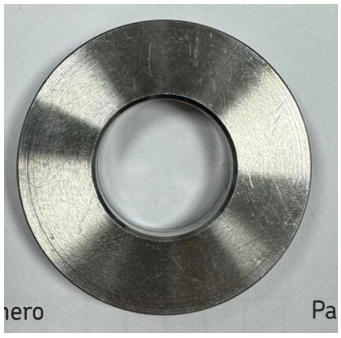


Figure 3.12: Bezel - front view



Figure 3.13: Bezel - side view



Figure 3.14: Bezel - back view

- a flange - Figure 3.15 & 3.16 & 3.17



Figure 3.15: Flange - front view



Figure 3.16: Flange - side view

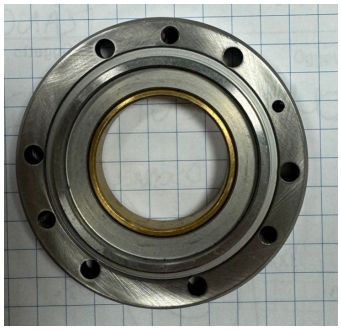


Figure 3.17: Flange - back view

- a ring - Figure 3.18 & 3.19



Figure 3.18: Ring - front view



Figure 3.19: Ring - side view

- a variable number of springs depending on the desired level of preload



Figure 3.20: Spring disc



Figure 3.21: Ring

The ring shown in Figure 3.20 contains a series of holes that accommodate the helical springs (only ten are visible, corresponding to the specified preload conditions), whereas the ring depicted in Figure 3.21 features an inner bronze-colored circular crown designed to ensure proper coupling with the inner race of the bearing. These two components are mounted facing each other. By adjusting their relative distance, the springs can be compressed to varying extent, thereby applying a different preload. The characteristic of the helical springs employed is linear, as shown in the Figure 3.22.

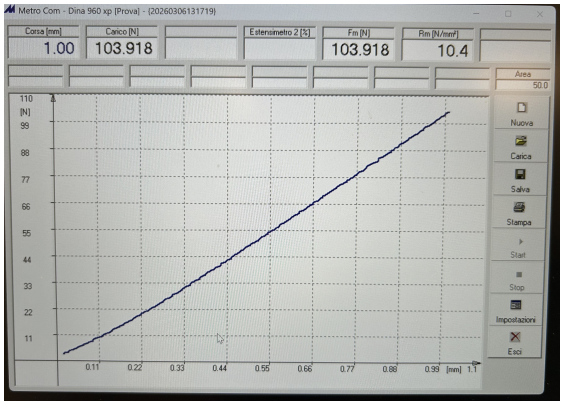


Figure 3.22: Characteristic line of the springs

Therefore, for a baseline configuration with 10 springs, the applied preload is 100N.

The shaft is oriented from left to right, with the driven end on the left and the non-driven end on the right. As illustrated in the image, the central section of the shaft is thickened to accommodate the rotor bars, which are evenly distributed along the circumference.

The two bearings of the driven end (DE) are located in the section $27{,}3mm < x < 47{,}3mm$ because each one has a thickness of 10 mm; the bearing of the non driven end (NDE) is located in the section at $132{,}07mm < x < 142{,}07mm$.

The bearing arrangement adopted is a combination of back-to-back and tandem configurations. On the driven end, two bearings are mounted in tandem, and when considered together with the bearing on the non-driven side, they form an overall back-to-back layout. Since the tandem pair has perfectly parallel load lines, it can be regarded as a single bearing with increased axial capacity. This configuration provides a larger resistant arm, which means that, for the same tilting moment to be supported, the required force—and consequently the load acting on each bearing—is reduced. The hybrid layout thus combines the advantages of both dispositions: the tandem pair ensures high thrust capacity in one direction without overloading individual components, while the back-to-back geometry offers rigidity, bidirectional axial support, and improved resistance to tilting moments and shaft deflection. In addition, the distribution of stresses across three bearings enhances reliability and fatigue life, while the back-to-back arrangement maintains alignment under thermal expansion, ensuring stability under variable operating conditions. Finally, the single bearing is subjected to a controlled preload, which can be adjusted by varying the number and compression level of the springs, allowing fine regulation of the system's performance.

It is also important to distinguish between rotating (Figure 3.23) and stationary

components: the rotating parts include the shaft, bearings, bushing, bezel and ring, while the flange and springs, although mounted on the shaft, do not rotate with it.



Figure 3.23: Shaft and rotating components

Chapter 4

Experimental Setup for Modal Analysis

4.1 Modal Analysis: principles, applications, and validity conditions

In the field of industrial design and development, *modal analysis* represents an essential tools for ensuring product reliability, performance, and safety[1]. This methodology enables engineers to study the dynamic behavior of structures and mechanical systems, identifying potential weaknesses before production and mitigating risks associated with resonance and excessive vibration.

Modal analysis is widely adopted to understand how a structure or system reacts to different dynamic excitations. Specifically it determines the natural frequencies, mode shapes, and damping ratios of a structure. These parameters are critical for preventing resonance phenomena that could compromise structural integrity and operational efficiency.

The theoretical background presented in this chapter is grounded in well-established modal analysis literature, including the works of Ewins [2] and Maia & Silva [3]

4.2 Industrial Applications

Table 4.1 shows different examples of modal and frequency response techniques employed across numerous sectors, including:

Real life applications	
Automotive	Vibration analysis of components such as engines, transmissions, and chassis to improve comfort and safety.
Aerospace	Optimization of aeronautical structures to ensure strength and stability under extreme operating conditions.
Manufacturing	Vibration control in industrial machinery to enhance productivity and reduce wear.
Oil & Gas	Assessment of pipelines and offshore structures to prevent failures caused by dynamic loads.

Table 4.1: Industrial sectors and their applications of modal analysis

4.3 Benefits of Modal Analysis

A correct implementation of these techniques offers significant advantages:

- **Early Identification of Critical Issues**: Simulations and experimental tests allow engineers to detect structural weaknesses before production.
- **Performance Optimization**: Dynamic parameters are refined to achieve the best balance between weight, stiffness, and cost.
- **Risk Mitigation**: Eliminating resonance and unwanted vibrations enhances product safety and reliability.
- **Economic Savings**: A robust design reduces the likelihood of defects or recalls, lowering maintenance and repair costs.

4.4 Conditions for the Validity of Modal Analysis

The reliability of modal analysis depends on satisfying specific theoretical, experimental, and data quality conditions.

4.4.1 Theoretical Assumptions

- **Linearity and Stationarity**: The system must exhibit linear behavior, and its physical properties (mass, damping, stiffness) should remain constant during testing.

- **Symmetric System Matrices**: Mass, damping, and stiffness matrices are assumed to be symmetric, ensuring reciprocity in frequency response measurements ($h_{ij} = h_{ji}$).
- **Damping Characteristics**: Proportional damping results in real mode shapes, while non-proportional damping introduces complex modes requiring advanced analysis.

4.4.2 Experimental Requirements

- **Boundary Conditions**: Support conditions significantly affect modal parameters. For free-free conditions, rigid body modes should have frequencies at least one-tenth lower than the first flexible mode.
- **Minimal Test Setup Influence**: Sensors and excitation devices must not significantly alter the structural dynamics.
- **Reference Location Selection**: The reference point should not coincide with a modal node to avoid missing modes in FRFs.
- **Adequate Excitation Spectrum**: The input force spectrum should be reasonably flat across the frequency range of interest.
- **Proper Excitation Method**: Hammer tips or shaker signals must be selected to cover the desired frequency range.
- **Sufficient Measurement Points**: Measurement locations must allow for an unambiguous description of mode shapes.
- **Rest Between Impacts**: For impact testing, the structure must return to rest before subsequent impacts.

4.4.3 Signal Processing and Data Acquisition

- **FFT Periodicity Compliance**: The sampled signal must satisfy the periodicity requirement of the FFT; otherwise, windowing is required.
- **Leakage Minimization**: Prefer leakage-free excitation signals such as burst random or sine chirp.
- **Windowing**: Force windows remove noise after impact; exponential windows minimize leakage but can artificially increase damping.
- **Averaging**: Reduces variance and improves statistical reliability, especially for random excitation.

- **Zooming**: Essential for resolving closely spaced modes and reducing leakage distortion.

- **Proper Digitization**: Analog-to-digital conversion must avoid clipping and quantization errors.

- **High Coherence**: The coherence function should confirm strong correlation between input and output signals.

4.4.4 Data Consistency

- **Mass Loading Control**: Minimize accelerometer mass effects, especially on lightweight structures.

- **Consistent Test Setup**: Avoid changes in instrumentation or support conditions between measurements.

- **Multiple References**: Use multiple reference points to improve redundancy and capture all modes.

4.4.5 Validation Criteria

- **Pole Stability**: Variations should remain below 1% in frequency and 5% in damping across increasing model orders.

- **Quality Indicators**: Modal Assurance Criterion (MAC), Modal Scale Factor (MSF), orthogonality checks, coherence, and stability diagrams should confirm model reliability.

4.5 Parameter Estimation Techniques

- **Single-Mode Methods**: Peak-picking and circle-fit are fast but approximate; suitable for lightly damped, well-separated modes.

- **Multiple-Mode Methods**: Necessary for closely spaced or heavily damped modes; involve curve fitting in frequency or time domain.

- **Residual Terms**: Account for out-of-band modes; low-frequency residuals relate to rigid body mass, high-frequency residuals to local stiffness.

4.6 Real vs Complex Modes

- **Real Modes**: Occur under proportional damping assumptions; all points move in phase (standing wave).

- **Complex Modes**: Non-proportional damping or closely spaced modes lead to phase differences (traveling wave behavior).

4.7 Correlation with Analytical Models

Experimental results are essential for validating Finite element correlation. Modal Assurance Criterion (MAC) and Modal Scale Factor (MSF) are used to compare mode shapes and scaling. Accurate correlation requires matching coordinate systems between the test and the finite element mesh.

4.8 Experimental Setup

From an experimental perspective, it is essential to design a test setup that satisfies all the validity conditions previously discussed. In modal analysis, the modal parameters are intrinsic properties of the system itself. For this reason, they do not depend on the type of support chosen for the test, and each experimental setup should theoretically yield equivalent results. Nevertheless, for each component analyzed, a dedicated support was designed rather than adopting a standardized setup. This choice can be justified in light of certain assumptions and predictions based on the component's geometry and stiffness.

4.8.1 Support Configuration

The following figures present a selection of photographs (Figure 4.1 & 4.2) depicting different support configurations, each intended to emphasize specific characteristics of the system under investigation. These visual examples serve to illustrate how variations in the complexity of the components can influence the experimental setup and highlight the rationale behind the adopted design choices. For most components, foam supports were selected because they provide an almost faithful reproduction of the conditions and assumptions underlying the validity of the model. Furthermore, the deformations and vibration modes of the foam occur at very low frequencies, which is particularly relevant since, given the operational frequency range, they do not interfere with the ultimate purpose of the analysis.

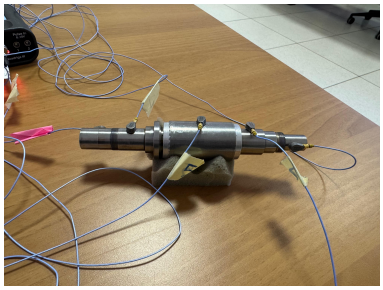


Figure 4.1: Foam support for the shaft

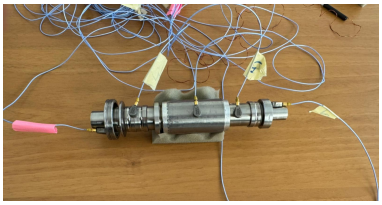


Figure 4.2: Foam support for the rotating components

Figure 4.3: Two different experimental setup

The experimental setup previously described and illustrated was not retained for the measurements on the rotating spindle, as it did not provide sufficient support for the system and posed a risk of component damage in the event of a fall. For these tests, the Campbell diagram and the Operating Deflection Shape (ODS) analysis were carried out by exciting and measuring the system while the spindle rotated across its operating speed range. This procedure enables the identification of speed-dependent resonances and operational deformation patterns, thereby complementing conventional modal analysis—which is performed under stationary conditions—by revealing dynamic behaviours that cannot be captured in static tests. To ensure adequate stability during rotation, Figure 4.4 illustrates the rigid support structure that was therefore designed and coated with a rubber layer to isolate the base vibrations from those of the spindle. The thickness of the supports was minimised to maximise the accessible surface area for sensor placement, and the spacing between the two supports was selected to avoid introducing bending moments that could compromise measurement accuracy.

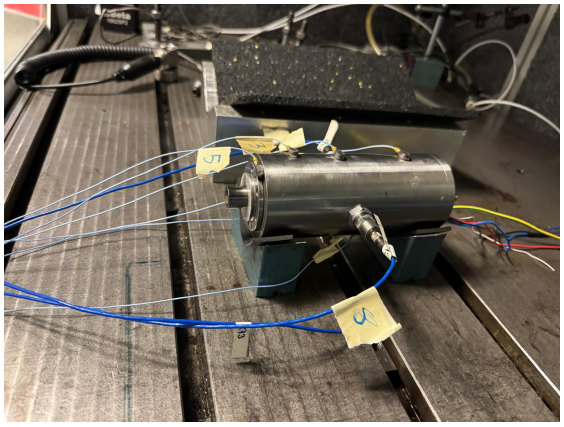


Figure 4.4: Support for the rotation of the spindle

4.8.2 Instrumentation and Data Acquisition

For excitation and response measurement, sensors and impact hammers manufactured by PCB PIEZOTRONICS were employed.

PCB 352A25 (Figure 4.5) is a miniature, lightweight, ceramic shear ICP accelerometer, whose performance and physical parameters [4] are listed in Table 4.2 & 4.3

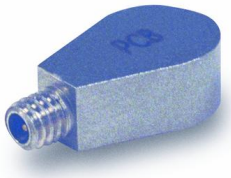


Figure 4.5: PCB 352A25 accelerometer

Parameter	**Value**
Sensitivity (±15 %)	0.25 mV/(m/s^2)
Measurement Range	±19600 m/s^2 pk
Frequency Range (±5 %)	1.0 to 10000 Hz
Frequency Range (±10 %)	0.7 to 13000 Hz
Frequency Range (±3 dB)	0.3 to 20000 Hz
Resonant Frequency	$\geq 80kHz$
Broadband Resolution (1)	0.1 m/s^2 rms
Non-Linearity	≤1 %
Transverse Sensitivity	≤ 5 %

Table 4.2: Performance parameters PCB 352A25

Parameter	**Value**
Size - Height	3.6 mm
Size - Length	11.4 mm
Size - Width	6.4 mm
Weight	0.6 g
Sensing Element	Ceramic
Sensing Geometry	Shear
Housing Material	Titanium
Sealing	Epoxy
Mounting	Adhesive

Table 4.3: Physical Characteristics PCB 352A25

It is worth noting that the sensor mass, being extremely small, 0.6 g, does not interfere with the dynamic response of the component or system under investigation.

For the measurements on the rotating spindle, different sensors were employed, specifically the **KS78C** model (Figure 4.6) produced by **MMF**, because, although heavier (Table 4.4 & 4.5) [5], they can be secured using adhesive. This feature is essential since the rotating spindle, lacking an appropriate water-cooling system—which would make the setup more complex and fail to ensure accurate results—tends to overheat, making the wax-based fixation ineffective.



Figure 4.6: KS78C Accelerometer

Parameter	**Value**
Sensitivity (±15 %)	11.11 mV/(m/s^2)
Measurement Range	±6.67 m/s^2
Frequency Range (±5 %)	0.6 to 14000 Hz
Frequency Range (±10 %)	0.4 to 16000 Hz
Frequency Range (±3 dB)	0.2 to 20000 Hz
Resonant Frequency	$\geq 42kHz$
Broadband Resolution (1)	0.04 m/s^2 rms
Non-Linearity	Not specified
Transverse Sensitivity	≤ 5 %

Table 4.4: Performance parameters KS78C

Parameter	**Value**
Size - Height	Not specified
Size - Length	Not specified
Size - Width	Not specified
Weight	11.2 g
Sensing Element	Piezoelectric
Sensing Geometry	Shear design
Housing Material	Stainless steel
Sealing	IP60
Mounting	M5 thread

Table 4.5: Physical Characteristics of KS78C100 Accelerometer

In order to perform the impact tests, the PCB 086E80 miniature instrumented impulse hammer [6] (Figure 4.7) is employed, whose specifics are reported in Table 4.6 & 4.7



Figure 4.7: PCB 086E0 impulse hammer

Parameter	**Value**
Sensitivity (±20 %)	22.5 mV/N
Measurement Range	222 N pk
Resonant Frequency	$\geq$ 100 kHz
Non-Linearity	$\leq$ 1 %

Table 4.6: Performance Parameters PCB 086E80

Parameter	**Value**
Sensing Element	Quartz
Sealing	Epoxy
Hammer Mass	4.8 g
Head Diameter	6.3 mm
Tip Diameter	2.5 mm
Hammer Length	107 mm
Electrical Connection Position	Side
Extender Mass Weight	1.25 g

Table 4.7: Physical Characteristics PCB 086E80

For larger and heavier components, such as the casing and the overall system assembly, the impulse generated by the PCB 086E80 mini hammer is insufficient to adequately excite the structure. To overcome this limitation, another device from the same manufacturer, the **PCB 086C03** (Figure 4.8), was employed, that is a modally tuned impulse hammer with force sensor and tips (Table 4.8 & 4.9).



Figure 4.8: PCB 086C03 impulse hammer

Parameter	**Value**
Sensitivity (±15 %)	2.25 mV/N
Measurement Range	±2224 N pk
Resonant Frequency	$\geq$ 22 kHz
Non-Linearity	$\leq$ 1 %

Table 4.8: Performance Parameters PCB 086C03

Parameter	**Value**
Sensing Element	Quartz
Sealing	Epoxy
Hammer Mass	0.16 kg
Head Diameter	1.57 cm
Tip Diameter	0.63 cm
Hammer Length	21.6 cm
Electrical Connection Position	Bottom of Handle
Extender Mass Weight	75 g

Table 4.9: Physical Characteristics PCB 086C03

The selection of hammer tips is of critical importance, as it directly determines the frequency range that will be analyzed. Indeed, Figure 4.9 shows how different tips are capable of exciting distinct frequency ranges

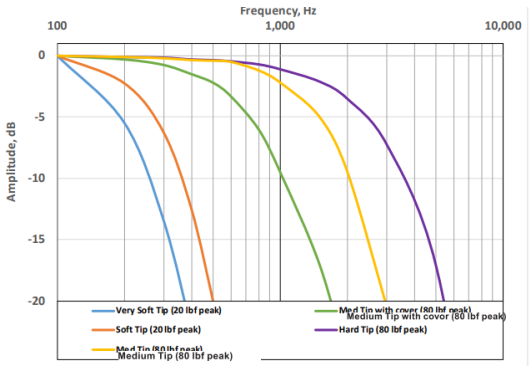


Figure 4.9: Excitation range for different Tips

The case study focuses on a range from 0 to 10 kHz in order to account for all relevant phenomena, including bearing defect frequencies on both inner and outer rings, rotational speed and its harmonics, as well as ball pass frequencies. Within this specified frequency range, the choice falls on the hard metal tip, as experimental evidence indicates that the soft rubber tip would only reach a maximum of approximately 8 kHz and would additionally introduce measurement errors caused by the double-impact phenomenon.

Data acquisition was performed using **SQuadriga III** by **Head Acoustics**, integrated with the **ArtemiS Suite** software interface.



Figure 4.10: SQuadriga III

As shown in Figure 4.10, the SQuadriga III system provides a total of eight acquisition channels for sensors and the impact hammer. During the impact tests, one channel was allocated to the hammer and seven channels to the other sensors. Conversely, during the tests performed on the rotating spindle, all eight channels were used to connect eight sensors. A closer examination of the component geometry reveals that most parts are highly symmetric and relatively small in size. This observation strongly supports the chosen number of sensors, as it ensures accurate

measurements and a reliable estimation of modal parameters with a high degree of fidelity.

Chapter 5

Results of the Experimental modal analysis

This chapter presents the experimental results obtained through a structured sequence of modal analyses on the spindle assembly and its components. The investigation followed a progressive approach: starting with the experimental modal analysis of each individual component considered as an isolated system, then examining the rotating parts assembled together, and finally analyzing the complete spindle assembly as a single entity. This methodology was adopted to facilitate problem-solving during subsequent evaluations; by understanding the dynamic behavior of each component across the entire frequency spectrum, any anomalies or unexpected responses in the full assembly can be traced back to their likely source. From a practical standpoint, the modal analysis was conducted using the ArtemiS Suite software following a systematic workflow. The process included:

1. **Creation of the CAD model and export in tessellated format (.stl)**;
2. **Definition of excitation points** on the tessellated file, each representing a degree of freedom and approximating local behavior. A compromise was required between computational cost and frequency resolution;
3. **Identification and positioning of sensors**, as incorrect placement (e.g., on a nodal point) would invalidate the analysis;
4. **Initialization and auto-calibration of all measurement instruments**, ensuring accurate post-processing and modal parameter extraction;
5. **Impact testing** for data acquisition;
6. **Extraction of modal parameters** (natural frequencies and damping ratios) using the dedicated "Modal Analysis" tool;

7. **Visualization of mode shapes** at selected natural frequencies.

In carrying out the experimental tests, a roving hammer configuration was adopted. In this approach, the accelerometers were fixed on the structure and served as reference channels, while the excitation point was moved across all the locations of interest using an instrumented impact hammer. This choice was driven by practical considerations: the accelerometers were mounted using adhesive wax, which ensures good coupling but requires significant time for correct installation. Relocating them repeatedly, as required in a roving-accelerometer setup, would have drastically increased preparation time and reduced repeatability. By contrast, the impact hammer is lightweight, compact, and easily maneuverable, allowing the excitation of all predefined points without geometric or accessibility limitations. From a theoretical perspective, the roving-hammer and roving-accelerometer approaches are fully equivalent because of the symmetry of the frequency response function matrix $H(\omega)$. This symmetry implies that exchanging the roles of excitation and response does not alter the modal information obtained; thus, fixing the sensors and moving the hammer provides the same data that would be obtained by fixing the hammer and moving the sensors. The preference for the roving hammer method in this study therefore follows from practical efficiency rather than intrinsic differences in the modal information extracted. Finally, an additional test was performed on the rotating spindle to obtain the experimental Campbell diagram, serving as a cross-validation of the previous analyses. The results reported in this section include natural frequencies, damping ratios, and mode shapes, supported by transfer functions (TFs) and stability diagrams where relevant. These findings provide the foundation for the comparative assessment with numerical predictions discussed in the next chapter.

5.1 Shaft

In Figure 5.1, the experimental setup selected for the modal analysis of the shaft can be observed. The device is supported only in its central region—using a small foam parallelepiped—in order to minimize the contact surface. This arrangement makes it possible to reproduce the free–free boundary condition at the right and left ends with good accuracy, since these regions exhibit the maximum vibration amplitudes, whereas the central portion, being thick and stiff, remains almost stationary.

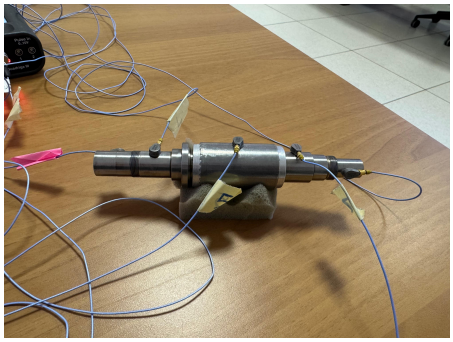


Figure 5.1: Experimental setup - Shaft

A total of 60 degrees of freedom were identified, and five single-axis sensors were installed, although only four were used due to signal-quality considerations. After carrying out the measurements, the following (Figure 5.2) results were obtained

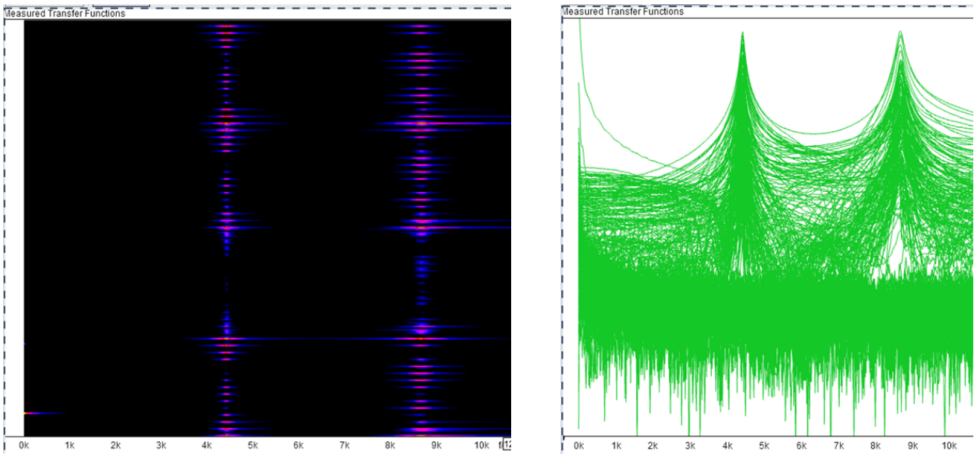


Figure 5.2: Measured transfer functions - Shaft

As can be seen in the lower portion of the Figure 5.2 on the right, very noisy and contaminated signala are present. This is not desirable for the extraction of modal parameters, since the software would be forced to interpolate a signal that, in practice, carries no meaningful information; for this reason, it was excluded from the analysis. With this premise, it was then possible to derive the transfer-function and the stability diagram (Figure 5.3).

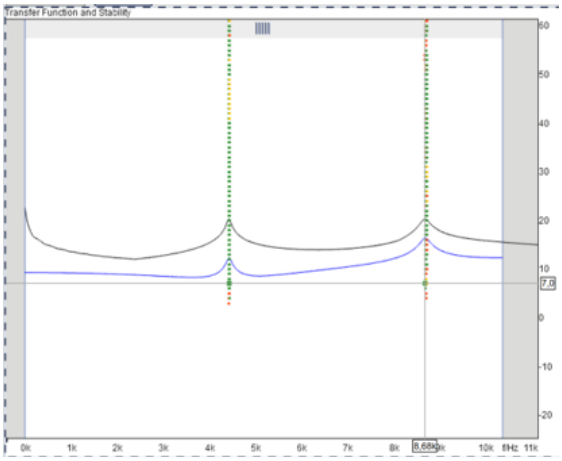


Figure 5.3: Transfer function and stability - Shaft

from which the following (Table 8.1) modal parameters can be derived:

Modal Parameters		
Shape Name	**Frequency [Hz]**	**Damping - ξ - [%]**
Mode shape 1	4426	1.0
Mode shape 2	8679	0.9

Table 5.1: Modal parameters of the shaft

5.2 Shaft Accessories

The accessories mounted on the shaft and rotating with it are

- the bezel,
- the bushing,
- the ring

These components are functionally necessary for the assembly of the system; however, they do not play a strategic role in determining its dynamic response. Since their configuration is standardized, they cannot be adjusted to achieve a desired output. Consequently, only the numerical values of the modal parameters of each individual component are reported.
For the bezel, the modal parameters are reported in Table 5.2:

Modal Parameters		
Shape Name	**Frequency [Hz]**	**Damping - ξ - [%]**
Mode shape 1	27318	1.8

Table 5.2: Modal parameters of the bezel

For the bushing,the modal parameters are reported in Table 5.3:

Modal Parameters		
Shape Name	**Frequency [Hz]**	**Damping - ξ - [%]**
Mode shape 1	28670	0.2

Table 5.3: Modal parameters of the bushing

For the ring, the modal parameters are reported in Table 5.4:

Modal Parameters		
Shape Name	**Frequency [Hz]**	**Damping - ξ - [%]**
Mode shape 1	27318	1.8

Table 5.4: Modal parameters of the ring

In addition, as can be seen from the listed natural frequencies, these values lie well outside the operational range of interest, namely $0 \leq f \leq 10\,\text{kHz}$

5.3 Rotating components

With regard to the experimental setup of this system, it follows exactly the same configuration adopted in the previous analysis (Figure 5.1), since additional components are only mounted at the two extremities; therefore, the foam support positioned at the central region remains appropriate. For this configuration, vibrations in both the axial and radial directions were considered. The two cases differ only in the number of excitation points and in the placement of the sensors, because exciting the structural modes in both directions requires impacting the specimen at different locations and, consequently, positioning the sensors so as to accurately capture the oscillations along the intended measurement direction.

5.3.1 Radial vibrations

Figure 5.4 highlights the sensor locations and the foam support previously described



Figure 5.4: Experimental setup - Shaft and accessories - radial vibrations

In this analysis, 50 excitation points and 5 sensors were considered. After carrying out the measurements, the following (Figure 5.5) results were obtained

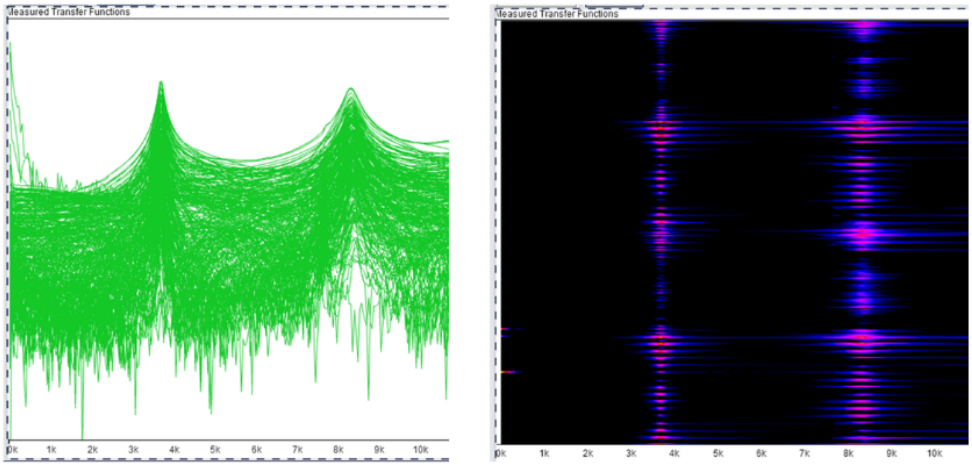


Figure 5.5: Measured transfer functions - Shaft and accessories - radial vibrations

In this case, all five sensors were able to provide meaningful measurements; therefore, no exclusions were necessary. With this premise, it was then possible to derive the transfer-function and the stability diagram (Figure 5.6)

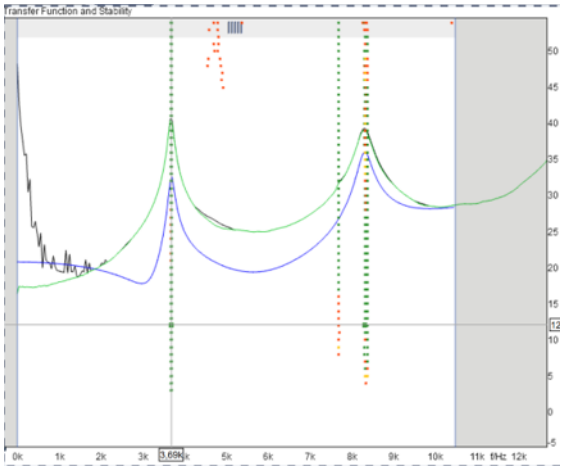


Figure 5.6: Transfer function and stability diagram - Shaft and accessories - radial vibrations

from which the following (Table 5.5) modal parameters can be derived:

Modal Parameters		
Shape Name	**Frequency [Hz]**	**Damping - ξ - [%]**
Mode shape 1	3687	1.6
Mode shape 2	8310	1.7

Table 5.5: Modal parameters of the rotating components - radial vibrations

5.3.2 Axial vibrations - Da Capire se mettere o meno

The figure highlights the sensor locations and the foam support previously described

IMMAGINE SETUP SPERIMENTALE - MANCA

In this analysis, 16 excitation points and 5 sensors were considered. After carrying out the measurements, the following (Figure 5.7) results were obtained

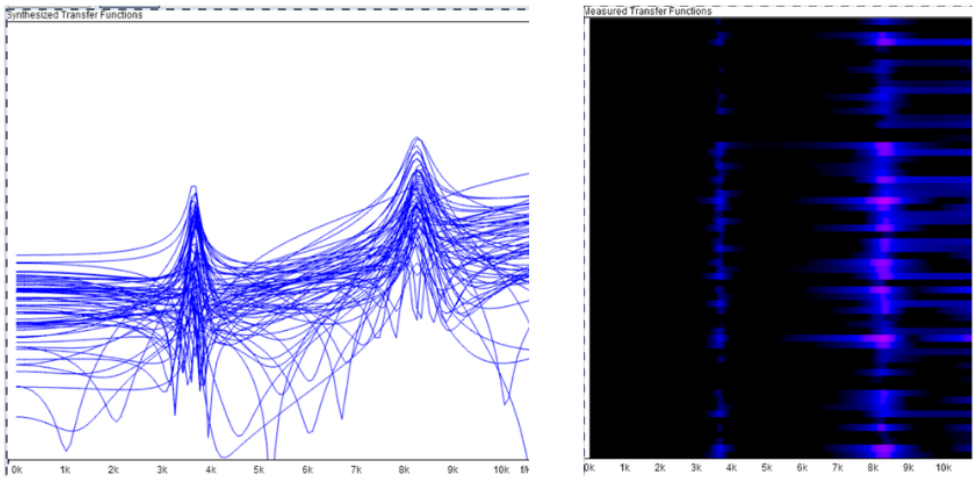


Figure 5.7: Measured transfer function - Shaft and accessories - axial vibrations

For the purpose of extracting the stable poles, only four sensors are considered due to the presence of a noisy signal.With this premise, it was then possible to derive the transfer-function and the stability diagram (Figure 5.8)

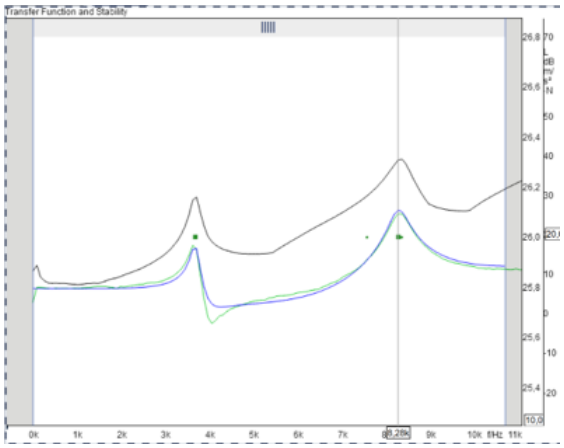


Figure 5.8: Transfer function and stability diagram - shaft and accessories - axial vibrations

from which the following (Table 5.6 modal parameters can be derived:

Modal Parameters		
Shape Name	**Frequency [Hz]**	**Damping - ξ - [%]**
Mode shape 1	3680	2.2
Mode shape 2	8276	2.4

Table 5.6: Modal parameters of the rotating components - axial vibrations

5.4 Casing

In Figure 5.9, the experimental setup adopted for the modal analysis of the casing is shown. This configuration differs from the previous one because the component is significantly bulkier and heavier; as a consequence, it would excessively compress the sponge, compromising the reliability of the simulated boundary conditions. For these reasons, a more suitable support was employed—an air cushion typically used in industrial packaging—which provides a behaviour very close to the free–free condition required for modal analysis.

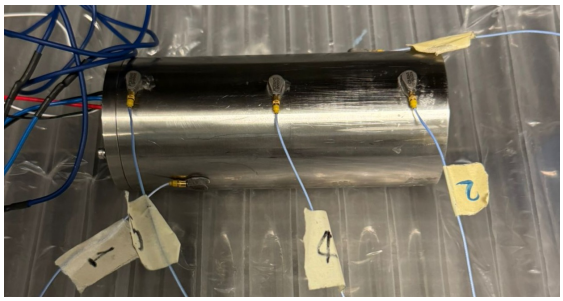


Figure 5.9: Experimental setup casing radial vibrations

For this setup, 59 degrees of freedom were excited, five sensors were installed. After carrying out the measurements, the following (Figure 5.10) results were obtained

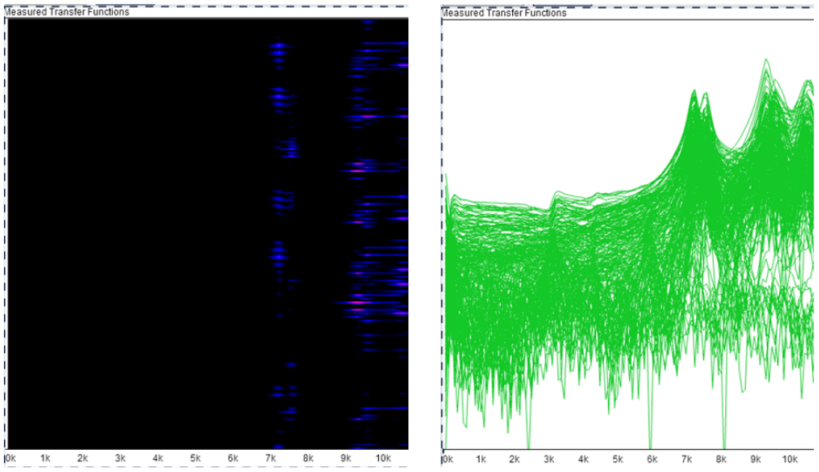


Figure 5.10: Measured transfer functions - Casing

As in the previous case, in this figure, highly noisy signals can be identified in the lower portion. Consequently, they were removed in order to facilitate the interpolation process required to obtain stable poles. With this premise, it was then possible to derive the transfer-function and the stability diagram (Figure 5.11)

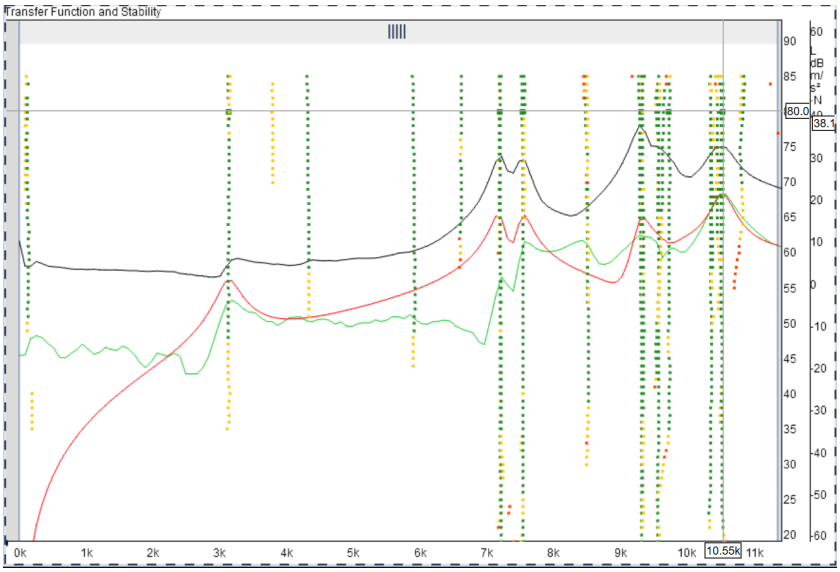


Figure 5.11: Transfer function and stability diagram - Casing

from which the following (Table 5.7) modal parameters can be derived:

Modal Parameters		
Shape Name	**Frequency [Hz]**	**Damping - ξ - [%]**
Mode shape 1	3137	4.7
Mode shape 2	7197	1.3
Mode shape 3	7547	1.3
Mode shape 4	9325	1.0
Mode shape 5	10547	1.3

Table 5.7: Modal parameters of the casing

5.5 Spindle assembly

In Figure 5.12 & 5.15, it can be observed that the experimental setup adopted for this case closely replicates that used for the casing, namely an air plastic pad. As in the case of the rotating components on the shaft, two vibration measurement directions—axial and radial—were considered. Consequently, different excitation points and sensor locations were selected in the two configurations.

5.5.1 Radial vibrations

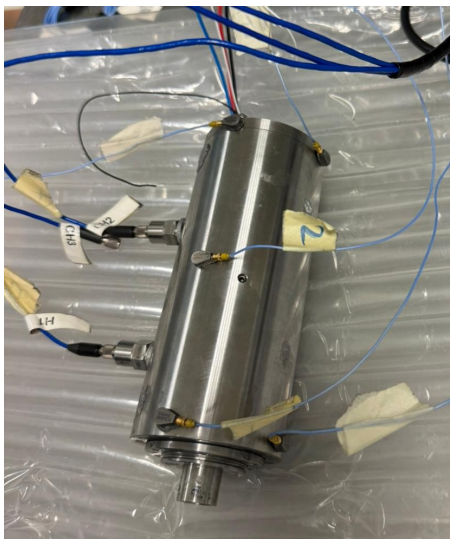


Figure 5.12: Experimental setup - Spindle - radial vibrations

For this setup, 30 positions were excited, seven monoaxial sensors were installed.

After carrying out the measurements, the following (Figure 5.13) results were obtained

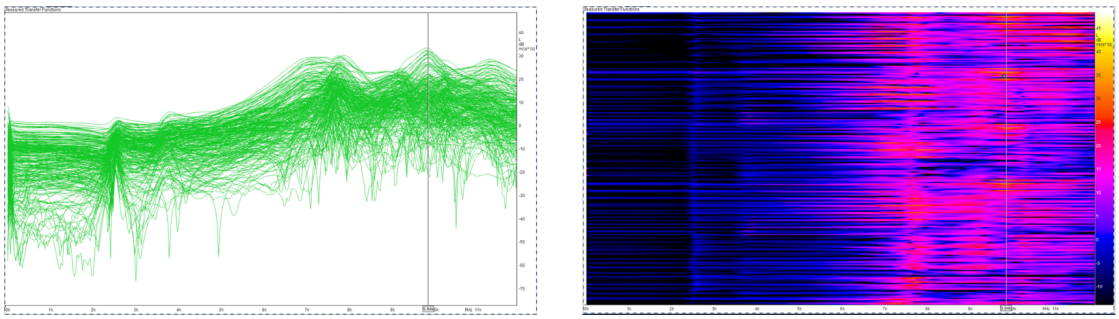


Figure 5.13: Measured transfer functions - Spindle - radial vibrations

The measurements obtained from the sensor located on the upper part of the spindle, in the DE area, are not taken into consideration because they are affected by excessive noise. With this premise, it was then possible to derive the transfer-function and the stability diagram (Figure 5.14)

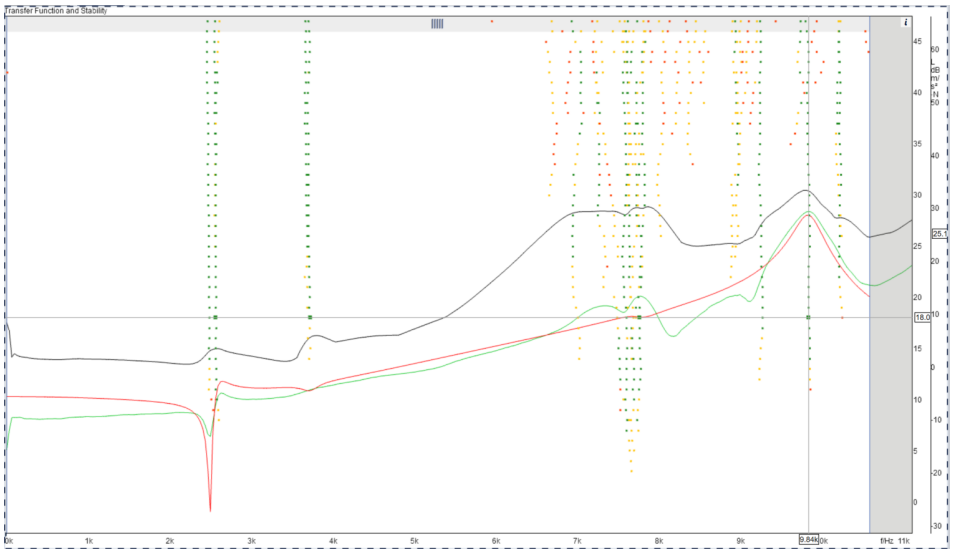


Figure 5.14: Transfer function and stability diagram - Spindle - radial vibrations

from which the following (Table 5.8) modal parameters can be derived:

Modal Parameters		
Shape Name	**Frequency [Hz]**	**Damping - ξ - [%]**
Mode shape 1	2564	2.9
Mode shape 2	3726	3.7
Mode shape 3	7767	2.2
Mode shape 4	9273	1.6
Mode shape 5	9843	1.6

Table 5.8: Modal parameters of the spindle - radial vibrations

5.5.2 Axial vibrations

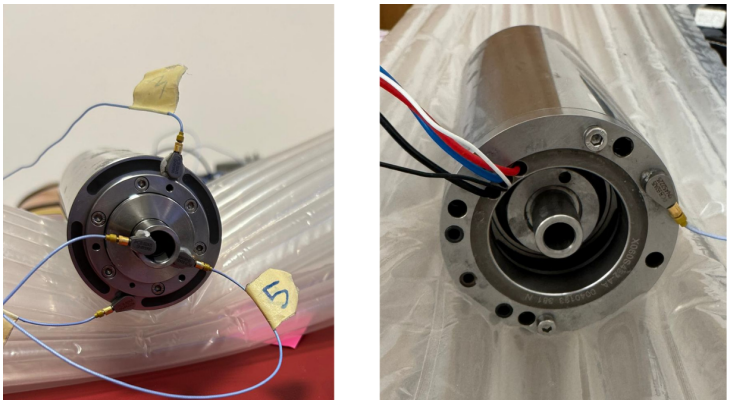


Figure 5.15: Experimental setup - Spindle - axial vibrations

For this setup, 31 points were excited and 4 sensors were installed. After carrying out the measurements, the following (Figure 5.16) results were obtained

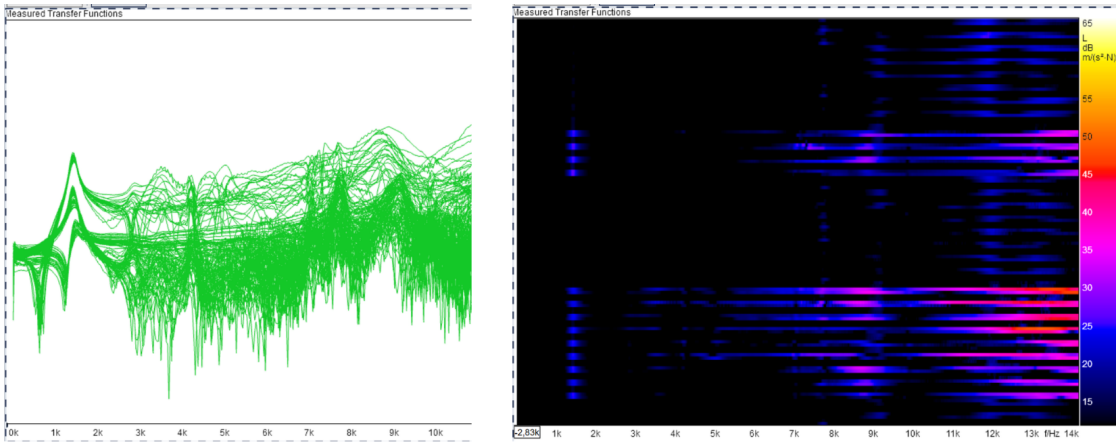


Figure 5.16: Measured transfer functions - Spindle - axial vibrations

In this case, only three of the four sensors employed proved to be effective, as they recorded signals with no significant noise component. Consequently, only these sensors contributed to the identification of the system's modal parameters. With this premise, it was then possible to derive the transfer-function and the stability diagram (Figure 5.17)

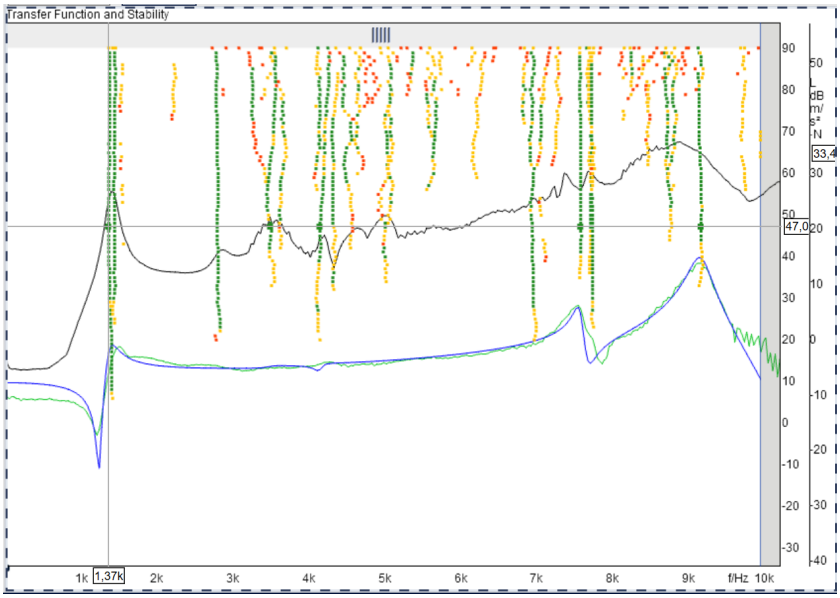


Figure 5.17: Transfer function and stability diagram - Spindle - axial vibrations

from which the following (Table 5.9) modal parameters can be derived:

Modal Parameters		
Shape Name	**Frequency [Hz]**	**Damping - ξ - [%]**
Mode shape 1	1372	5.9
Mode shape 2	3498	5.0
Mode shape 3	4158	1.7
Mode shape 4	7585	0.9
Mode shape 5	9172	1.6

Table 5.9: Modal parameters of the spindle - axial

5.6 Decoupling the shaft and casing motion

The purpose of these analyses is precisely to decouple the motion of the shaft located inside the casing from that of the casing itself, in order to understand how the two components move relative to each other. As in the previous cases, the axial vibrational modes were separated from the radial ones and, for each category, the following measurements were performed:

- Excitation on the casing with the sensors mounted on the casing
- Excitation on the casing with the sensors mounted on the shaft
- Excitation on the shaft with the sensors mounted on the casing
- Excitation on the shaft with the sensors mounted on the shaft

The sensors were positioned symmetrically in order to reduce interpolation errors in the software during the extraction of stable poles, and their placement was determined to ensure an almost complete coverage of the surface. For each analysis, a different sensor layout was selected to highlight the characteristics of the system while, as far as possible, avoiding nodal points.

5.6.1 Radial vibrations

Casing to casing

Figure 5.18 shows how are sensors located on the outer surface of the casing.

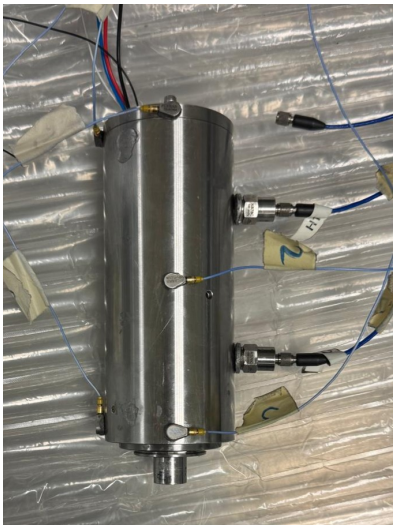


Figure 5.18: Sensors placement on the casing in the radial direction

For this analysis, 26 excitation points and 7 sensors were considered. After carrying out the measurements, the following (Figure 5.19) results were obtained.

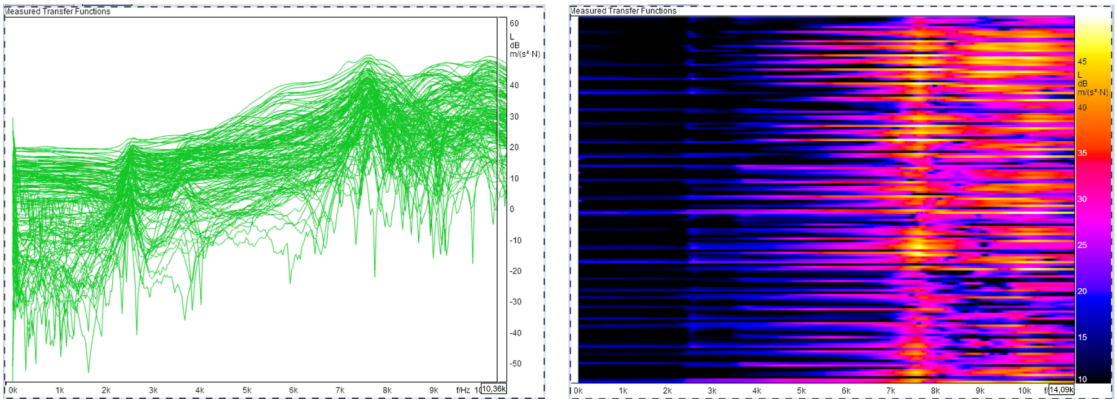


Figure 5.19: Measured transfer functions - Casing to casing - radial vibrations

Recordings from one channel have been discarded because of the noise, thus just 6 sensors out of 7 are active. With this premise, it was then possible to derive the transfer-function and the stability diagram (Figure 5.20)

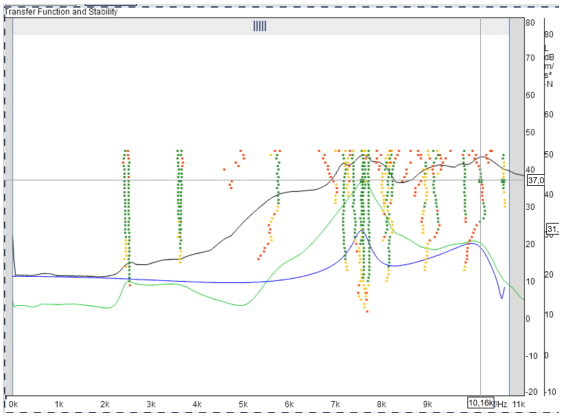


Figure 5.20: Transfer function and stability diagram - Casing to casing - radial vibrations

from which the following (Table 5.10) modal parameters can be derived

Modal Parameters		
Shape Name	**Frequency [Hz]**	**Damping - ξ - [%]**
Mode shape 1	2517	4.0
Mode shape 2	7587	2.0

Table 5.10: Modal parameters of the spindle - Casing to casing - radial

Casing to shaft

Figure 5.21 shows how are sensors located on the shaft.

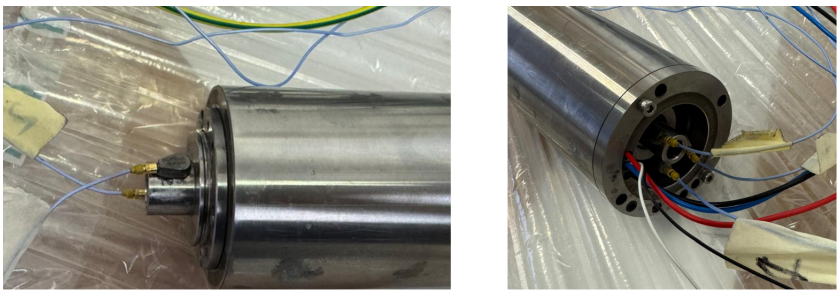


Figure 5.21: Sensors placement on the shaft in the radial direction

In this analysis, 26 excitation points and 4 sensors were considered. After carrying out the measurements, the following (Figure 5.22) results were obtained

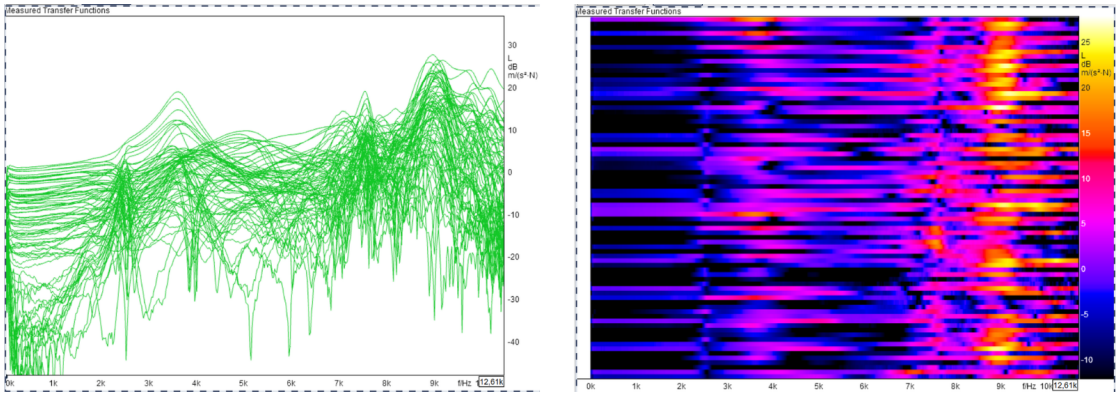


Figure 5.22: Measured transfer functions - Casing to shaft - radial

One sensor provided with very noisy signals, thus, just 3 sensors out of 4 are active. With this premise, it was then possible to derive the transfer-function and the stability diagram (Figure 5.23)

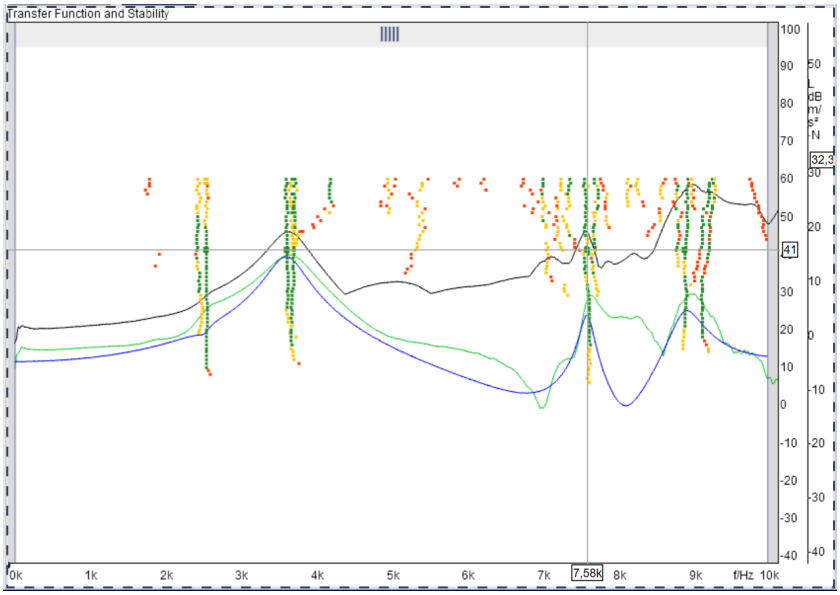


Figure 5.23: Transfer function and stability diagram - Casing to shaft - radial direction

from which the following (Table 5.13) modal parameters can be derived

Modal Parameters		
Shape Name	**Frequency [Hz]**	**Damping - ξ - [%]**
Mode shape 1	2533	4.1
Mode shape 2	3597	6.3
Mode shape 3	7581	1.1
Mode shape 4	8875	2.1

Table 5.11: Modal parameters of the spindle - Casing to shaft - radial

Shaft to casing

The sensors placement is the same as Figure 5.18, just with different excitation points. For this analysis, 26 excitation points and 5 sensors were considered. After carrying out the measurements, the following (Figure 5.25) results were obtained.

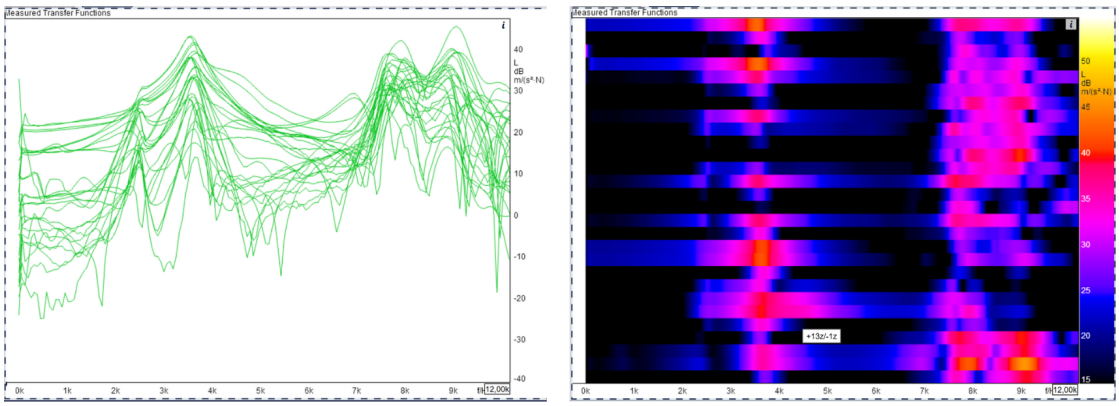


Figure 5.24: Measured transfer functions - Shaft to casing - radial direction

Two sensors provided with very noisy signals, thus, just 3 sensors out of 5 are active. With this premise, it was then possible to derive the transfer-function and the stability diagram (Figure 5.25).

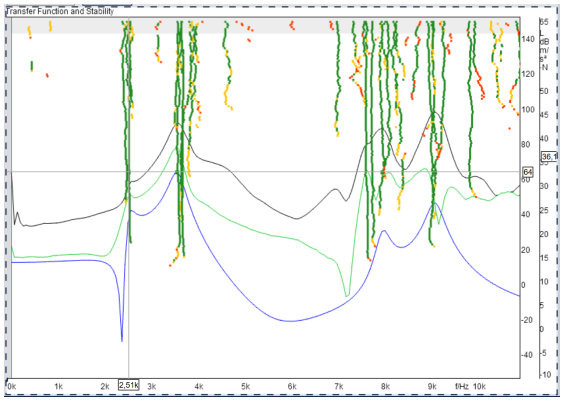


Figure 5.25: Transfer function and stability diagram - Shaft to casing - radial

from which the following (Table 5.13) modal parameters can be derived

Modal Parameters		
Shape Name	**Frequency [Hz]**	**Damping - ξ - [%]**
Mode shape 1	2510	3.4
Mode shape 2	3554	4.5
Mode shape 3	7948	1.7
Mode shape 4	9071	1.9

Table 5.12: Modal parameters of the spindle - Casing to shaft - radial

Shaft to shaft

The sensors placement is the same as Figure 5.21, just with different excitation points. For this analysis, 9 excitation points and 4 sensors were considered. After carrying out the measurements, the following (Figure 5.26) results were obtained.

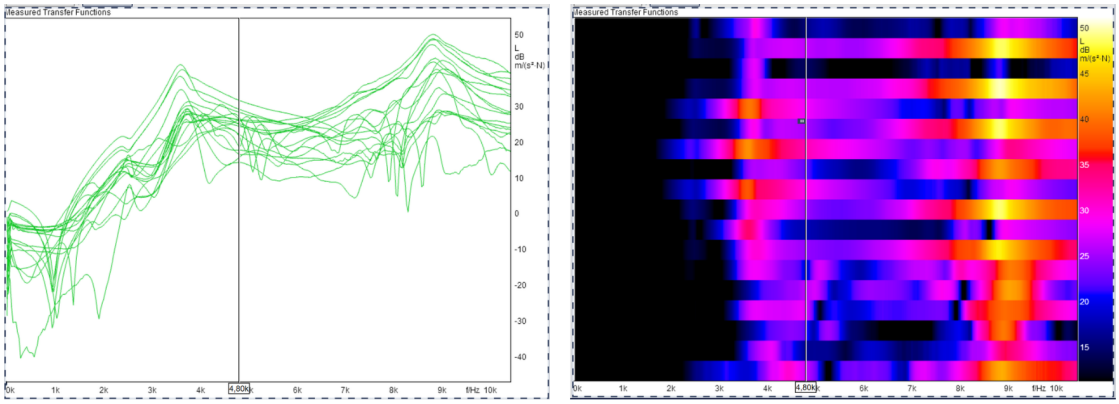


Figure 5.26: Measured transfer functions - shaft to shaft - radial

Two sensors provided with very noisy signals, thus, just 2 sensors out of 4 are active. With this premise, it was then possible to derive the transfer-function and the stability diagram (Figure 5.27).

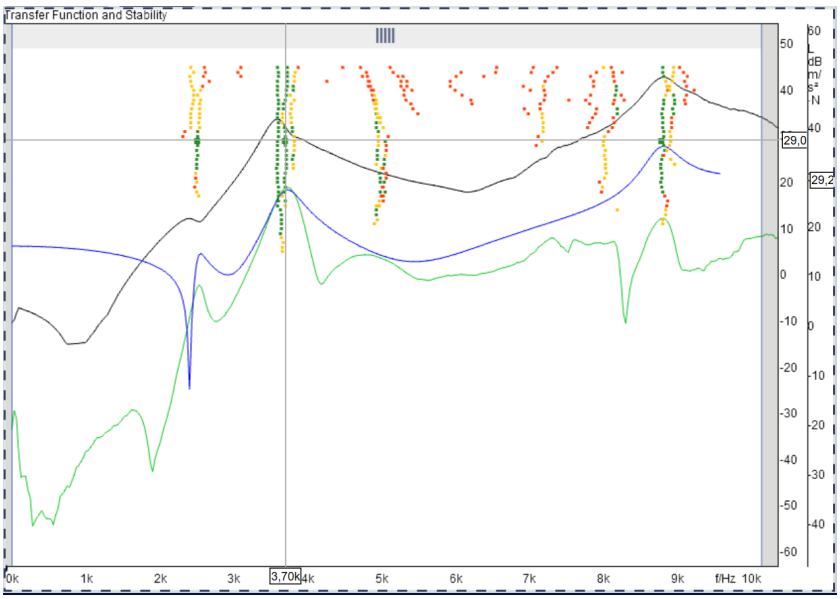


Figure 5.27: Transfer function and stability diagram - shaft to shaft - radial

from which the following (Table 5.13) modal parameters can be derived

Modal Parameters		
Shape Name	**Frequency [Hz]**	**Damping - ξ - [%]**
Mode shape 1	2505	3.1
Mode shape 2	3704	5.3
Mode shape 3	8792	2.5

Table 5.13: Modal parameters of the spindle - Casing to shaft - radial

5.6.2 Axial vibrations

Casing to casing

Figure 5.28 shows sensors located on the outer surface of the casing.

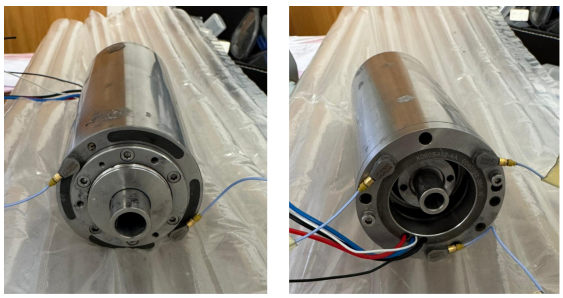


Figure 5.28: Sensors placement on the casing in the axial direction

For this analysis, 24 excitation points and 5 sensors were considered. After carrying out the measurements, the following (Figure 5.29) results were obtained.

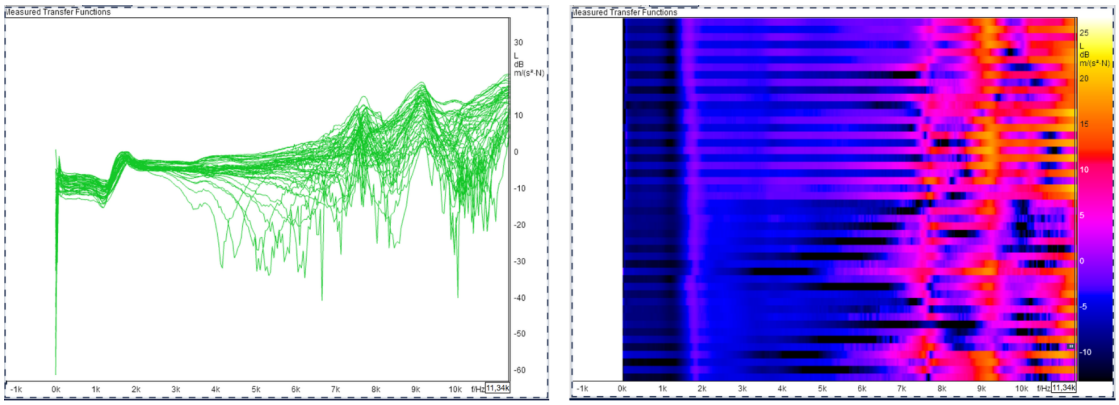


Figure 5.29: Measured transfer functions - Casing to casing - axial vibrations

Recordings from three channels have been discarded because of the noise, thus just 2 sensors out of 5 are active.With this premise, it was then possible to derive the transfer-function and the stability diagram (Figure 5.30).

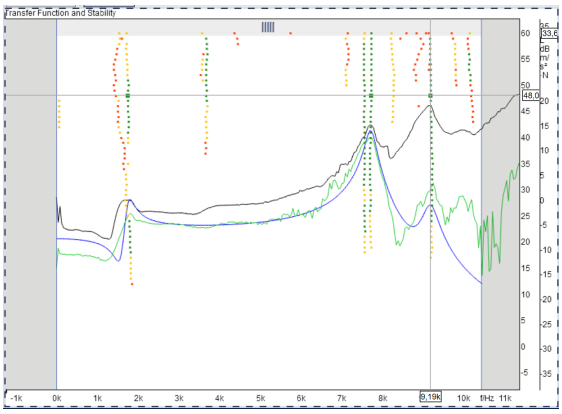


Figure 5.30: Transfer function and stability diagram - Casing to casing - axial vibrations

from which the following (Table 5.14) modal parameters can be derived

Modal Parameters		
Shape Name	**Frequency [Hz]**	**Damping - ξ - [%]**
Mode shape 1	1757	5.2
Mode shape 2	7719	1.7
Mode shape 3	9216	2.2

Table 5.14: Modal parameters of the spindle - Casing to casing - axial

Casing to shaft

Figure 5.31 shows sensors located on the shaft.

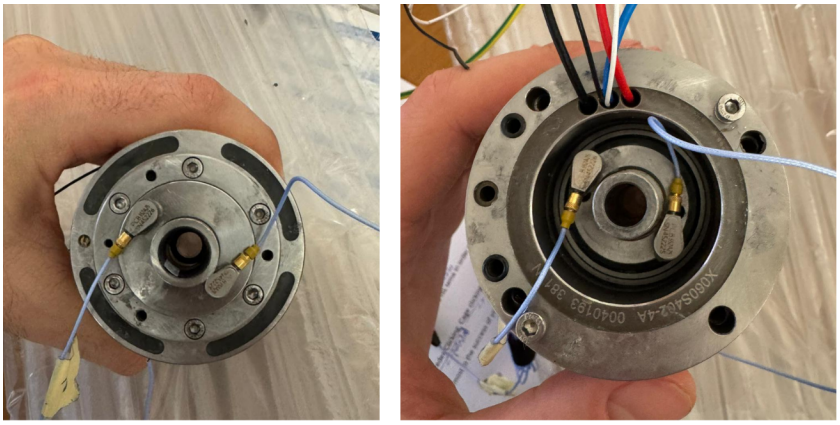


Figure 5.31: Sensors placement on the shaft in the axial direction

In this analysis, 24 excitation points and 4 sensors were considered. After carrying out the measurements, the following (Figure 5.32) results were obtained.

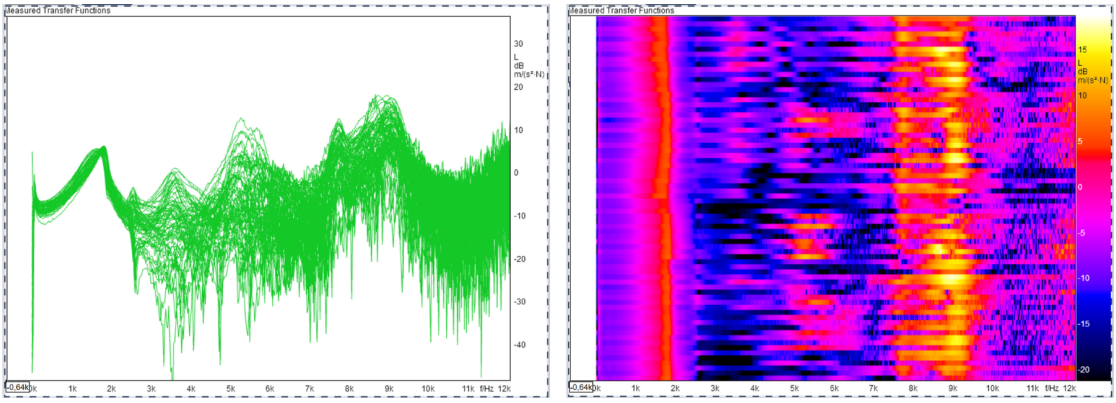


Figure 5.32: Measured transfer functions - Casing to shaft - axial

For this analysis all the sensors provided with quality recordings, thus no one is discarded. With this premise, it was then possible to derive the transfer-function and the stability diagram (Figure 5.33).

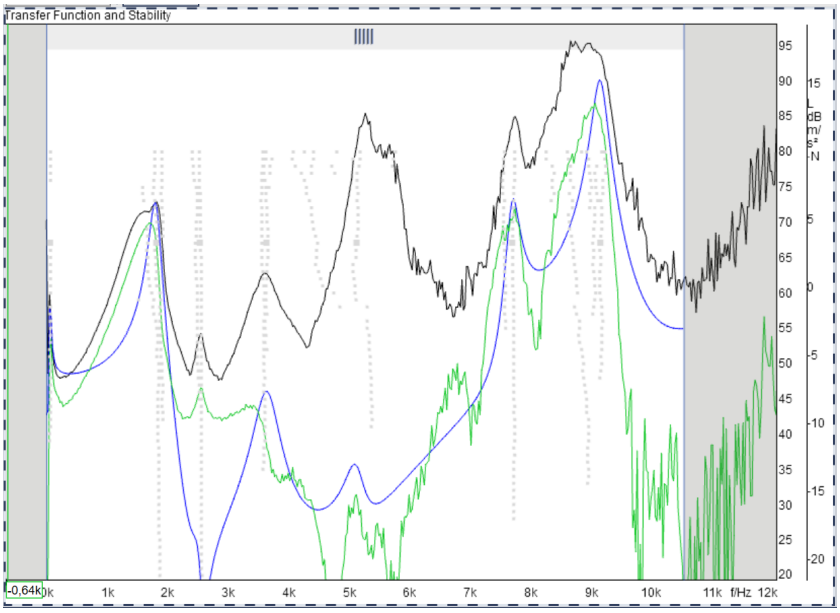


Figure 5.33: Transfer function and stability diagram - Casing to shaft - axial direction

from which the following (Table 5.17) modal parameters can be derived

Modal Parameters		
Shape Name	**Frequency [Hz]**	**Damping - ξ - [%]**
Mode shape 1	56	17.4
Mode shape 2	1809	5.1
Mode shape 3	2541	3.5
Mode shape 4	3646	5.4
Mode shape 5	5132	3.4
Mode shape 6	7707	1.3
Mode shape 7	9162	1.4

Table 5.15: Modal parameters of the spindle - Casing to shaft - axial

Shaft to casing

The sensors placement is the same as Figure 5.28, just with different excitation points. For this analysis, 12 excitation points and 4 sensors were considered. After carrying out the measurements, the following (Figure 5.34) results were obtained.

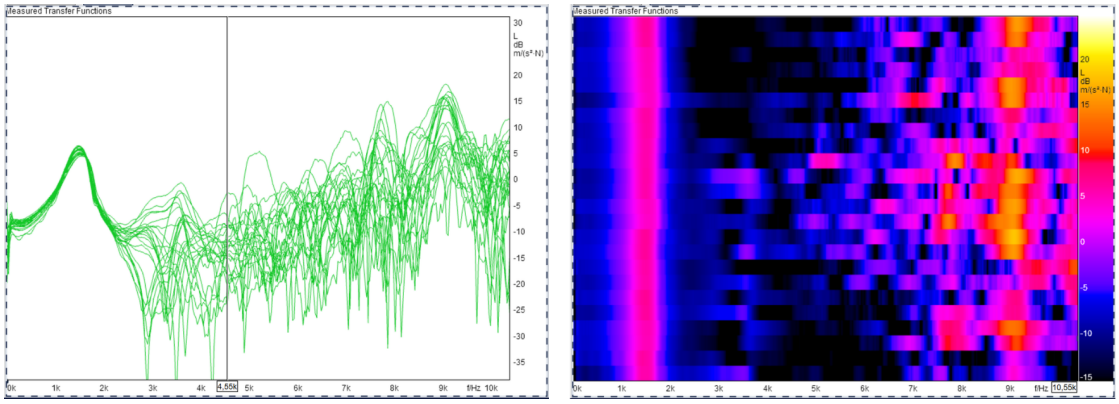


Figure 5.34: Measured transfer functions - Shaft to casing - axial direction

Two sensors provided with very noisy signals, thus, just 2 sensors out of 4 are active. With this premise, it was then possible to derive the transfer-function and the stability diagram (Figure 5.35).

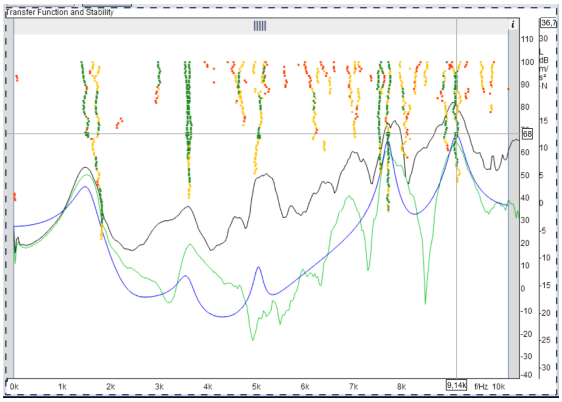


Figure 5.35: Transfer function and stability diagram - Shaft to casing - axial

from which the following (Table 5.17) modal parameters can be derived

Modal Parameters		
Shape Name	**Frequency [Hz]**	**Damping - ξ - [%]**
Mode shape 1	1522	13.7
Mode shape 2	3584	4.9
Mode shape 3	5058	1.8
Mode shape 4	7727	1.1
Mode shape 5	9141	1.5

Table 5.16: Modal parameters of the spindle - Casing to shaft - axial

Shaft to shaft

The sensors placement is the same as Figure 5.31, just with different excitation points. For this analysis, 12 excitation points and 4 sensors were considered. After carrying out the measurements, the following (Figure 5.36) results were obtained.

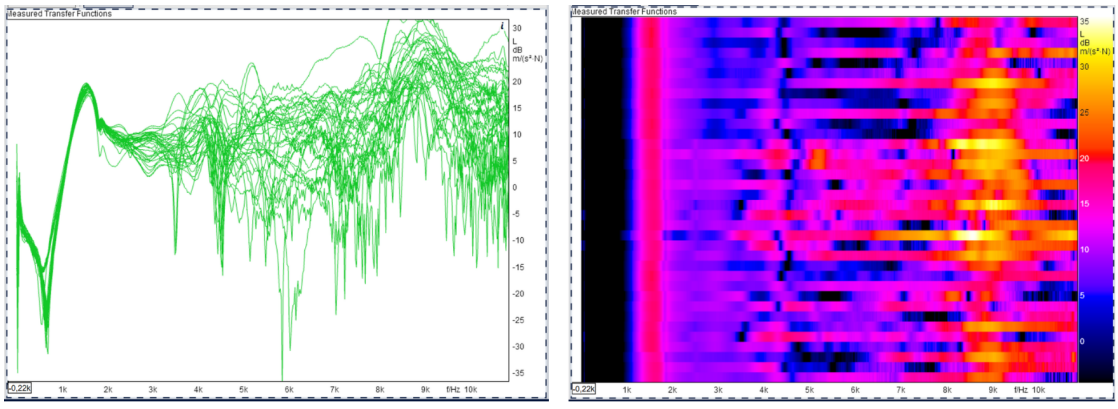


Figure 5.36: Measured transfer functions - shaft to shaft - axial

One sensor provided with very noisy signals, thus, just 3 sensors out of 4 are active. With this premise, it was then possible to derive the transfer-function and the stability diagram (Figure 5.37).

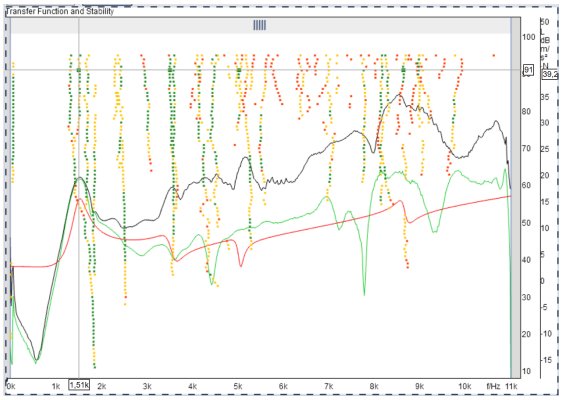


Figure 5.37: Transfer function and stability diagram - shaft to shaft - axial

from which the following (Table 5.17) modal parameters can be derived

Modal Parameters		
Shape Name	**Frequency [Hz]**	**Damping - ξ - [%]**
Mode shape 1	1513	8.8
Mode shape 2	3512	4.8
Mode shape 3	5039	1.9
Mode shape 4	8654	1.2

Table 5.17: Modal parameters of the spindle - Casing to shaft - axial

5.7 Spindle in rotation

Operating-condition tests are inherently complementary to experimental modal analysis because they reveal how the structure actually deforms and responds under the true forcing conditions, boundary constraints, and thermal states encountered in service, thereby bridging the gap between idealized modal parameters and real operational behavior. While modal analysis identifies natural frequencies, damping ratios, and mode shapes under controlled excitation and often simplified constraints, operating deflection shapes (ODS) show the actual vibration patterns at the frequencies excited during operation, enabling the visualization of deformation fields, the detection of localized issues such as looseness, imperfect contacts, or misalignments, and the assessment of how multiple modes combine. In parallel, the Campbell diagram situates these observations across the speed range by mapping the evolution of natural frequencies with rotational speed and superimposing the

lines associated with rotational harmonics, the so called orders, thus allowing the identification of critical speeds, the separation of forward and backward whirl due to gyroscopic effects, and the recognition of potential resonances when excitation lines intersect natural frequencies. Together, ODS and Campbell analysis provide diagnostic and prognostic insight that static modal parameters alone cannot supply: ODS ties the measured operational responses to spatial deformation patterns near bearings and other critical regions, while the Campbell diagram contextualizes those responses across operating speeds, validates or refines rotor–bearing models, and guides decisions on start-up/shut-down strategies and allowable operating ranges to avoid excessive amplitudes or instability. Consequently, the integration of operating-condition testing with modal analysis yields a more faithful representation of the system's dynamic behavior, improves fault localization and root-cause analysis, and supports robust design and condition-based maintenance. This experiment differs from the previous tests because the spindle is no longer stationary but rotates according to two predefined loading cycles. The first cycle consists of:

- a run-up from 0 to 10 kHz in 90 s,
- a steady-state condition at a constant speed of 10 kHz for 40 s,
- a coast-down to zero speed by disconnecting the electrical supply.

Two steel supports coated with a thin rubber layer were employed to isolate the vibrations of the base from those of the spindle, and they were positioned at a distance sufficient to prevent bending effects while ensuring a structurally rigid configuration. It should be noted that, for radial measurements, only a single support was placed at the central section of the spindle, whereas two supports were adopted for axial vibration measurements in order to enhance measurement accuracy (Figure 5.38). The sensors were also placed strategically to avoid nodal points and to acquire vibration measurements near the bearings, where the dynamic response is most representative.

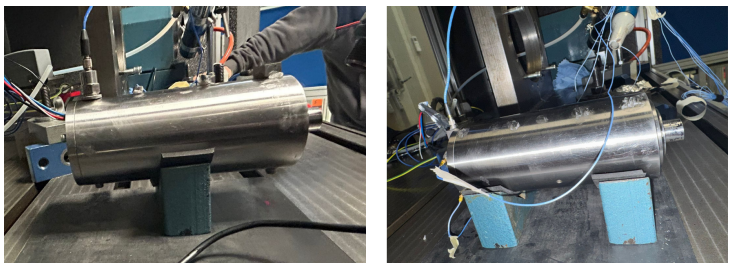


Figure 5.38: Experimental setup - Rotating spindle

For this experiment, small single-axis sensors mounted with wax were used in addition to two larger single-axis sensors affixed with adhesive. This configuration

was adopted because the spindle tends to heat up during operation, causing wax-mounted sensors to loosen or detach, whereas the adhesive-mounted sensors ensured stable measurements throughout the tests. The spindle was not cooled by circulating refrigerant fluid inside its internal channels; instead, the surrounding environment was cooled by a device that injected cold air directly into the working chamber. This approach prevented the temperature from rising excessively and avoided overheating issues while also eliminating the additional mass that an internal cooling system would have introduced, thereby preserving the dynamic characteristics of the system but affecting the boundary conditions of the whole system.

5.7.1 Campbell diagram

The Campbell diagram provides a comprehensive representation of the vibrational behaviour of a rotating system by combining frequency-domain information derived from FFT analysis with the corresponding time-domain measurements acquired at different rotational speeds. In its linear-scale form, the diagram plots the evolution of vibration frequencies as a function of spindle speed, allowing the identification of synchronous components, harmonic orders, and potential resonances. This graphical representation highlights how natural frequencies shift with rotation and how operational excitations evolve over time, offering an essential tool for interpreting the dynamic response of the spindle under real operating conditions.

Radial vibrations

To measure the vibrations under operating conditions in the radial direction, the sensors were positioned strategically. Specifically, they were arranged on the casing every 90 degrees in pairs separated by 180 degrees, meaning that the radial direction was captured vertically (top and bottom) and horizontally (right to left and vice versa), as illustrated in Figure 5.39. The chosen reference was the cubic triaxial sensor mounted on the casing towards the driven end.

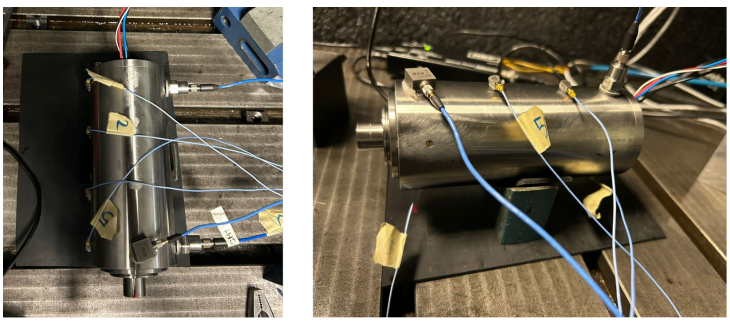


Figure 5.39: Sensors positioning for radial vibrations

Consequently, it was possible to obtain the following (Figure 5.40) Campbell diagram.

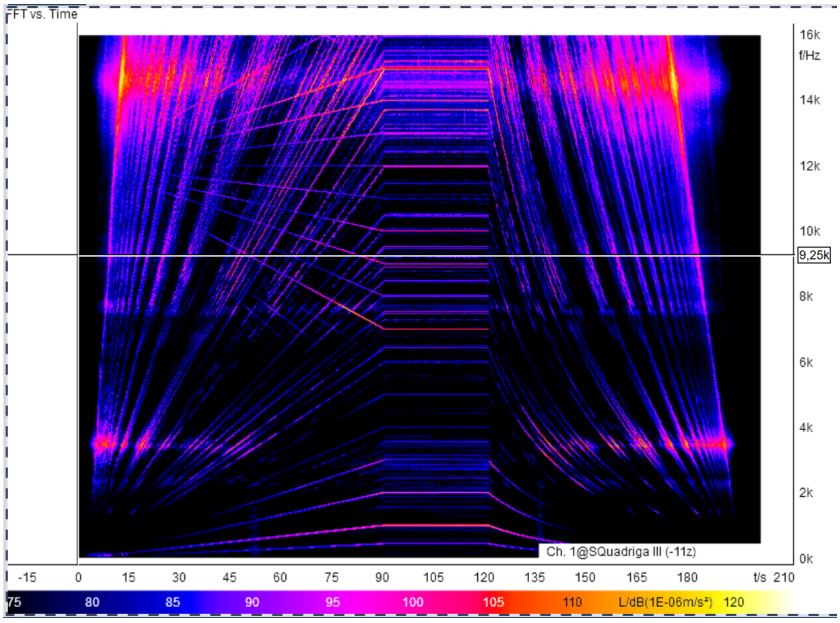


Figure 5.40: Campbell diagram in radial direction

Axial vibrations

Regarding the vibrations in the axial direction, as Figure 5.41 shows, the sensors were positioned on the rear side of the spindle (NDE side) and, on the front part, on the casing and the flange, since these components do not rotate. The chosen reference was the cubic triaxial sensor mounted on the upper rear section of the spindle.

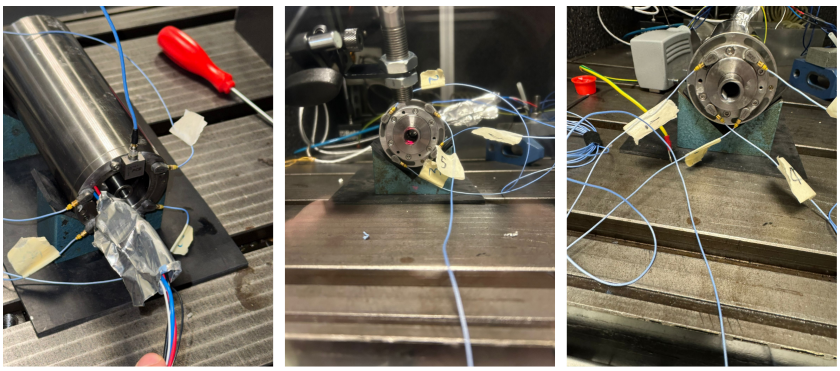


Figure 5.41: Sensors positioning for radial vibrations

Consequently, it was possible to obtain the following (Figure 5.42) Campbell diagram.

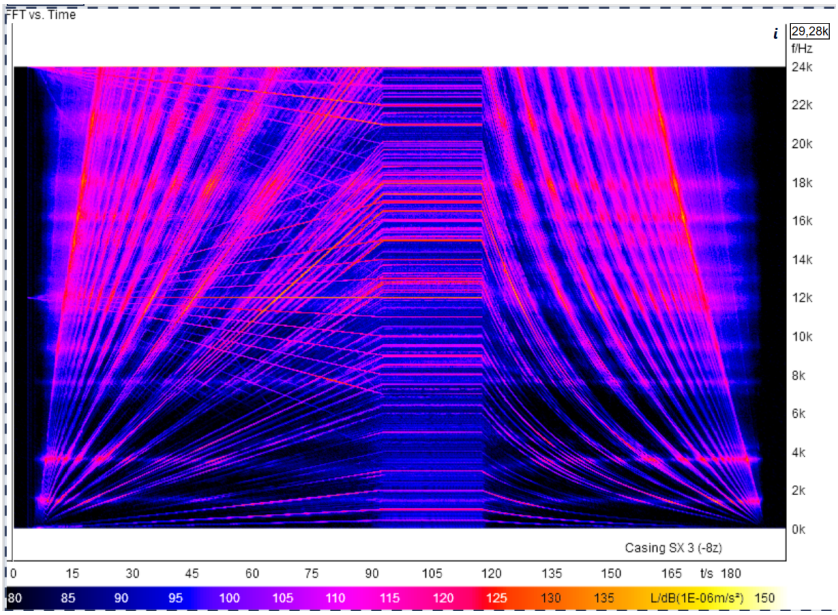


Figure 5.42: Campbell diagram in axial direction

5.7.2 Operating deflection shapes

To determine the various operating deflection shapes, the autospectra are analysed, as the autospectrum constitutes the fundamental tool for extracting the operational frequencies that are subsequently used to reconstruct the ODS and to identify the frequencies at which it is meaningful to visualize the structural deformation. These autospectra originate from the same measurements employed to construct the Campbell diagram and were acquired on the spindle under rotating conditions. When interpreting an autospectrum, the focus lies on identifying the frequency peaks that correspond to the dominant components of the vibratory response. Peaks at harmonics of the rotational speed indicate synchronous excitations (e.g., imbalance at 1×, misalignment at 2×), whereas broadband increases or sharp isolated peaks may signal resonant phenomena or localised defects. The amplitude distribution across the frequency axis therefore provides direct insight into which frequencies should be selected for ODS reconstruction, as only those associated with clearly identifiable and dynamically relevant peaks can yield meaningful deformation patterns.

Radial shapes

The colormap in Figure 5.43 is helpful in determining the deflection shapes.

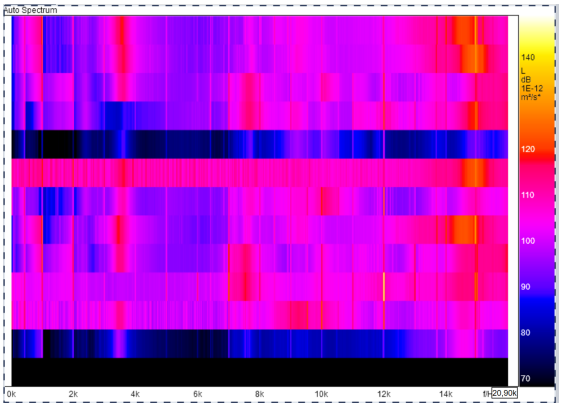


Figure 5.43: Auto spectrum for radial excitations

In fact, the following (Table 5.18) frquencies are identified:

Shape Parameters	
Shape Name	**Frequency [Hz]**
Shape 1	2344
Shape 2	3585
Shape 3	7805
Shape 4	9164

Table 5.18: Operating Deflection Shape - radial

Axial shapes

The colormap in Figure 5.44 is helpful in determining the deflection shapes.

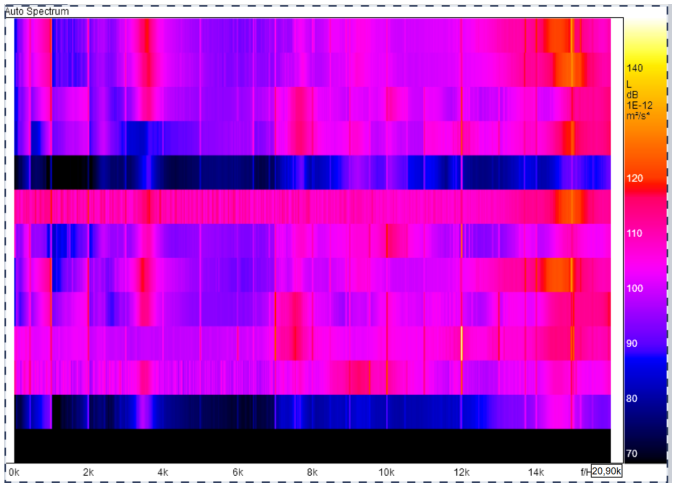


Figure 5.44: Auto spectrum for axial excitations

In fact, the following (Table 5.19) frequencies are identified:

Shape Parameters	
Shape Name	**Frequency [Hz]**
Shape 1	1528
Shape 2	3720
Shape 3	7681
Shape 4	9487

Table 5.19: Operating Deflection Shape - axial

Chapter 6

Numerical modeling of the case study

6.1 Introduction

The mechanical behaviour of rolling bearings results from the interaction between structural flexibility, nonlinear contact forces, lubrication phenomena and geometrical imperfections on the rolling elements and raceways. The numerical model implemented in SKF SimPro Expert is designed to reproduce this coupled behaviour with a high degree of fidelity, while remaining computationally efficient enough to be applied to complete mechanical systems such as rotor–bearing–housing assemblies. The theoretical formulation relies on the combination of four fundamental components: the equations of motion for a flexible multibody system; Hertzian and elastohydrodynamic lubrication theory for the contact forces and stiffness; harmonic representations of geometrical imperfections; and the Component Mode Synthesis (CMS) reduction technique adapted specifically by SKF to handle moving, rotating and time-varying contact interfaces. This chapter is primarily based on the theoretical framework developed by Wensing (1998) [7], whose work provides the foundation for the analytical CMS approach, the EHL-based descriptions of contact stiffness and damping, and the harmonic treatment of geometric deviations. The following chapter provides a complete and discursive description of the theoretical foundation of this model, including governing equations, lubrication theory, nonlinear contact representations, the specialised CMS formulation, and the treatment of localised defects and waviness.

6.2 Governing Equations of the System

The complete bearing application consists of a rotating flexible shaft supported by rolling bearings, whose outer rings are themselves supported by flexible housings. The system is governed by Lagrange's equations applied to the total kinetic, potential and dissipated energy.

Let the set of generalised coordinates of the complete system be $\mathbf{p}$, including the reduced modal coordinates of the shaft, the reduced modal coordinates of each housing, the rigid-body coordinates of the inner ring, and the translational coordinates of every rolling element. The equations of motion are written as:

$$\frac{d}{dt}\left(\frac{\partial T}{\partial \dot{\mathbf{p}}}\right) - \frac{\partial T}{\partial \mathbf{p}} + \frac{\partial V}{\partial \mathbf{p}} + \frac{\partial F}{\partial \dot{\mathbf{p}}} = \mathbf{Q},$$

where T denotes the kinetic energy, V the elastic potential energy, F Rayleigh's dissipation function and $\mathbf{Q}$ the vector of external generalised forces.

After CMS reduction of the flexible components, the global system takes the matrix form:

$$\mathbf{M}\,\ddot{\mathbf{p}} + \mathbf{C}\,\dot{\mathbf{p}} + \mathbf{K}\,\mathbf{p} = \mathbf{F}_{\mathrm{nl}}(\mathbf{p}, \dot{\mathbf{p}}, t) + \mathbf{R}(t).$$

The matrix $\mathbf{M}$ collects the reduced mass contributions of the shaft, the housings and the rigid-body inertia of the inner ring; $\mathbf{C}$ gathers structural damping and the viscous contributions of the elastohydrodynamic contacts; $\mathbf{K}$ contains the linearised structural and contact stiffnesses; $\mathbf{F}_{\mathrm{nl}}$ embodies the full nonlinear normal and tangential forces at the contacts; and $\mathbf{R}(t)$ accounts for applied loads, centrifugal forces of the rolling elements and any imposed accelerations.

6.3 Contact Mechanics

6.3.1 Hertzian Elastic Contact

The elastic part of the contact force is based on a Hertzian point-contact formulation. Let δ be the elastic mutual approach between the rolling element and the raceway, defined as the relative displacement between their centers of curvature, adjusted to account for deformations of the contacting surfaces The normal elastic force follows the classical power law:

$$F_{\mathrm{e}} = \kappa\,\delta^{3/2},$$

where κ depends on the reduced radius of curvature and the reduced elastic modulus of the two contacting bodies.

The Hertzian theory also establishes the distribution of pressure in the contact ellipse, from which local contact stresses, deformed shape and stiffness can be derived. While Hertzian theory neglects lubrication and assumes frictionless normal loading, it provides the baseline for all subsequent EHL modifications.

6.3.2 Elastohydrodynamic Lubrication

Under normal operating conditions, rolling bearings operate in the elastohydrodynamic lubrication regime. The lubricant forms a thin film whose thickness and pressure distribution are coupled to the elastic deformation of the surfaces.

The EHL problem is governed by three coupled equations. The first is the Reynolds equation for the pressure field $p(x, y)$:

$$\frac{\partial}{\partial x}\left(\frac{\rho\, h^3}{\eta}\frac{\partial p}{\partial x}\right) + \frac{\partial}{\partial y}\left(\frac{\rho\, h^3}{\eta}\frac{\partial p}{\partial y}\right) = 6\rho\, U\frac{\partial h}{\partial x} + 12\rho\,\frac{\partial h}{\partial t},$$

where η is the pressure-dependent viscosity, h the gap thickness, ρ the density and U the sum velocity of the surfaces.

The gap function is expressed as:

$$h(x, y, t) = \delta(t) + \frac{x^2}{2R_x} + \frac{y^2}{2R_y} + d(x, y, t),$$

where $d(x, y, t)$ is the surface elastic deformation obtained from the Boussinesq integral.

The third equation is the dynamic force balance on the rolling element:

$$m\,\ddot{\delta} + \int p(x, y)\, dx\, dy = F_{\text{ext}}(t).$$

The full solution of this system is computationally intensive and unsuitable for repeated time-domain integration in a full bearing model. For this reason, SKF adopts a dimensionless curve-fit representation of the EHL behaviour, based on extensive numerical studies.

6.3.3 Dimensionless EHL Stiffness Model

The EHL mutual approach is written in dimensionless form as:

$$\Lambda = 1 - p(L)\, N^{-1/2},$$

where N is the dimensionless load parameter and L the pressure-viscosity parameter. The curve-fit representation links the elastic force F_{e} to the equivalent mutual approach via:

$$\Lambda(N, L) = 1 - p(L)\, N^{-q(L)},$$

with $p(L)$ and $q(L)$ empirical functions obtained from numerical EHL solutions.

This yields a smooth transition between full Hertzian stiffness and the more compliant behaviour at low or negative approach values, which arise in low-load, high-speed conditions.

6.3.4 Viscous Damping in the Lubricated Contact

Energy dissipation occurs mainly through viscous shearing in the entrance region of the EHL contact. A linear viscous damper is introduced:

$$F_{\mathrm{d}} = c\,\dot{\delta},$$

with the damping coefficient expressed in dimensionless form as:

$$C(N, L) = r(L)\,N^{-s(L)}.$$

These empirical expressions ensure that the lubrication damping is directly coupled to load, speed and film conditions.

6.4 Geometrical Imperfections and Waviness

Geometrical imperfections on the contacting bodies represent one of the most critical excitation sources in rolling bearings. The waviness on the inner ring, outer ring and rolling elements is shown in Figure 6.1

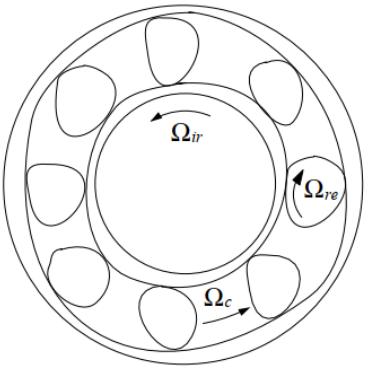


Figure 6.1: Waviness excitation in ball bearings

and represented by a truncated Fourier series:

$$W(\theta) = \sum_{n=1}^{N} A_n \cos(n\theta + \phi_n),$$

with amplitudes A_n decaying approximately with the square of the wavenumber for the low and medium orders. The waviness produces time-varying normal contact forces as the rolling elements over-roll the periodic deviations. The frequency of these fluctuations depends on the rotational speeds of inner ring, cage and rolling elements and on the specific wavenumber.

The contribution of rolling-element waviness can be particularly important due to their high rotational speed, even when the amplitude is significantly smaller than that of the rings.

6.4.1 High-Order Waviness

Higher wavenumbers, including those equal to the number of balls plus or minus one, can induce rigid-body vibration modes of the outer ring and may result in significant excitation amplitudes. These modes are especially relevant for bearings with a large number of rolling elements.

6.5 Component Mode Synthesis for Bearings

6.5.1 Limitations of Classical CMS

Classical CMS techniques rely on fixed-interface normal modes and static constraint modes, assuming the location of interface forces is fixed. In a rolling bearing, however, the contact forces rotate continuously, so their application point moves along the raceway. Interpolating nodal displacements at moving locations introduces discretisation errors and artificial dynamics.

6.5.2 SKF Analytical CMS Method

To circumvent this difficulty, SKF uses an analytical representation of the raceway deformation based on global orthogonal functions. The circumferential dependence is captured through a Fourier series, while the radial and axial variations are represented using Chebyshev polynomials.

Let the deformation of the raceway in the radial direction be expressed as:

$$u_r(r, z, \theta, t) = \sum_{n,m,l} a_{nml}(t)\, \cos(n\theta)\, T_m\left(\frac{z}{Z_0}\right) T_l\left(\frac{r}{R_0}\right),$$

where T_m denotes a Chebyshev polynomial of order m and Z_0 and R_0 are normalisation constants.

Each term of this analytical expansion defines a global constraint mode in the CMS sense. The full deformation of the housing with the outer ring is therefore represented by a combination of analytical global modes and fixed-interface normal modes computed via finite element analysis.

This approach provides a reduced model that retains accuracy under moving contact loads, preserves continuity and avoids the need for node-based interpolation.

6.6 Matrix Formulation of Component Mode Synthesis

The Component Mode Synthesis reduction used in the SKF dynamic model relies on the idea that the displacement field of each flexible component can be represented as a superposition of a small number of characteristic deformation patterns. These include static constraint modes, which reproduce the deformation under static interface loads, and fixed–interface normal modes, which reproduce the dynamic flexibility of the structure within the frequency range of interest. The resulting mathematical structure allows the full finite element equations of each component to be projected onto a reduced space of analytically or numerically defined basis functions.

Let $\mathbf{x}$ be the vector collecting all finite element degrees of freedom of a given component. The Ritz approximation writes the displacement field as

$$\mathbf{x} = \boldsymbol{\Phi}\,\mathbf{p},$$

where $\boldsymbol{\Phi}$ is the component mode matrix and $\mathbf{p}$ the vector of generalised coordinates. The matrix $\boldsymbol{\Phi}$ contains the static constraint modes and the fixed–interface normal modes, arranged column-wise and normalised so as to guarantee independence and numerical stability.

Substituting this representation into the finite element equations of motion

$$\mathbf{M}\,\ddot{\mathbf{x}} + \mathbf{C}\,\dot{\mathbf{x}} + \mathbf{K}\,\mathbf{x} = \mathbf{f},$$

and premultiplying by $\boldsymbol{\Phi}^T$ yields the reduced system

$$\mathbf{m}\,\ddot{\mathbf{p}} + \mathbf{c}\,\dot{\mathbf{p}} + \mathbf{k}\,\mathbf{p} = \mathbf{f}_r,$$

where the reduced matrices are defined as

$$\mathbf{m} = \boldsymbol{\Phi}^T\mathbf{M}\boldsymbol{\Phi}, \qquad \mathbf{c} = \boldsymbol{\Phi}^T\mathbf{C}\boldsymbol{\Phi}, \qquad \mathbf{k} = \boldsymbol{\Phi}^T\mathbf{K}\boldsymbol{\Phi},$$

and the reduced force vector as

$$\mathbf{f}_r = \boldsymbol{\Phi}^T\mathbf{f}.$$

In the SKF analytical CMS method, the matrix $\boldsymbol{\Phi}$ consists of two blocks. The first block contains global static modes associated with analytical functions describing the radial and axial deformation of the raceway through combinations of Fourier terms in the circumferential direction and Chebyshev polynomials in the radial and axial directions. The second block contains fixed–interface normal modes computed from the finite element model by constraining the raceway degrees of freedom in the directions normal to the contact.

Because the analytical global modes explicitly encode the circumferential dependence of the deformation, the transformation $\mathbf{x} = \mathbf{\Phi p}$ remains valid at any angular position of the rolling element. This allows the reduced matrices $\mathbf{m}$, $\mathbf{c}$ and $\mathbf{k}$ to faithfully represent the response of the outer ring and the housing under moving contact loads, avoiding the discontinuities and discretisation errors that arise from nodal interpolation.

When multiple components are coupled together, such as the shaft, housings and rolling elements, their reduced equations are assembled into a global reduced system by enforcing interface compatibility conditions through constraint equations. The resulting global model preserves the essential dynamical features of the full finite element model while dramatically reducing computational effort, enabling efficient time-domain simulation of the complete bearing application.

6.7 Schematic Representation of the CMS Method

To clarify the structure of the Component Mode Synthesis reduction employed in the bearing model, two schematic representations are presented. The first shows how the full finite element domain is decomposed into retained static and dynamic modes. The second illustrates the moving contact load travelling along the raceway and the analytical basis functions used to represent its deformation.

6.7.1 Mode Decomposition in CMS

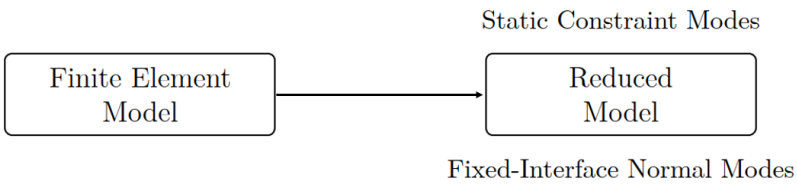


Figure 6.2: Decomposition of the finite element model into a reduced set of CMS component modes

6.7.2 Moving Contact Loads and Analytical Shape Functions

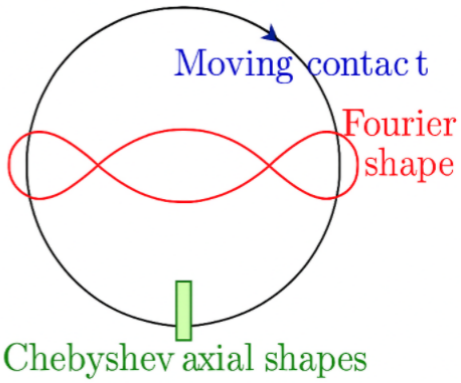


Figure 6.3: Representation of moving contact loads and analytical basis functions used in the SKF CMS method

6.8 Local Defects and Indentations

Local defects such as indentations, pits or "Brinell-like" marks are treated as localised deviations from the ideal geometry. Their shape is incorporated directly into the mutual approach, modifying the contact force according to:

$$\delta_{\text{eff}}(t) = \delta(t) - W_{\text{defect}}(\theta(t)),$$

where W_{defect} is a localised geometric function defined along the raceway.

As the rolling elements traverse the defect, a sharp fluctuation in the contact force arises, which excites resonances of both the outer ring and the surrounding structure. The defect response is particularly strong in the axial modes of the outer ring due to their efficient acoustic radiation.

6.9 Hybrid Bearings and Large Ball Sets

In hybrid bearings equipped with ceramic balls, the reduced density and increased stiffness of the rolling elements modify the dynamic response. The natural frequencies of rolling-element modes increase significantly, and the coupling between waviness and ball passing frequency changes due to the different inertia and compliance properties. Bearings with a large number of rolling elements present more complex load distributions and generate more intricate excitation patterns, especially for waviness orders close to the ball count. These qualitative considerations

are also consistent with internal SKF analyses, including Berrada [8], which highlights the relevance of waviness orders equal to the number of rolling elements ± 1 in bearings with large ball sets. The CMS formulation is naturally suited to such configurations, because the analytical basis functions readily represent the resulting deformation patterns.

6.10 Linearisation, Modal Analysis and Transient Simulation

Before transient integration, the system is linearised around its quasi-static equilibrium. The linearised stiffness matrix includes Hertzian or EHL stiffness contributions, geometric stiffness due to contact-angle sensitivity and structural stiffness of the components.

Solving the undamped eigenvalue problem yields natural frequencies and mode shapes for all relevant deformation patterns. These modes guide the interpretation of the response and allow for efficient post-processing.

The transient simulation is performed using a Newmark-type integration method with Newton–Raphson iterations to handle nonlinear contact forces. The computed time histories provide detailed information on vibration levels, contact force fluctuations, resonance excitations and defect responses, making it possible to analyse both steady-state and transient operating conditions.

6.11 Conclusion

The theoretical foundation of the SKF dynamic bearing model combines nonlinear contact mechanics, elastohydrodynamic lubrication theory, harmonic representations of imperfections and a specialised CMS reduction scheme capable of representing moving contact loads. This unified formulation enables the accurate prediction of bearing vibration, dynamic load distribution, resonance behaviour and defect response within complete mechanical systems.

Chapter 7

Results of the numerical modal analysis

This chapter presents the numerical results obtained through a structured sequence of modal analyses performed on the spindle assembly and its individual components. The methodological logic mirrors the experimental investigation, ensuring full coherence between the two approaches. As in the experimental workflow, the analysis proceeded progressively: starting with the numerical modal evaluation of each component considered as an isolated system, then extending to the rotating subassemblies, and ultimately assessing the complete spindle assembly as a single integrated structure. This hierarchical organization enables a direct, component-wise comparison between experimental and numerical outcomes and facilitates the identification of potential discrepancies and their origins. Although the conceptual framework is analogous to that of the experimental campaign, the execution of the numerical analyses required a dedicated sequence of modelling operations specific to the SKF SimPro Expert environment. For each component or assembly, the numerical modal analysis followed a standardized workflow composed of the following steps:

1. Creation of the CAD model of the component or assembly, export in .iges format, conversion into STEP format, and import into SKF SimPro Expert, where the geometric volume is automatically computed.

2. Addition of material properties, specifically density and elastic stiffness, required for an accurate modal characterization.

3. Verification of mass consistency by comparing the mass measured experimentally with the numerical mass computed as the product of material density and geometric volume; if the two values do not coincide, the model must be refined until the condition is satisfied.

4. Generation of the three-dimensional finite element mesh, with element size and type chosen according to the geometric complexity and expected dynamic behaviour.

5. Removal of all constraints to reproduce the free–free boundary condition used in the experimental setup.

6. Execution of the numerical modal analysis within SKF SimPro Expert.

In addition to the general workflow described above, the material properties (Table 7.1) used for each component were defined with particular care, as they directly affect both mass consistency and the stiffness distribution of the numerical model. The density and elastic modulus for each part were assigned according to the available datasheets or, when such information was not accessible, through a reverse-engineering process.

Material Properties			
Material	**Density [kg/m^3]**	**Elastic modulus [GPa]**	**Poisson ratio**
Aluminum	2770	72	0,33
Steel	7800	210	0,3
Bearing Steel	7800	206	0,3

Table 7.1: Material properties

While this sequence represents the set of operations common to all models, additional adjustments were introduced for specific components to better reproduce their real mechanical behaviour. These refinements, although not identical across all configurations, were essential to ensure that the numerical predictions remained as faithful as possible to the physical system. Finally, numerical Campbell analyses were performed for the rotating configuration of the spindle to complement the experimental Campbell diagram presented in the previous chapter. The results reported in this section include the natural frequencies and associated mode shapes for all investigated configurations, forming the basis for the comparative assessment with the experimental findings developed in the following chapter.

7.1 Shaft

In SKF SimPro Expert, two modeling approaches are available for simulating the dynamic behaviour of the shaft:

- **Fourier shaft**: The Fourier-based shaft is constructed using a fundamentally different approach. The procedure begins with the definition of a two-dimensional component that is discretised into a 2D finite-element mesh (Figure 7.1).

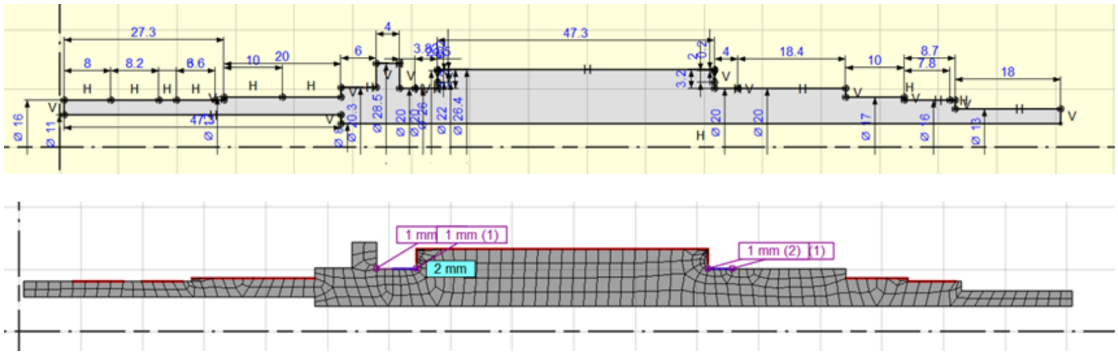


Figure 7.1: 2D Fourier components

This mesh is subsequently revolved and sliced around the rotational axis, producing a full three-dimensional representation of the shaft with its real geometry (Figure 7.2).

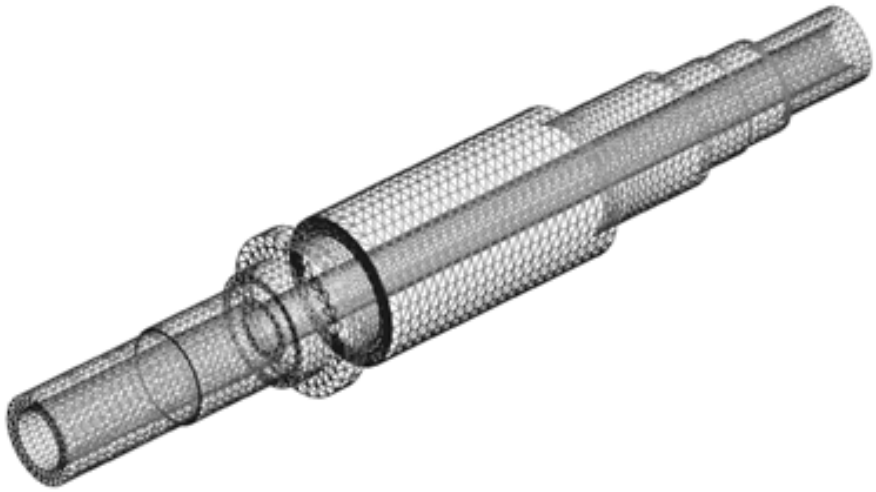


Figure 7.2: Fourier shaft: 3D mesh

Unlike the beam formulation, presented in the next section, this model is capable of representing all deformation components, including radial expansion,

and it naturally accounts for local variations in stiffness and mass distribution. Interfaces are automatically generated on the 3D mesh (Figure 7.3) so that the shaft can be connected to adjoining components, for instance to the inner rings of the bearings.

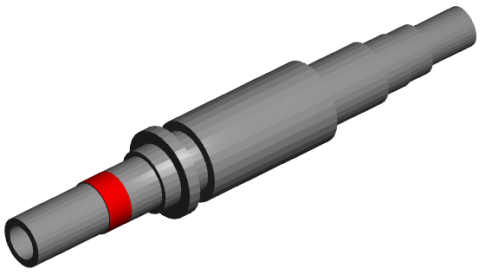


Figure 7.3: Fourier shaft: interfaces and connections

The deformation behaviour at the coupling interfaces is governed by analytical shape functions: a Fourier series describes the circumferential dependence, while Chebyshev polynomials represent the transverse components of the deformation field. This formulation makes it possible to reproduce three-dimensional deformation patterns with significantly higher fidelity than the beam-based approach while keeping computation times manageable. By modelling the component directly in 3D, the real geometry is captured more faithfully, allowing the shaft to elongate, twist, and expand radially. The rotor bars of the shaft are represented as a thin cylindrical sleeve made of aluminum - light blue region in Figure 7.4 - that surrounds the steel shaft, while the breaker bars at the extremities of this sleeve are modelled as two aluminum rings - dark blue region in Figure 7.4 -.



Figure 7.4: Fourier shaft model

This approach makes it possible to account for both the mass and the stiffness contributions of the aluminum components integrated into the steel structure.

- **Beam shaft**: In SKF SimPro Expert, the standard shaft modeler allows the user to construct the shaft directly in a two-dimensional view, where the geometry is divided into multiple segments of different diameters. This 2D representation is then discretised into beam elements that are connected at nodal points along the shaft axis. Although the model is displayed as a three-dimensional body, its mathematical nature remains that of a one-dimensional beam governed by classical beam theory. As a consequence, the shaft is able to elongate axially and to twist, but it cannot undergo radial expansion or contraction, since no real 3D geometry is associated with the beam formulation. This simplification significantly reduces computational cost and makes the beam model suitable for rapid evaluations, although it inherently limits the accuracy when radial deformation effects are important. The straightforward construction of the model, combined with its relatively low computational cost, makes this approach widely used in industrial applications. In this simplified configuration (Figure 7.5), the two aluminum rings are replaced by a lumped mass applied to the aluminum sleeve surrounding the steel shaft.



Figure 7.5: Beam shaft model

This represents a significant simplification, as introducing a lumped mass implies that the stiffness contribution of these rings is neglected.

Based on these considerations, all assemblies containing the shaft were modeled according to both of these paradigms.

7.1.1 Beam shaft

According to the beam shaft model, the modal parameters are reported in Table 7.2

Modal Parameters	
Shape Name	**Frequency [Hz]**
Mode shape 1	5013
Mode shape 2	9137

Table 7.2: Modal parameters of the beam shaft

7.1.2 Fourier shaft

According to the Fourier shaft model, the modal parameters are reported in Table 7.3

Modal Parameters	
Shape Name	**Frequency [Hz]**
Mode shape 1	4801
Mode shape 2	8762

Table 7.3: Modal parameters of the Fourier shaft

7.2 Shaft accessories

Regarding the modeling of the auxiliary components, no special measures were required during the construction of their numerical models, as these parts are simple axisymmetric elements and they are purely FEM elements. Consequently, all the steps outlined at the beginning of the chapter were followed without the need for additional considerations. Figure 7.6 shows how the bezel is modeled in SKF SimPro Expert.



Figure 7.6: Bezel: model and mesh

and the modal parameters are reported in Table 7.4:

Modal Parameters	
Shape Name	**Frequency [Hz]**
Mode shape 1	11820
Mode shape 2	12663
Mode shape 3	27167

Table 7.4: Modal parameters of the bezel

Figure 7.7 shows how the bezel is modeled in SKF SimPro Expert.



Figure 7.7: Bushing: model and mesh

and the modal parameters are reported in Table 7.5:

Modal Parameters	
Shape Name	**Frequency [Hz]**
Mode shape 1	Not detected
Mode shape 2	26794
Mode shape 3	36539

Table 7.5: Modal parameters of the bushing

Figure 7.8 shows how the bezel is modeled in SKF SimPro Expert

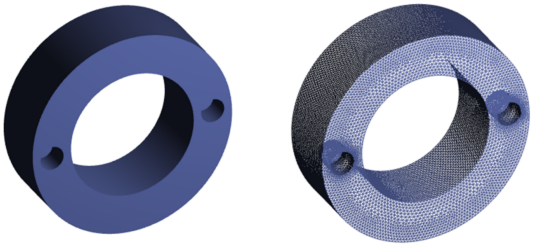


Figure 7.8: Ring: model and mesh

and the modal parameters are reported in Table 7.6:

Modal Parameters	
Shape Name	**Frequency [Hz]**
Mode shape 1	27435

Table 7.6: Modal parameters of the ring

7.3 Rotating components

The software employed for the numerical modal analysis is not capable of simulating vibrational modes in the axial direction, since in that direction the shaft stiffness is so high as to generate vibration modes that lie far outside the frequency range of interest ($0 < f < 10$ kHz) under the free-free boundary condition required by the modal analysis. Consequently, the analysis is limited to the evaluation of purely radial vibration modes. Nevertheless, despite this limitation, several simulations were carried out under different validity assumptions. Specifically, the following configurations were considered:

- beam shaft model
- Fourier shaft model
- Fourier shaft model including the connection of the side surfaces of the bearing inner rings because they do not penetrate each other

Each of these configurations yielded distinct results.

7.3.1 Beam shaft

In SKF SimPro Expert, the beam shaft model of the rotating components looks like Figure 7.9

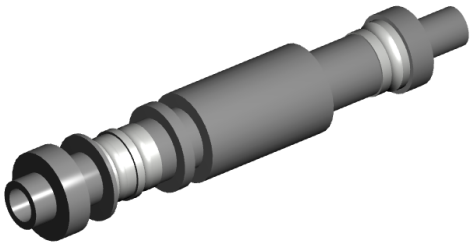


Figure 7.9: Shaft and accessories: beam shaft model

and, according to this model, the modal parameters, reported in Table 7.7, are

Modal Parameters	
Shape Name	**Frequency [Hz]**
Mode shape 1	3912
Mode shape 2	8074
Mode shape 3	8499

Table 7.7: Modal parameters of the shaft and rotating components - beam model

7.3.2 Fourier shaft

In SKF SimPro Expert, the beam shaft model of the rotating components looks like Figure 7.10

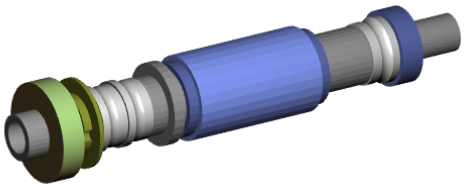


Figure 7.10: Shaft and accessories: Fourier shaft model

and, according to this model, the modal parameters, reported in Table 7.8, are

Modal Parameters	
Shape Name	**Frequency [Hz]**
Mode shape 1	3782
Mode shape 2 [1]	7777
Mode shape 3	7877

Table 7.8: Modal parameters of the shaft and rotating components - Fourier model

7.3.3 Fourier shaft with connection on the side surfaces of bearings inner rings

In SKF SimPro Expert, the Fourier shaft model of the rotating components looks like Figure 7.10, the connection on the side surfaces of bearing inner rings is not visible but is implemented on the software. The purpose of the implemented connection is to prevent the lateral faces of the bearings from interpenetrating, as this does not occur under real operating conditions. According to this model, the modal parameters, reported in Table 7.9 are:

Modal Parameters	
Shape Name	**Frequency [Hz]**
Mode shape 1	3782
Mode shape 2	7877

Table 7.9: Modal parameters of the shaft and rotating components - Fourier model with connection

Despite the fact that this model, due to the connection between the lateral surfaces of the inner rings, introduces an additional degree of detail, the difference in the resulting natural frequency values is not significant (Table 7.7 & 7.8). Therefore, since adding detail increases the model complexity and computational cost, this implementation will not be retained in the subsequent steps, and the basic Fourier shaft configuration is preserved. This represents a clear limitation of the software, which is unable to adequately simulate the non-penetration condition between two rigid bodies.

7.4 Casing

Although it is not strictly a shaft, the casing was modeled (Figure 7.11) — albeit in an approximate manner—using the same approach.

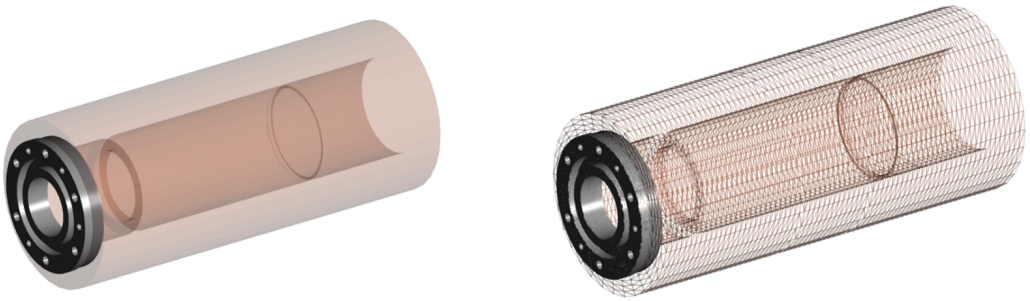


Figure 7.11: Casing: model and mesh

The modeling procedure is fundamentally incorrect from the outset, as the software allows the creation of components with homogeneous density only. In our case, the presence of the stator bars in the central region makes the component strongly non-homogeneous. In addition to this limitation, both the geometric and material modeling are necessarily approximate, since the original manufacturer's datasheet was not available and the component had to be reconstructed through a reverse-engineering process.
According to these hypotheses, the modal parameters, reported in Table 7.10, are:

Modal Parameters	
Shape Name	**Frequency [Hz]**
Mode shape 1	12486
Mode shape 2	14081
Mode shape 3	18123

Table 7.10: Modal parameters of the casing

7.5 Spindle assembly

The modeling of the assembly includes all rotating and non-rotating components mounted on the shaft, and this sub-assembly is enclosed within the casing.
The following describes how each of these components is mounted on the shaft:

- the bushing, bezel, and ring have their bore surfaces connected to the shaft;

- for the bearings, the inner ring is fixed to the shaft, while the outer ring is fixed to the corresponding housing;

- the two bearings on the DE side are axially connected to the shaft through the outer ring,

- the bearing on the NDE side has an outer ring that is free to move in the axial direction; this configuration can be justified by considering that the preload generated by the springs acts axially from the NDE side toward the DE side;

- the spring is not mounted directly on the shaft but is housed in a dedicated cavity within the casing;

- all these components are enclosed within a casing which, unlike each component considered individually, is modeled according to both the beam-shaft paradigm and the Fourier-shaft paradigm by means of a series of Fourier disks;

- the flange is secured by means of very small bolts fitted into a narrow groove of the casing

In SKF SimPro Expert, the Fourier shaft model of the rotating components looks like Figure 7.12.

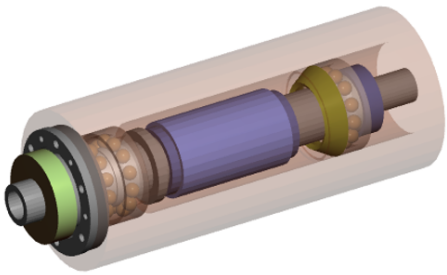


Figure 7.12: Spindle assembly: Fourier shaft model

According to this model, the modal parameters, reported in Table 7.11 are:

Modal Parameters	
Shape Name	**Frequency [Hz]**
Mode shape 1	1553
Mode shape 2	2835
Mode shape 3	4149
Mode shape 4	5165
Mode shape 5	7777
Mode shape 6	8453

Table 7.11: Modal parameters of the spindle assembly - Fourier shaft

7.6 Spindle in rotation

The operating conditions for the rotating spindle are the same as in the experimental case, namely:

- a run-up from 0 to 10 kHz in 90 s,
- a steady-state condition at a constant speed of 10 kHz for 40 s,
- a coast-down to zero speed by disconnecting the electrical supply.

7.6.1 Beam shaft

To simulate the system according to the beam-shaft model, the casing is divided into three disks (Figure 7.13 & 7.14 for the mesh and 2D model). This configuration prevents the spindle from being supported on the V-block (the one used in the experiments), and therefore the disc housings are grounded directly.

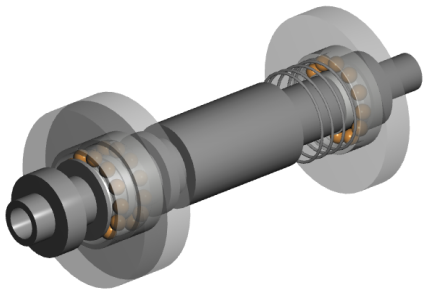


Figure 7.13: Fourier discs for the spindle in operation - beam shaft

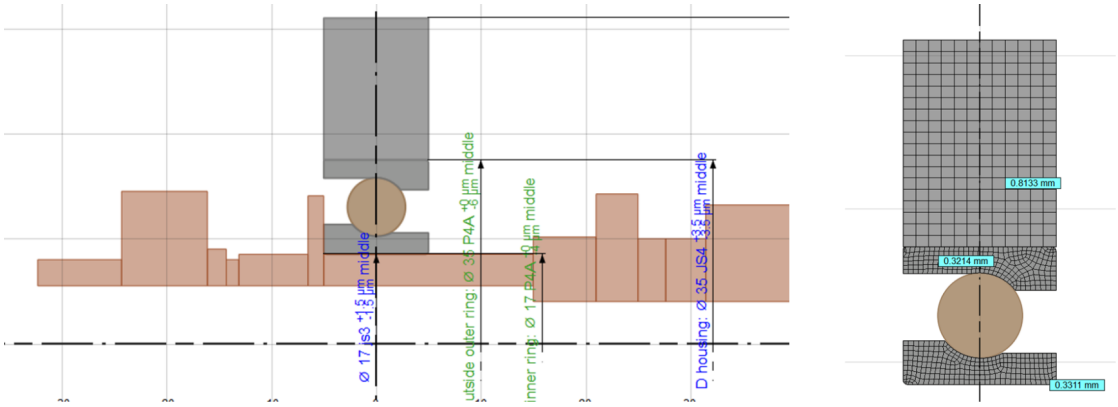


Figure 7.14: Fourier discs: model and meshing

Campbell diagram

Figure 7.15 shows the Numerical Campbell diagram for the spindle assembly according to the beam shaft paradigm.

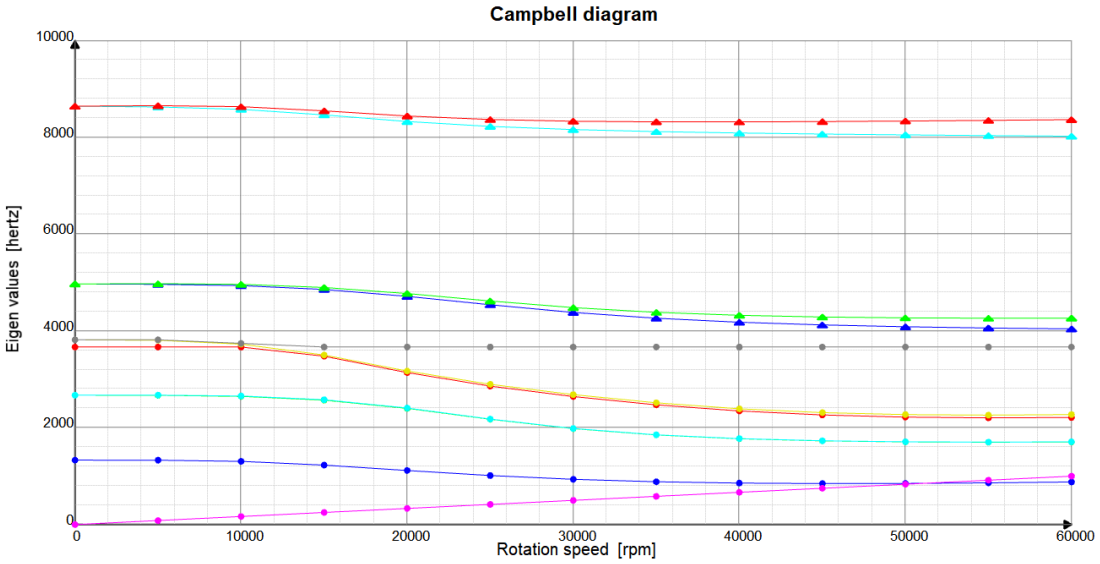


Figure 7.15: Numerical Campbell diagram for the undamped model - beam shaft

Operating deflection shapes

The operating deflection frequencies, according to the beam model, are reported in Table 7.12

Shape Parameters	
Shape Name	**Frequency [Hz]**
Shape 1	1331
Shape 2	2673
Shape 3	3669
Shape 4	3818
Shape 5	4973
Shape 6	8646

Table 7.12: Operating deflection shapes - beam shaft model

7.6.2 Fourier shaft

To reproduce the operating conditions required for the spindle to rotate, a V-shaped steel support was introduced (Figure 7.16), with its base constrained to the ground in the simulations.

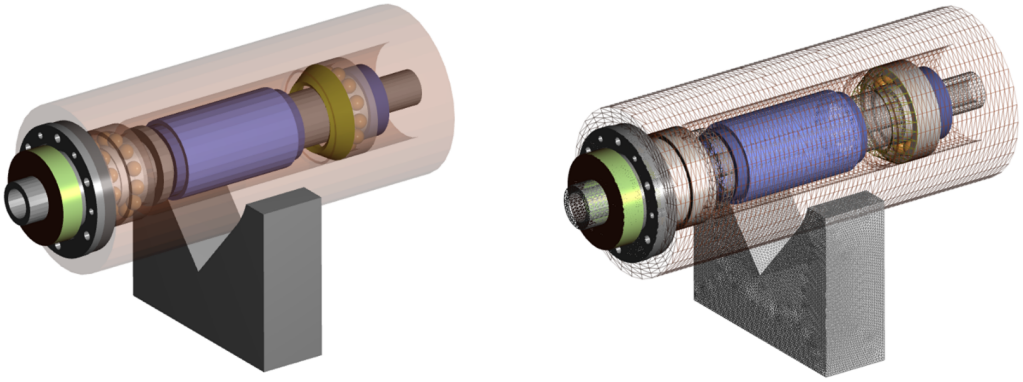


Figure 7.16: Spindle in rotation: Fourier model and mesh

The Campbell diagram, which illustrates the evolution of natural frequencies as a function of the rotational speed, was obtained in a discrete manner by performing a sequence of modal analyses at different rotational speeds. Based on these results, the corresponding Operating Deflection Shapes (ODSs) were subsequently determined. Due to the inherent limitations of the beam-shaft model, only the Fourier-shaft formulation was considered for this analysis.

Campbell diagram

Figure 7.17 shows the Numerical Campbell diagram for the spindle assembly.

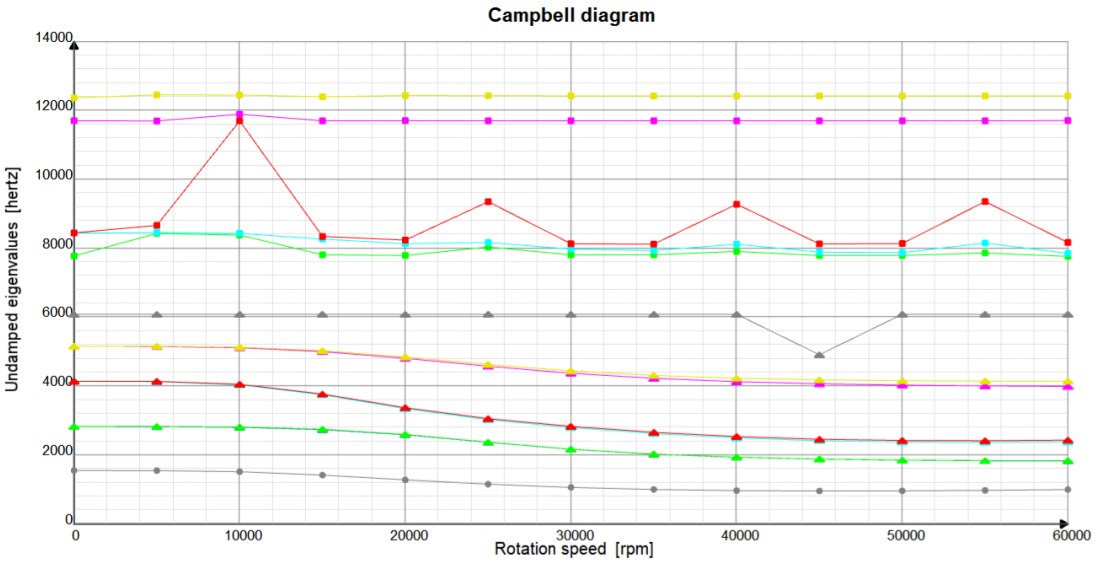


Figure 7.17: Numerical Campbell diagram for the undamped model - Fourier shaft

Operating deflection shapes

The operating deflection frequencies, according to the Fourier shaft model, are reported in Table 7.13

Shape Parameters	
Shape Name	**Frequency [Hz]**
Shape 1	1553
Shape 2	2832
Shape 3	4142
Shape 4	5159
Shape 5	6088
Shape 6	8447

Table 7.13: Operating deflection shapes - Fourier shaft model

Chapter 8

Comparison between experiments and numerical model

8.1 Introduction

The comparison between experimental and numerical results represents a central step in assessing the reliability, predictive capability and physical consistency of the dynamic model implemented in SKF SimPro. The objective of this chapter is not limited to verifying whether the numerical eigenfrequencies correspond to the experimentally identified ones; it also aims to understand the origin, magnitude and direction of the deviations, to interpret the underlying physical mechanisms, and to establish to what extent the model can support future design decisions, calibration activities or methodological developments. The analysis follows the same hierarchical progression adopted during the experimental campaign, beginning with individual components considered in free–free conditions, continuing with rotating subassemblies and concluding with the complete spindle, both in stationary conditions and under operational rotation. The use of a unified dataset, combining the experimental modal parameters extracted in Chapter 5 with the corresponding numerical results reported in Chapter 7 and consolidated in the comparison tables, allows each mode to be examined cohesively and consistently. The deviations are expressed as relative percentage differences with sign, a convention that makes it immediately clear whether the numerical model overestimates or underestimates the measured stiffness. A positive deviation indicates a stiffer numerical behaviour leading to higher natural frequencies, whereas a negative deviation reveals a more compliant numerical model or, alternatively, experimental conditions producing

additional stiffening that is not captured numerically. This approach offers several advantages. It allows the correlation quality to be evaluated not only in terms of absolute frequency alignment but also in terms of trend fidelity, modal ordering and sensitivity to boundary conditions. It also highlights critical aspects of the modelling assumptions, such as the treatment of bearing–housing interfaces, the representation of the casing, the simplifications embedded in the beam formulation, or the inability of the numerical tool to capture certain axial deformation mechanisms. Furthermore, by providing a consistent measure of deviation across all components and configurations, the analysis makes it possible to identify recurring patterns, such as the systematic overprediction of radial modes at low order or the degradation of accuracy in the higher-frequency range where local effects, contact nonlinearities and geometric complexities become increasingly important. The comparison carried out in this chapter therefore serves a dual purpose. On one hand, it validates the modelling strategy adopted in this study by quantifying its level of agreement with experimental evidence across all relevant frequency bands. On the other hand, it exposes the intrinsic limitations of the current implementation, which will form the basis for the proposed improvements discussed in the following chapter. Within this framework, the next sections examine each subsystem in detail, beginning with the shaft and accessory components, and progressing toward the full spindle assembly in both stationary and rotating conditions.

8.2 Shaft

Table 8.1 presents a comparison between the different configurations under investigation.

Shaft Modal Parameters						
Shape name	**Experimental frequency [Hz]**	**Numerical frequency beam shaft [Hz]**	**Numerical frequency Fourier shaft [Hz]**	**Experimental damping - ξ - [%]**	**Variation - Δf - beam [%]**	**Variation - Δf - Fourier [%]**
Mode shape 1	4426	5013	4801	1.044	-13.26	-8.47
Mode shape 2	8679	9137	8762	0.941	-5.28	-0.96

Table 8.1: Experimental and numerical modal parameters of the shaft

The shaft constitutes the most elementary benchmark for correlation because its boundary conditions can be reproduced closely in both test and simulation, and because its dynamics are governed primarily by geometry, mass distribution and bending stiffness. Under free–free support, the experimental campaign identified two dominant bending modes at approximately 4.43 (Figure 8.1) kHz and 8.68 kHz (Figure 8.2), with low modal damping on the order of one percent, which is typical for lightly damped metallic structures measured with impact testing in free–free conditions.

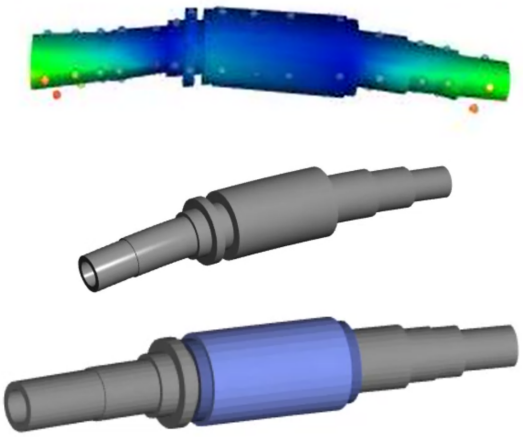


Figure 8.1: Shaft: mode shape 1 comparison

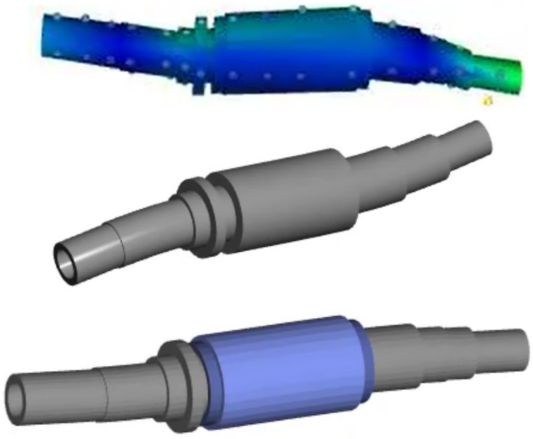


Figure 8.2: Shaft: mode shape 2 comparison

These results establish the reference against which the two numerical shaft formulations—beam and Fourier—are evaluated. When the shaft is modeled using the beam formulation, the first bending mode is overestimated by about thirteen percent and the second by roughly five percent relative to the experimental values. The corresponding frequencies are approximately 5.01 kHz and 9.14 kHz, respectively. This bias is consistent with the simplifying assumptions of a one-dimensional beam representation, which cannot reproduce radial expansion and tends to concentrate stiffness along the centreline; as a result, the effective bending compliance is slightly underestimated, yielding higher natural frequencies. In practical terms,

the beam model already delivers a correlation that would be acceptable for preliminary design screens, but it exhibits a systematic "too-stiff" tendency on the first family that should be acknowledged when drawing design inferences. Adopting the Fourier-based formulation improves the agreement decisively. The first bending mode is reduced to an overprediction of about eight percent, while the second is essentially matched within one percent. The numerical frequencies are approximately 4.80 kHz and 8.76 kHz, which indicates that adding circumferential Fourier components and through-thickness Chebyshev terms restores part of the three-dimensional compliance that is absent in the beam idealisation. In the present case, the Fourier model also accounts for the aluminium rotor sleeve and end rings as distributed 3-D features rather than as lumped masses, which further refines the inertia and stiffness distribution along the shaft. The net effect is a closer reproduction of the experimental trend and a marked reduction of the stiffness bias that characterises the beam alternative. From a damping standpoint, the experimental modal damping ratios of roughly one percent confirm that the shaft behaves as a lightly damped elastic member, and they also explain why frequency matching is the dominant criterion for correlation at component level. The numerical workflow does not introduce explicit structural damping in the undamped eigenvalue solution, so the comparison is naturally performed on modal frequencies rather than on decay parameters. Under this premise, the Fourier formulation can be considered validated for the frequency band of interest, whereas the beam model remains a useful but conservative surrogate.

8.3 Shaft accessories

The accessory components mounted on the shaft—the bezel, the bushing and the ring—represent an intermediate level of validation between the isolated shaft and the more complex rotating sets. Although these components do not dominate the global dynamic behaviour of the spindle, they contribute non-negligible local mass and stiffness effects and therefore must be evaluated individually to ensure that their modeling assumptions do not propagate systematic errors into the higher-level assemblies. The experimental results for these parts were obtained under free–free conditions through impact testing, following the same methodology adopted for the shaft, while the numerical results come from the dedicated finite element models presented in Chapter 7. Table 8.2 presents a comparison between the experimental and numerical results.

Ring Modal Parameters				
Shape name	**Experimental frequency [Hz]**	**Numerical frequency [Hz]**	**Experimental damping - ξ - [%]**	**Δf %**
Mode shape 1	27318	27435	1.819	-0.43

Table 8.2: Experimental and numerical modal parameters of the ring

Among the three elements, the ring displays the most accurate correlation. Its first significant experimental mode appears at approximately 27.32 kHz (Figure 8.3), and the numerical prediction differs by less than half a percent.

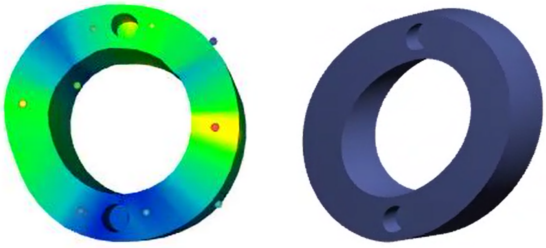


Figure 8.3: Ring - mode shape 1: comparison

This exceptionally small deviation is consistent with the ring's simple geometry and the nearly axisymmetric nature of its deformation, which the numerical model reproduces straightforwardly. The agreement confirms that the material assumptions and mesh density used for this component are adequate, and that modelling uncertainties are minimal. The ring therefore does not introduce any appreciable source of error in the subsequent assembly stages. Table 8.3 presents a comparison between the experimental and numerical results.

Bushing Modal Parameters				
Shape name	**Experimental frequency [Hz]**	**Numerical frequency [Hz]**	**Experimental damping - ξ - [%]**	**Δf %**
Mode shape 1	28670	26794	1.819	6.54

Table 8.3: Experimental and numerical modal parameters of the bushing

The bushing exhibits a more pronounced discrepancy between experimental and numerical results compared to the other components. Experimentally, its first significant mode appears at approximately 28.67 kHz (Figure 8.4, with a measured modal damping of about 1.8%. The numerical model predicts the corresponding

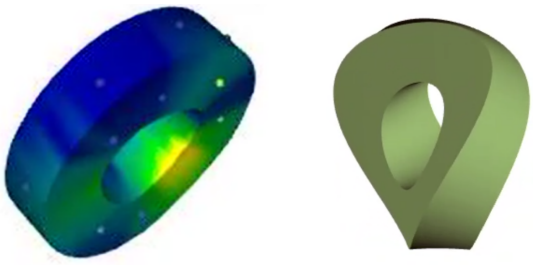


Figure 8.4: Bushing - mode shape 1: comparison

mode at 26.79 kHz, resulting in a relative deviation of about 6.54%, indicating that the numerical model underestimates the effective stiffness of the component.

This difference suggests the presence of stiffness contributions in the experimental configuration that are not fully captured in the numerical model. These may be associated with local contact effects, assembly-induced constraints, or residual boundary stiffness, all of which tend to increase the natural frequencies. In addition, the geometric complexity of the bushing, characterised by thickness variations and internal features, may further contribute to modelling inaccuracies if not fully resolved.

Overall, while the numerical model captures the general dynamic behaviour of the component, the observed discrepancy highlights the sensitivity of the bushing to local stiffness effects and modeling assumptions. Table 8.4 presents a comparison between the experimental and numerical results.

Bezel Modal Parameters				
Shape name	**Experimental frequency [Hz]**	**Numerical frequency [Hz]**	**Experimental damping - ξ - [%]**	**Δf %**
Mode shape 1	27318	27435	1.819	- 0.43

Table 8.4: Experimental and numerical modal parameters of the bezel

The bezel shows a very good agreement between experimental and numerical results (Figure 8.5, with a frequency deviation below 1%. The first significant mode is accurately predicted, indicating that the numerical model effectively represents the stiffness and mass distribution of the component.

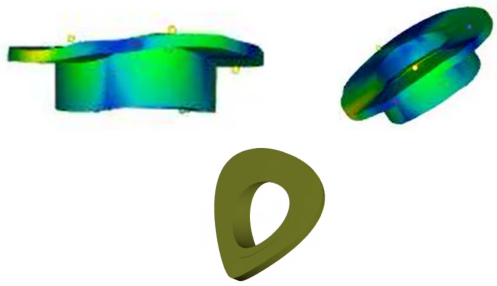


Figure 8.5: Bezel - mode shape 1: comparison

The small discrepancy suggests that boundary condition effects and modelling simplifications have a limited influence on this mode. Therefore, the bezel can be considered well represented within the current modeling framework.
The comparison between experimental and numerical modal results provides insight into both the accuracy of the finite element model and the influence of boundary conditions and modeling assumptions on the dynamic response.
For the ring and bezel components, the first natural frequency is predicted with very good agreement, with discrepancies below 1%. This level of correlation suggests that the numerical model accurately captures the mass and stiffness distribution of these components. In addition, it indicates that, for these geometries and mode shapes, the influence of boundary conditions is limited, and the assumption of ideal free–free conditions does not introduce significant errors in the predicted response.
Conversely, the bushing component exhibits a noticeably larger discrepancy, with the experimental natural frequency exceeding the numerical prediction by approximately 6.5%. From a structural dynamics standpoint, this difference can be interpreted as an indication of higher effective stiffness in the experimental system. In fact, natural frequencies are directly related to the square root of the stiffness-to-mass ratio, according to classical vibration theory. Therefore, even relatively small unmodeled stiffness contributions can lead to appreciable frequency shifts.
The observed overestimation of stiffness in the experimental results is likely associated with effects that are not fully represented in the numerical model. These may include local contact stiffness, interference fits, assembly-induced constraints, or residual boundary stiffness introduced by the experimental setup. Although the test configuration aims to reproduce free–free conditions, practical implementations inevitably introduce small constraints, which tend to increase the global stiffness and shift the natural frequencies toward higher values.
Overall, the results confirm the robustness of the numerical model for components with relatively simple dynamic behavior, while highlighting the sensitivity of more complex or interface-dominated components, such as the bushing, to secondary

effects and modeling assumptions. This emphasizes the importance of accurately representing contact conditions and boundary effects when aiming for high-fidelity correlation between experimental and numerical modal analyses.

8.4 Rotating components

The rotating-components configuration represents the first meaningful escalation in system complexity, because it brings together the shaft and the auxiliary parts that rotate with it—namely the bezel, bushing and ring—into a single subassembly operating under free–free conditions. Although this configuration still excludes the bearings and the casing, it already introduces an important structural characteristic: the dynamic behaviour is no longer governed by the shaft alone but by the combined mass and stiffness distribution of several interconnected elements. This shift makes the correlation exercise more sensitive to modelling assumptions, particularly the accuracy of the shaft representation and the fidelity with which local contacts and interfaces are treated. The comparison relies on the experimental modal parameters identified in Chapter 5 and the numerical predictions calculated using both the beam and Fourier shaft formulations, as reported in Chapter 7. Table 8.5 presents a comparison between the different configurations under investigation.

Shaft and Accessories Modal Parameters						
Shape name	**Experimental frequency [Hz]**	**Numerical frequency beam [Hz]**	**Numerical frequency Fourier [Hz]**	**Experimental damping - ξ - [%]**	**Δf beam [%]**	**Δf Fourier [%]**
Mode shape 1	3687	3912	3782	1.613	-6.10	-2.5766
Mode shape 2	8310	8074	7877	1.741	2.84	5.2106
Mode shape 3 [1]	Not detected	8499	7777	Not detected	N/A	N/A

Table 8.5: Experimental and numerical modal parameters of the shaft and accessories

AGGIUNGI LE FORME MODALI NUMERICHE E SPERIMENTALI

Experimentally, two dominant radial modes were observed at approximately 3.69 (Figure 8.6) kHz and 8.31 kHz (Figure 8.7).

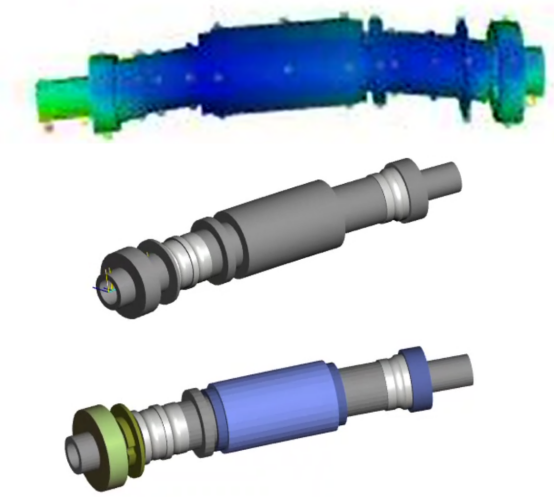


Figure 8.6: Shaft and accessories - mode 1: comparison

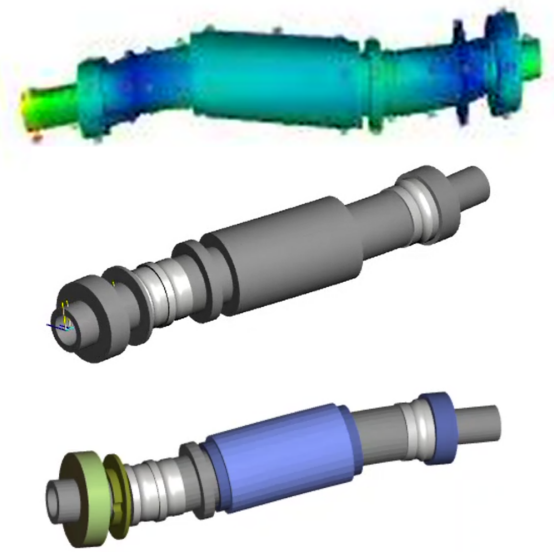


Figure 8.7: Shaft and accessories - mode 2: comparison

These modes reflect the global bending behaviour of the shaft–accessory ensemble, with the modal shapes indicating composite deformation patterns that include both shaft curvature and local accessory participation. When the numerical model is constructed using the beam-shaft formulation, the first mode is overestimated by roughly six percent, while the second is underestimated by about three percent. The predicted values, approximately 3.91 kHz and 8.07 kHz, indicate a moderate but consistent deviation that echoes the trends observed for the isolated

shaft. The beam model, with its inherently higher bending stiffness and simplified representation of the aluminium sleeve and end-rings, again tends to elevate the first mode and to shift the balance of stiffness contributions across the structure. Despite this, the correlation remains acceptable and preserves the correct ordering of the modes, which is essential for system-level interpretation. The Fourier-based formulation yields a clearer improvement. It overestimates the first radial mode by approximately three percent and underestimates the second by about six percent, corresponding to numerical predictions of around 3.78 kHz and 7.78 kHz. The closer alignment of the first mode, in particular, confirms that the Fourier representation better captures the distributed mass and stiffness of the rotating accessories and their interaction with the shaft. Because this formulation incorporates circumferential Fourier terms and through-thickness Chebyshev components, it reproduces subtle deformation mechanisms that the beam model necessarily overlooks. As a result, the Fourier model provides not only a more accurate frequency prediction but also a modal deformation pattern more consistent with experimental observations, particularly regarding the participation of the end-mounted accessories. A noteworthy limitation arises in the axial direction: the numerical tool, in this specific modelling configuration, is unable to compute axial vibration modes for the rotating-components subassembly. This constraint stems from the absence of axial stiffness elements in the simplified interface representation used at this stage. Consequently, experimental axial modes—identified in Chapter 5—cannot be directly compared to numerical predictions. Rather than indicating a mismatch, this highlights a structural limitation of the modelling framework that persists until bearings and boundary constraints are introduced in the spindle-assembly analyses. Although the lack of axial predictions reduces the completeness of the correlation for this subassembly, it does not compromise the interpretation of the radial behaviour, which is the dominant contribution in the frequency band of interest. Overall, the rotating-components configuration demonstrates a clear continuity with the trends observed at the individual-component level. The beam formulation yields a moderately stiff representation that remains usable but systematically deviates from experimental stiffness, whereas the Fourier formulation substantially improves the correlation, especially for the first radial mode, which is crucial for understanding how the shaft and accessories dynamically integrate. The absence of axial predictions at this stage is an intrinsic constraint rather than a modelling failure, and its implications will be revisited in the context of the full spindle assembly, where axial compliance and bearing interactions become available for numerical representation. The results confirm that the Fourier-based approach is the more reliable foundation for the subsequent assembly-level analyses.

8.5 Casing

The casing represents one of the most challenging components to correlate numerically, because its dynamic behaviour depends on a combination of complex geometry, large internal cavities, material non-uniformity and the presence of the motor's stator bars, all of which contribute to a stiffness distribution that is difficult to reproduce with simplified modelling assumptions. Unlike the shaft or the rotating accessories, which can be approximated reasonably well through axisymmetric or quasi-axisymmetric representations, the casing requires a detailed three-dimensional description to capture its deformation shapes accurately. This difficulty is reflected clearly in the comparison between the experimental modal analysis of Chapter 5 and the numerical predictions of Chapter 7. Table 8.6 presents a comparison between the different configurations under investigation

Casing Modal Parameters				
Shape name	**Experimental frequency [Hz]**	**Numerical frequency Fourier [Hz]**	**Experimental damping [%]**	**Δf Fourier [%]**
Mode shape 1	3137	12486	4.744	-298.02
Mode shape 2	7197	14081	1.335	-95.65
Mode shape 3	7547	18123	1.325	-140.14
Mode shape 4	9325	Not detected	0.955	N/A
Mode shape 5	10547	Not detected	1.291	N/A

Table 8.6: Experimental and numerical modal parameters of the casing

Experimentally, several natural frequencies are observed in the range between approximately 3 kHz and 10 kHz, with the first mode appearing around 3.14 kHz. The measured modal shapes show significant compliance in the outer cylindrical wall and in the front and rear regions where geometric transitions occur. However, when the casing is modelled numerically, the first mode predicted by the Fourier-based model appears only at about 12.49 kHz, corresponding to an overestimation of nearly three hundred percent relative to the experiment. The second mode is overestimated by approximately ninety-six percent and the third by roughly one hundred and forty percent. The remaining experimental modes have no numerical counterparts, as the model predicts no additional modes below ten kilohertz. Taken together, these values indicate that the numerical casing is considerably stiffer than the real component throughout the entire frequency band of interest. The root cause of this discrepancy lies primarily in the modelling constraints imposed by the available tool. The software requires the casing to be represented as a homogeneous component, but the physical part is markedly

non-homogeneous: internal motor bars, cavities for cooling channels, and thickness transitions generate highly localised stiffness reductions that strongly influence its modal characteristics. In the experimental structure, these non-uniformities lead to compliant bending modes at relatively low frequencies; in the numerical model, the enforced homogeneity results in smoother, stiffer walls and an artificially increased structural rigidity. The simplified reverse-engineered geometry further amplifies this gap by smoothing out small features that, in reality, lower stiffness locally and contribute to the formation of flexible mode shapes. The correlation is further complicated by the casing's sensitivity to boundary effects. Although both the experimental and numerical analyses adopt nominally free–free conditions, their practical implementation differs significantly. In the experimental setup, the free–free condition is approximated an air-film cushion, which introduces small but non-negligible residual stiffness and damping, particularly affecting the lowest-frequency range. As a result, the rigid-body modes that would theoretically occur at zero frequency in an ideal free–free system appear in the experimental data as low-frequency modes. In contrast, the numerical model assumes perfectly free–free boundary conditions, leading to ideal rigid-body modes at zero frequency. This discrepancy can affect the correlation in the low-frequency range. While this factor does not fully explain the large deviations observed, it contributes to the mismatch in the first modal family. From a modal-shape standpoint, the disagreement is equally pronounced. The experimental casing exhibits bending modes characterised by substantial ovalisation and distortions of the cylindrical shell, whereas the numerical model produces stiffer, higher-order shapes dominated by more uniform curvature patterns. This suggests that the numerical mesh and material model fail to capture the structural anisotropy induced by the stator bars and local mass concentrations. Because these features are fundamental to the casing's real dynamic behaviour, their absence in the numerical representation produces modal shapes that cannot be reliably compared to the experimental ones. In summary, the casing is the component for which the numerical correlation is least satisfactory. The stiffness overprediction ranges from nearly one hundred percent to almost three hundred percent across the first experimental modes, and the numerical model fails to reproduce several important flexible modes altogether. These discrepancies arise from unavoidable modelling simplifications—material homogeneity, geometric averaging, and incomplete representation of internal structures—and highlight the need for a more detailed modelling strategy if the casing is to be used as a predictive element in future analyses. Despite these limitations, the system-level model still benefits from the casing representation in terms of mass distribution and overall constraint topology, although its dynamic fidelity remains limited when considered in isolation.

8.6 Spindle assembly

The spindle assembly represents the first configuration in which all major subsystems—the shaft, rotating accessories, bearings, and casing—interact simultaneously, thereby generating a dynamic behaviour that emerges not from the properties of individual components but from their combined stiffness, mass distribution, and coupling. For this reason, the spindle assembly constitutes the most meaningful benchmark for assessing whether the modelling assumptions adopted throughout this work succeed in reproducing the real mechanical behaviour of the system within the operational frequency range of interest. The comparison presented here relies on the experimental modal parameters obtained in Chapter 5 and the numerical eigenfrequencies predicted by the Fourier-shaft formulation, as reported in Chapter 7. Table 8.7 presents a comparison between the different configurations under investigation, specifically, red modes are axial, blue modes are radial.

Spindle Assembly Modal Parameters				
Shape name	**Experimental frequency [Hz]**	**Numerical frequency [Hz]**	**Experimental damping [%]**	**Δf %**
Mode shape 1	1372	1553	5.868	-13.19
Mode shape 2	2564	2835	2.902	-10.57
Mode shape 3	3498	Not detected	5.024	N/A
Mode shape 4	3726	Not detected	3.719	N/A
Mode shape 5	4158	4149	1.672	0.22
Mode shape 6	7585	5165	0.861	31.91
Mode shape 7	7767	7777	2.196	-0.13
Mode shape 8	9172	8453	1.581	7.84
Mode shape 9	9273	Not detected	1.558	N/A
Mode shape 10	9843	Not detected	1.604	N/A

Table 8.7: Experimental and numerical modal parameters of the spindle assembly

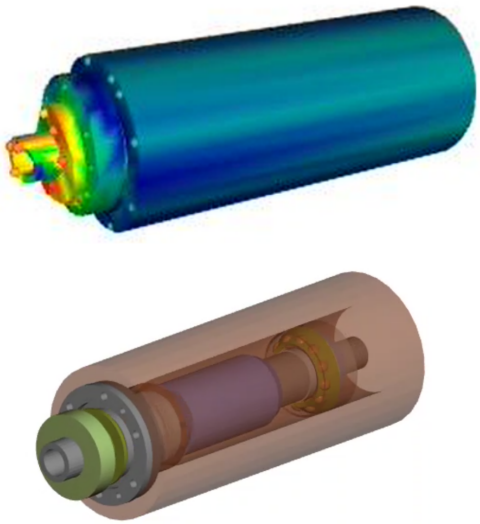


Figure 8.8: Spindle assembly - mode shape 1: comparison

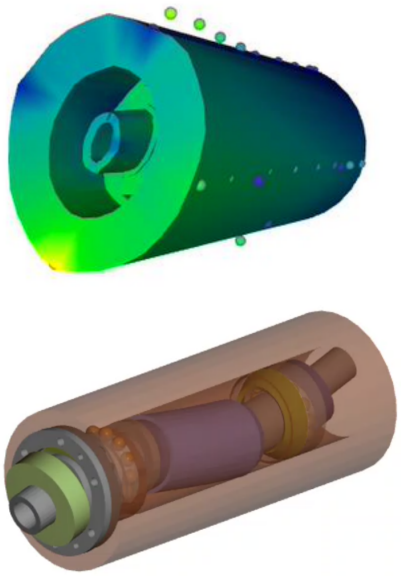


Figure 8.9: Spindle assembly - mode shape 8: comparison

Under free–free conditions, the experimental modal analysis identifies five dominant radial modes between approximately 2.56 kHz and 9.84 kHz. These modes represent global deformation patterns involving bending of the shaft inside the casing (Figure 8.9), local deflection of the bearings and housing, and distributed motion of the rotating accessories, all constrained by the complex boundary interactions between shaft, rings, springs, and housings. The numerical model predicts

a corresponding set of modes at 2.84 kHz, 4.15 kHz, 7.78 kHz, 8.45 kHz and 5.17 kHz. The agreement between the two sets is characterised by moderate deviations in the low and mid-frequency range, excellent matching around the mid-band, and a deterioration in accuracy near the upper limit of the experimental spectrum. The first radial mode is overestimated by roughly eleven percent, the second by a similar amount, while the third is reproduced with remarkable accuracy at less than one percent deviation. Beyond this point, the numerical stiffness begins to outweigh the experimental trend: the fourth mode is underestimated by nearly nine percent, and the highest experimental mode at 9.84 kHz is not represented convincingly, with the closest numerical prediction lying at a substantially lower frequency of around 5.17 kHz. Taken as a whole, these observations indicate that the model captures the global spindle behaviour reliably up to approximately eight kilohertz, beyond which the simplified casing and bearing interfaces limit the model's ability to represent higher-frequency dynamics. The axial family of modes provides complementary insight. Experimentally, five dominant axial modes appear between roughly 1.37 (Figure 8.8) kHz and 9.17 kHz, reflecting the combined compliance of the bearing arrangement, the axial preload mechanism, and the housing interfaces. The numerical model predicts the nearest corresponding modes at 1.55 kHz, 4.15 kHz, 5.17 kHz, 7.78 kHz and 8.45 kHz. Deviations are more pronounced than in the radial direction for the lower modes: the first axial mode is overestimated by about thirteen percent, the second by nineteen percent and the third by twenty-four percent. These discrepancies point to a modelling stiffness that exceeds the real axial compliance of the bearing interfaces. In contrast, the mid-band axial mode at 7.78 kHz is reproduced within approximately three percent, indicating that the model accurately captures the stiffer axial dynamics that dominate at higher frequencies. As with the radial case, the numerical representation of the highest axial mode tends to converge toward a slightly lower frequency, underestimating the experimental value by about eight percent. This behaviour reflects the cumulative effects of simplified bearing contacts, an idealised preload mechanism, and the overly rigid casing representation, all of which act to reduce the effective axial compliance that is present in the physical spindle. The modal-shape comparison further clarifies the origins of the frequency deviations. In both radial and axial directions, the numerical model reproduces the qualitative structure and ordering of the experimental modes, confirming that the primary deformation pathways—shaft bending, bearing tilting, and housing participation—are captured correctly. However, higher-frequency modes involving casing flexibility or complex interactions between inner and outer rings are less accurately represented, as the homogeneous casing model cannot reproduce the local softening caused by the stator bars and internal cavities. As a result, the numerical model tends to underestimate the deformation amplitude in regions where the experimental spindle exhibits significant local compliance, which explains why the highest families of radial and axial

modes are shifted downward in the numerical predictions. Taken together, these observations show that the numerical representation of the spindle assembly is robust and reliable in the frequency range most relevant for spindle operation. The deviations observed in the first three modes of each family remain within the range expected for industrial-grade modelling approaches, especially when operating under the constraints of fixed material homogeneity and reduced information on internal structures. The correlation weakens at higher frequencies—particularly above eight kilohertz—due to the compounded effects of modelling simplifications in the casing, the bearing interfaces and the preload system. Nevertheless, the model provides a sufficiently accurate representation of the spindle's dynamic behaviour to support sensitivity studies, boundary-condition selection and qualitative assessments of modal trends. The next section further investigates whether this predictive capability holds when the spindle is evaluated under rotating operational conditions.

8.7 Spindle in operation

The evaluation of the spindle under rotating conditions provides the most stringent and physically representative test of the numerical model, because it exposes the system to the combined influences of centrifugal loads, gyroscopic effects, evolving bearing contact conditions and thermally induced variations in stiffness. Unlike stationary modal analysis, which characterises the structure under idealised, zero-load conditions, the operational measurements presented in Chapter 5 capture the spindle's dynamic behaviour while it undergoes run-up, steady-state rotation at 60000rpm and subsequent coast-down. The comparison between these measurements and the numerically derived Campbell diagrams and operating deflection shapes (ODS) therefore reveals not only how well the numerical model predicts the intrinsic modal properties of the spindle, but also how accurately it reproduces the physical behaviour that emerges during real operation. Table 8.8 & 8.9 present a comparison between the different configurations under investigation, specifically, red shapes are radial, blue shapes are axial.

Spindle @0 rpm Modal Parameters					
Shape name	**Experimental frequency [Hz]**	**Numerical frequency beam shaft [Hz]**	**Numerical frequency Fourier shaft [Hz]**	**Δf beam [%]**	**Δf Fourier [%]**
Shape 1	1528	1331	1553	13	-2
Shape 2	2344	2673	2832	-14	-21
Shape 3	3585	3669	Not detected	-2	N/A
Shape 4	3720	3818	4142	-3	-11
Shape 5	7681	4973	5159	35	33
Shape 6	7805	Not detected	Not detected	N/A	N/A
Shape 7	9164	8646	8646	6	6
Shape 8	9487	Not detected	Not detected	N/A	N/A

Table 8.8: Experimental and numerical modal parameters of the spindle at 0 rpm

Spindle @60000 rpm Modal Parameters					
Shape name	**Experimental frequency [Hz]**	**Numerical frequency beam shaft [Hz]**	**Numerical frequency Fourier shaft [Hz]**	**Δf beam [%]**	**Δf Fourier [%]**
Shape 1	1528	879	1000	42.474	34.555
Shape 2	2344	1696	1835	27.645	21.715
Shape 2	2344	1699	1840	27.517	21.502
Shape 3	3585	2202	2386	38.577	33.445
Shape 3	3585	2202	2436	38.577	32.050
Shape 4	3720	2262	3999	39.194	-7.500
Shape 4	3720	3669	4150	1.371	-11.559
Shape 5	7681	4037	6089	47.442	20.726
Shape 5	7681	4260	6089	44.538	20.726
Shape 6	7805	8027	7494	-2.844	3.985
Shape 6	7805	8639	Not detected	-10.685	N/A
Shape 7	9164	Not detected	7855	N/A	14.284
Shape 7	9164	Not detected	8171	N/A	10.836
Shape 8	9487	Not detected	Not detected	N/A	N/A

Table 8.9: Experimental and numerical modal parameters of the spindle at 60000 rpm

During operation, the spindle exhibits distinct radial and axial response families, each characterised by frequency lines that evolve with rotational speed. In the radial direction, several prominent operational frequencies are experimentally identified at approximately 2.34 kHz, 3.59 kHz, 7.81 kHz and 9.16kHz. These are associated with global bending of the rotating assembly, interactions between shaft and casing, and, at higher frequencies, more complex deformation patterns involving bearings and localized casing flexibility. The numerical model, evaluated using the Fourier-shaft formulation, predicts the closest corresponding operational shapes at roughly 2.83 kHz, 4.14 kHz, 8.45 kHz and 6.09 kHz. The deviations for the first three radial

shapes range from about eight to twenty-one percent, reflecting a moderate but systematic tendency of the numerical model to overestimate structural stiffness under rotating conditions. This behaviour is consistent with earlier observations in the stationary spindle configuration, where the first radial families were reproduced with reasonable fidelity but progressively diverged from experimental measurements at higher frequencies. Notably, the highest experimental radial ODS at 9.16 kHz is significantly underestimated numerically, with the closest prediction occurring near 6.09 kHz. This suggests that the numerical representation of the casing and the bearing interfaces remains too stiff in the operational regime, especially when gyroscopic and centrifugal effects should induce additional compliance that the model does not fully capture. A further aspect emerges when examining the relationship between experimental and numerical operational frequencies under rotation. In some cases, the experimental ODS reveals two identical or nearly identical frequencies associated with distinct deformation patterns, whereas the numerical model predicts these same shapes at two clearly different frequencies. This behaviour is not indicative of an inconsistency but reflects a physical phenomenon inherent to rotating systems. When the spindle rotates at high speed, gyroscopic coupling, centrifugal softening, anisotropic contact conditions within the bearings and preload-dependent effects introduce directional stiffness differences that do not exist under stationary conditions. Mechanically, this means that two deformation patterns that are degenerate in the non-rotating spindle—typically corresponding to bending in orthogonal directions—are no longer dynamically equivalent once rotation is imposed. Rotation breaks the symmetry of the system and causes a frequency splitting of modes that would otherwise share the same natural frequency. The numerical model, which evaluates the system at discrete rotational speeds, naturally captures this orthogonal-direction asymmetry, producing two distinct operational frequencies where the experiment identifies a single, speed-dependent line. The difference arises because the experimental identification clusters close-lying peaks into a single observed frequency, while the numerical model resolves them separately. This effect confirms that the model correctly incorporates the directional anisotropy induced by rotation, even if residual discrepancies persist at higher frequencies. The axial operational response displays a more encouraging correspondence. Experimentally, axial ODS peaks are observed at approximately 1.53 kHz, 3.72 kHz, 7.68 kHz and 9.49 kHz. The numerical model predicts nearest axial counterparts at about 1.55 kHz, 4.14 kHz, 8.45 kHz and 6.09 kHz. The lowest axial peak is matched extremely well, with a deviation of less than two percent. The subsequent axial modes in the mid-frequency range exhibit deviations on the order of ten percent, which remains satisfactory given the inherent uncertainties associated with the bearing contact model, the preload implementation and the absence of speed-dependent lubricant effects in the simulation. The highest axial operational peak, however, exhibits a substantial mismatch: the experimental 9.49

kHz frequency is again paired numerically with a shape near 6.09 kHz. This systematic underestimation at the upper end of the spectrum mirrors the discrepancy observed in the radial direction and again points to the combined influence of bearing-housing interactions, casing compliance and rotational effects that are not fully represented in the numerical formulation. The Campbell diagram comparison reinforces these observations. The numerical Campbell diagram generated using the Fourier model captures the correct qualitative evolution of frequency lines with speed, including the rise of bending-related modes and the relative stability of high-frequency modes associated with localised stiffness. The experimental Campbell diagram likewise presents a clear separation between speed-dependent and speed-independent components. However, the slope and curvature of the numerical frequency trajectories do not fully match the experimental ones. In particular, the numerical model overpredicts the influence of gyroscopic stiffening on the lower radial modes and underpredicts the softening trends that appear at high frequencies in the experimental measurements. Thermal effects, centrifugal expansion of the inner ring, lubricant shear thinning, and preload relaxation during operation all contribute to these experimentally observed softening mechanisms, which are not incorporated in the present numerical model. As a consequence, the numerical Campbell diagram captures the structural logic of the operational behaviour but lacks the detailed speed-dependent fidelity required to reproduce the high-frequency operational peaks. Despite these discrepancies, the numerical ODS shapes remain qualitatively consistent with the experimental ones. Both reveal global bending patterns at low frequency that transition into mixed shaft–bearing–casing modes in the mid-band, and become increasingly influenced by localised casing flexibility at higher order. The numerical shapes, however, tend to underestimate the deformation amplitude near the casing's outer wall and overestimate stiffness near the bearing interfaces. This again traces back to the casing representation, which lacks the internal structural discontinuities that produce significant local compliance under experimental conditions. As a result, the numerical operational shapes correctly replicate the overall deformation patterns and the ordering of the principal families but deviate in the localisation and intensity of the deformation fields at higher frequencies. Altogether, the comparison under rotating conditions demonstrates that the numerical model is able to reproduce the essential operational behaviour of the spindle, especially in terms of mode ordering, deformation patterns and the lower-frequency axial response. The correlation weakens in the upper frequency range for both radial and axial families, highlighting the limitations of the current modelling assumptions regarding casing flexibility, bearing contact realism and speed-dependent effects such as centrifugal softening and thermal interactions. Nevertheless, the model remains sufficiently accurate to support dynamic interpretation, sensitivity studies and methodological validation for the frequency range most relevant to spindle operation. Its performance under rotation confirms the

trends already established in the stationary configurations and provides a coherent foundation for the future developments proposed in the next chapter.

8.8 Overall assessment

The comparative analysis conducted across all levels demonstrates that the numerical model succeeds in reproducing the fundamental dynamic behaviour of the spindle over the frequency range most relevant for its operation, while revealing limitations that stem from modelling assumptions and structural simplifications intrinsic to the current simulation framework. At component level, the shaft provides a robust baseline: the Fourier-based formulation reproduces the first bending families with deviations confined to single-digit percentages and essentially matches the second bending mode, confirming that the inclusion of circumferential and through-thickness compliance is necessary to obtain realistic bending behaviour. The beam formulation remains usable for qualitative assessments but exhibits a systematic stiffness bias, consistent with its one-dimensional nature. The accessory components present a heterogeneous but physically interpretable level of agreement. The ring correlates almost exactly with the experimental results, the bushing exhibits only a modest underestimation of about -6.5%, and the bezel shows larger discrepancies at higher frequencies due to its geometric sensitivity and the smoothing inherent in a homogeneous representation. Since these modes all reside well above the spindle's operational band, their imperfect correlation has limited impact on system-level fidelity, even though they foreshadow the difficulties encountered at high frequency once the casing becomes dynamically active. The rotating subassembly composed of the shaft and its accessories confirms the same trends: the Fourier model offers a closer reproduction of the radial response and preserves correct modal ordering, whereas the beam formulation shows a residual stiffness imbalance. However, a methodological limitation emerges at this stage: the software cannot compute axial vibration modes for the rotating components when no axial stiffness elements are defined. This absence prevents a full comparison between numerical and experimental axial families and leaves a portion of the dynamic behaviour unexplored. It also highlights the importance of bearing interfaces and axial preload mechanisms, which are introduced only at the spindle-assembly level. The casing remains the component with the least satisfactory correlation. The enforced material homogeneity, combined with the smoothing of internal structures and the absence of stator-bar heterogeneity, yields an over-rigid numerical shell, shifting the first modal families several kilohertz above their experimental counterparts. This discrepancy removes key low-frequency modes from the numerical spectrum and affects the accuracy of assembly-level predictions in the higher bands where casing participation becomes prominent. Although the model still contributes mass

and boundary geometry appropriately, its structural fidelity at low frequency is insufficient for quantitative prediction. The assembled spindle under stationary conditions demonstrates that the model captures the global stiffness topology and the dominant interaction pathways between shaft, bearings and housing. The radial modes up to approximately eight kilohertz are reproduced with small to moderate deviations, while the axial modes present systematic overestimation in the lower families and closer agreement in the mid-band. The highest modes tend to be underestimated, consistent with the combined effects of idealised bearing tilting stiffness, simplified preload representation and the overly rigid casing. At this stage, the analysis also reveals a second methodological limitation: the absence of a fully decoupled analysis separating shaft and casing motion. Such an analysis—experimentally available through casing-to-shaft and shaft-to-casing transfer functions—would have enabled a clearer attribution of discrepancies to either the rotor or the housing. Its omission does not compromise the overall assessment but leaves certain high-frequency interactions less precisely characterised. Under rotating conditions, the qualitative structure of the Campbell diagram and the deformation patterns of the operating deflection shapes are reproduced convincingly. The lowest axial operational line is matched with excellent accuracy, and the mid-band operational shapes remain within a physically reasonable deviation. The deterioration of accuracy at the upper end of the spectrum is consistent with the absence of speed-dependent effects—such as centrifugal softening, lubricant shear thinning, thermal growth, and preload relaxation—which are all clearly present in the experimental response but absent from the current numerical formulation. The numerical splitting of deformation patterns that appear degenerate experimentally confirms that the model captures the anisotropy introduced by rotation, even if the precise quantitative values remain imperfect. Overall, the modelling strategy adopted in this work achieves a coherent balance between computational tractability and physical realism. The model is reliable for modal trend interpretation, design screening and qualitative decision-support across the operationally relevant bandwidth. Its limitations are clearly delineated: incomplete axial modelling in the rotating-components configuration, absence of shaft–casing decoupling in the numerical workflow, insufficient representation of casing heterogeneity, simplified bearing–housing contact mechanics, and the lack of speed-dependent or thermal effects. Addressing these aspects would transform the current qualitative agreement at high frequency into quantitative predictive capability. The improvement roadmap discussed in Chapter 9 provides the logical next steps to advance the numerical model into a fully predictive simulation framework suitable for high-fidelity spindle-dynamics analysis.

Chapter 9

Future developements

The comparison between experimental and numerical results presented in the previous chapter has demonstrated that the current modelling framework captures the essential dynamic behaviour of the spindle across the lower and mid-frequency ranges, while also revealing several systematic limitations that constrain its predictive accuracy, particularly in the higher modes and under rotating operational conditions. These limitations do not undermine the overall value of the numerical model, which has proven sufficiently reliable for trend interpretation, boundary-condition selection and qualitative assessment of modal behaviour below approximately 8kHz. Nonetheless, the deviations observed in the casing, the incomplete representation of axial compliance, the simplified treatment of bearing contacts and preload mechanics, and the absence of speed-dependent physical effects indicate clear avenues for further refinement. The improvements outlined in this chapter are therefore not merely optional enhancements, but well-defined and technically justified developments that would significantly increase the model's realism and extend its applicability to a broader range of operating scenarios.

As observed in the rotating-components configuration, the system exhibits a strong anisotropy in stiffness, with the axial stiffness being significantly higher than the radial one. As a result, axial modes are not absent in the numerical model, but they occur at much higher frequencies compared to radial modes. This leads to a modal description that is effectively dominated by radial dynamics within the frequency range of interest. Consequently, axial deformation patterns, although present, remain less relevant for the current analysis due to their high-frequency nature.

Similarly, the ability to separate axial and radial vibration modes in a systematic and automated manner would considerably strengthen the diagnostic value of the numerical results. In the current workflow, the two families can be distinguished only through manual inspection of mode shapes, a process that becomes cumbersome and increasingly ambiguous when higher-order or mixed modes are present.

Allowing the software to perform a clean separation between axial and radial modal components would not only align the numerical output more closely with experimental classification practices, but would also facilitate automated correlation, clustering and trend evaluation across multiple spindle configurations. Beyond mode identification, a key development involves the ability to model components while accounting for their relative motions. Many discrepancies observed in the assembly-level comparison, especially in the axial direction, originate from the fact that the current model implicitly assumes perfectly rigid coupling along interfaces that, in reality, experience finite relative displacement. Bearings, for example, do not transmit axial and radial loads in the same manner, nor do their inner rings behave as monolithic constraints when loaded dynamically. Allowing the modelling environment to represent controlled relative motions between components would make it possible to simulate micro-slip, tolerances, geometric clearance and the compliance associated with real assembly conditions. This enhancement would directly improve the accuracy of predicted bearing tilting modes and the lower-frequency axial behaviour of the spindle. A further set of developments concerns the representation of non-uniform material properties, a limitation that was particularly evident in the casing. As demonstrated by the substantial over-prediction of casing stiffness—sometimes by nearly three hundred percent—the assumption of material homogeneity suppresses local softening mechanisms associated with the stator bars, internal cavities and thickness gradients. Enabling the software to model components with spatially varying properties would make it possible to replicate the complex stiffness landscape of the real casing and, consequently, to reproduce the low-frequency flexible modes that are entirely absent in the present numerical representation. Finally, a specific improvement concerns the modelling of the inner-ring contacts within the bearings. The present framework treats the inner rings as if they could penetrate one another when modelling stacked configurations or when applying certain types of preload, a simplification that significantly distorts the real stiffness distribution and can lead to inaccurate prediction of axial and tilting modes. A refined contact formulation that enforces non-penetration between inner rings would capture the real load-transfer mechanism and would enable a more accurate representation of the effects of bearing preload, spring compression and the axial freedom of the non-locating support group. This enhancement would address several of the persistent deviations identified in both axial modal families and operating deflection shapes.

The analysis presented in these chapters outline a coherent and technically grounded roadmap for future developments that would significantly improve the predictive accuracy, physical realism and methodological robustness of the numerical modelling framework used throughout this work. The comparison conducted in Chapter 8 has shown that the current implementation is capable of reproducing the essential dynamic behaviour of the spindle across the lower and mid-frequency

ranges, while also exposing systematic limitations that arise from simplified stiffness representations, idealised contacts, homogeneous material assumptions and the restricted capability of the software to capture certain deformation mechanisms. The developments proposed here directly address these limitations and stem from clear, experimentally verified discrepancies identified across all component and assembly configurations. A central theme emerging from these chapters is the necessity to extend the modelling capabilities beyond the present stiffness-driven constraints. The inability to compute modal behaviour in directions where the system exhibits negligible intrinsic stiffness prevents the identification of compliant or near-rigid-body modes that are nevertheless dynamically relevant. Similarly, the absence of an automated and robust distinction between axial and radial vibration families complicates the interpretation of both numerical and experimental results, especially when mixed or coupled modes arise. Enhancing the software to perform modal analysis in low-stiffness directions and to classify vibration families would therefore improve the completeness and clarity of the modal representation, facilitating a more rigorous and fully consistent correlation process. The need to model relative motion between components represents another key direction for improvement. Many of the discrepancies identified in the lower-frequency axial modes of the spindle assembly originate from the assumption of perfectly rigid coupling between parts that, in reality, exhibit finite relative displacement due to local compliance, geometric clearances or preload mechanisms. Enabling the modelling environment to incorporate controlled relative motion would make it possible to simulate bearing tilting behaviour more accurately, to reproduce the compliance of the preload system and to capture the micro-interactions between rings, spacers, springs and housings that characterise real spindle assemblies. These advancements would directly enhance the correlation of both axial modes and mixed deformation patterns. Equally important is the capability to represent components with non-uniform material properties. The casing, in particular, exhibited substantial differences between experimental and numerical results, chiefly because the current tool enforces a homogeneous material distribution that suppresses the local softness introduced by the stator bars, cooling channels and geometric transitions. Enabling the software to incorporate spatially varying stiffness, density or damping would dramatically improve the fidelity of casing simulations and allow numerical models to reproduce the low-frequency flexible modes that were entirely absent in the current representation. This development would also enhance the accuracy of assembly-level predictions, as casing flexibility plays a crucial role in shaping the higher-order radial and axial response. The refinement of inner-ring contact modelling represents a final, highly targeted improvement. The current simulation environment allows partial penetration between inner rings under certain preload and support configurations, a simplification that affects the load-transfer mechanism and leads to inaccuracies in axial and tilting modes. Implementing

a more realistic non-penetration constraint between inner rings would not only improve the physical fidelity of the bearing model but would also enhance the accuracy of the spindle's axial stiffness distribution, particularly under preload or mixed loading conditions. This refinement would address several of the persistent deviations observed in both stationary and rotating configurations.

Beyond these specific technical enhancements, a fundamental objective for future development concerns the robustness and cross-functional scalability of the software. The high-speed spindle represents the ideal starting point for initial model tuning: its extreme structural stiffness, the use of super-precision bearings, and its role in finishing applications—characterized by high rotational speeds and low torque—provide a controlled environment for validating dynamic behavior. However, a truly resilient modeling framework must demonstrate operational versatility toward the opposite extreme: the standard industrial electric motor used in heavy-duty applications, such as suction pumps or ventilation fans. Transitioning to such assets involves a shift toward high-torque, low-speed regimes with less precise assembly tolerances. Unlike the near-ideal conditions of a spindle, industrial motors often employ a combination of clearance-fit and preloaded bearings, complicating modal identification. Furthermore, operating in harsh environments introduces variables like lubricant contamination from external particles, which renders standard shielding ineffective and makes high preload a liability due to the increased risk of bearing seizure. Incorporating the ability to simulate these degraded or non-ideal boundary conditions is essential for transforming the framework into a universal analytical platform.

Collectively, the developments proposed in this chapter form a coherent progression aimed at increasing the depth, flexibility and physical accuracy of the modelling framework. They emerge organically from the correlation results and reflect a balanced combination of methodological refinement, physical realism and practical applicability. Implementing these enhancements would substantially reduce the gap between numerical predictions and experimental behaviour, particularly in the higher-frequency bands and under operational rotation. More importantly, they would provide users of the modelling tool with the capability to perform truly predictive analyses, enabling more reliable design decisions, improved bearing-housing interface calibration and a deeper understanding of the coupled dynamics governing high-speed spindle behaviour.

Chapter 10

Conclusions

The work presented in this thesis has addressed one of the most persistent challenges in spindle dynamics: establishing a consistent and physically meaningful correlation between numerical predictions and experimental evidence for a high-speed spindle operating under actual boundary conditions. By combining an extensive modal testing campaign with a structured numerical analysis conducted within the SKF SimPro environment, this study has demonstrated both the potential and the inherent limitations of current modelling approaches when applied to systems in which bearing behaviour, preload mechanisms, casing flexibility and assembly details interact in a non-trivial manner.

The experimental campaign, articulated across isolated components, rotating sub-assemblies and the complete spindle in both stationary and operational conditions, has provided a robust and reliable dataset capable of capturing the true dynamic behaviour of the system. The adoption of free–free boundary conditions, validated sensor layouts and roving-hammer excitation allowed the extraction of modal parameters with high repeatability and physical consistency. The additional investigation performed on the rotating spindle, through Campbell diagram analysis and operating deflection shapes, offered essential insight into speed-dependent effects such as gyroscopic coupling, harmonic excitations and the deformation patterns active under real working conditions. These results formed a comprehensive and trustworthy reference against which the numerical model could be assessed.

The numerical model, constructed in SKF SimPro Expert, reproduced many of the dynamic features observed experimentally, particularly in the low- and mid-frequency ranges. The Fourier-based shaft formulation proved indispensable for capturing the correct bending behaviour of the rotor and for achieving close agreement with experimental data, especially in the first modal families of the shaft and the rotating components. The more simplified beam formulation, while computationally efficient, systematically overestimated stiffness and was therefore less representative of the physical system. The analysis also confirmed that accessory

components such as the ring and the bushing are reproduced with good accuracy, whereas more geometrically intricate parts such as the bezel exhibit deviations at higher frequencies, although these do not significantly influence the dynamic behaviour within the operational range.

The most critical source of discrepancy emerged from the model of the casing. Due to the software's constraint of assigning homogeneous material properties and the unavoidable geometric simplifications introduced during reverse engineering, the numerical representation of the casing was found to be substantially stiffer than the experimental one. This mismatch suppressed several flexible modes identified experimentally and propagated into the assembly-level predictions, particularly at higher frequencies where casing compliance becomes increasingly relevant. Despite this, the global dynamic trends of the spindle assembly were captured with reasonable fidelity, and the numerical model reproduced the correct modal order and deformation patterns for most of the frequency range of interest.

Under rotating conditions, the numerical model successfully captured the qualitative evolution of natural frequencies with speed and reproduced the primary operational deformation shapes. The differences observed at high frequency were consistent with the absence of centrifugal softening, thermal effects and lubrication-dependent stiffness variations, all of which are intrinsically present in the experiment but not currently included in the numerical formulation. These discrepancies highlight the importance of incorporating speed-dependent mechanisms in future developments of the software environment.

Overall, this thesis has demonstrated that the numerical model developed using SKF SimPro can reliably reproduce the dominant modal behaviour of the spindle when appropriate modelling strategies—particularly the use of the Fourier-based shaft formulation and physically consistent boundary conditions—are employed. At the same time, the work has clearly identified the methodological limitations that hinder full quantitative agreement, especially concerning casing flexibility, axial compliance, bearing–housing interactions and load-dependent dynamic effects. By clarifying these aspects through a rigorous comparison with comprehensive experimental evidence, the thesis provides a solid foundation for future improvements in modelling practices and software capabilities.

Ultimately, the contributions of this work extend beyond the specific spindle analysed. They define a general methodological framework for correlating experimental and numerical modal analyses of high-speed rotating systems, emphasising the importance of boundary condition modelling, hierarchical validation, and the combined interpretation of stationary and operational data. The results confirm that accurate prediction of spindle dynamics cannot rely solely on detailed component models, but must instead consider the coupled behaviour of bearings, housings and preload mechanisms as an integrated and physically coherent system. In this sense, the work highlights both the strengths of current modelling tools and the

developments required to achieve the level of predictive accuracy demanded by next-generation high-precision applications.

Appendix A

Geometrical characterization of the components

In order to enable the accurate modeling of the entire system, first within the ArtemiS Suite software and subsequently in SimPro Expert, an appropriate geometrical characterization of all system components is required. Each component was then weighed to determine the total mass of the vibrating assembly. The following section presents the characteristic dimensions of each component along with their respective positions on the shaft.

A.1 Ring

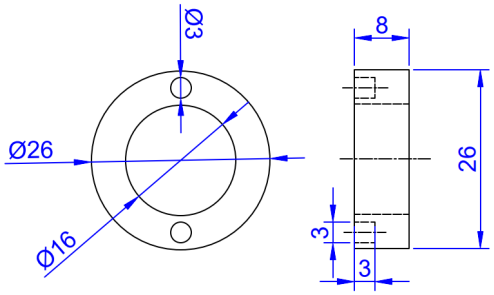


Figure A.1: Front and side view of the ring

Parameter	Value
Thickness (s)	8 mm
Inner Diameter (d_{in})	16 mm
Outer Diameter (d_{out})	26 mm
Grooves pitch (p)	21 mm
Groove Diameter (d_{g})	3 mm
Groove Width (g)	2.8 mm
Thread Type	M16 × 0.75
Weight	18.65 g

Table A.1: Geometrical and Physical Specifications of the Ring (NDE)

A.2 Bearing

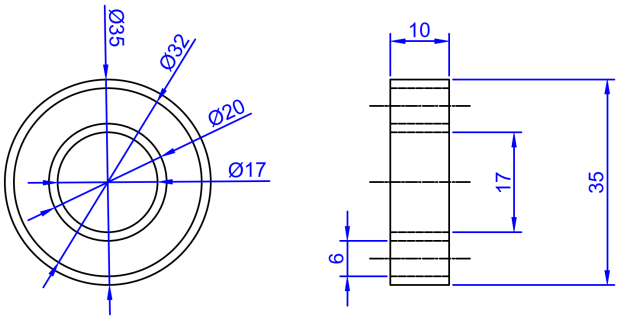


Figure A.2: Front and side view of the bearing

SKF SP-7003 CE-RZ/1	
Parameter	**Value**
Thickness (s)	10 mm
Inner Diameter (d_{in})	17 mm
Outer Diameter (d_{out})	35 mm
Number of balls (N)	12
Weight	36.33 g

Table A.2: Geometrical and Physical Specifications of the Bearing

A.3 Bezel

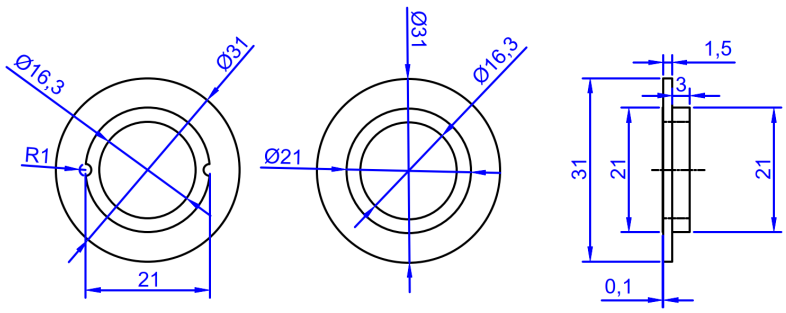


Figure A.3: Front, back and side view of bezel

Parameter	Value
Outer Diameter (D_{out})	31 mm
Delevated (D_{elevated})	21 mm
Inner Diameter (D_{in})	16.3 mm
Radius (r)	2 mm
s_1	0.1 mm
s	1.5 mm
s_2	3 mm
Weight	9.46 g

Table A.3: Geometrical and Physical Specifications of the Bezel

A.4 Bushing

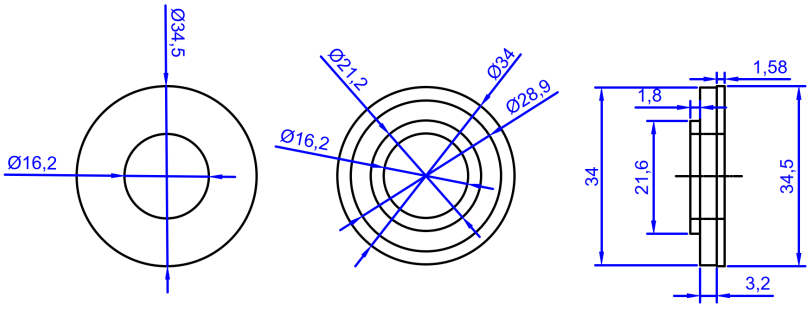


Figure A.4: Front, back and side view of the bushing

Parameter	Value
Outer Diameter (D_{out})	34.5 (mm)
Inner Diameter (D_{in})	16.2 (mm)
Outer Diameter (dout)	34 (mm)
Inner Diameter (din)	21.2 (mm)
Inner Diameter Back ($d_{\text{in_back}}$)	28.9 (mm)
Thread Thickness (s_{thread})	3.2 (mm)
Inner Thickness (s_{in})	1.7 (mm)
s_1	1.5 (mm)
s_c	8.2 (mm)
Thread	M34 × 0.9
Weight	30.26 (g)

Table A.4: Geometrical and Physical Specifications of the Bushing

A.5 Flange

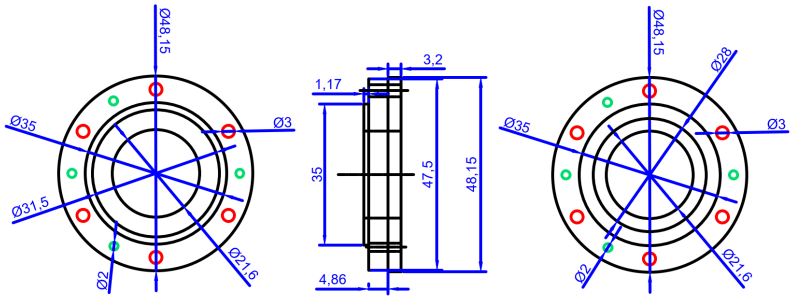


Figure A.5: Front, back and side view of the flange

Parameter	Value
Outer Diameter (D_{out})	48.15 (mm)
Median Diameter (D_{med})	35 (mm)
Inner Diameter (D_{in})	21.6 (mm)
Thickness (t)	3.5 (mm)
Outer Thread Diameter (d_{ot})	17.9 (mm)
d_1	35 (mm)
d_2	31.5 (mm)
Inner Diameter (din)	21.6 (mm)
s_1	3.2 (mm)
s_2	4.86 (mm)
Total Thickness (s_{tot})	9.23 (mm)
Weight	73.4 (g)

Table A.5: Geometrical and Physical Specifications of the Flange

A.6 Spring

The spring system consists of two rings: the first features 18 holes, each housing an elastic element (in our case, helical springs), while the second is a thin ring—almost comparable to a hollow disk—designed to adjust the applied preload. In the configuration under analysis, only 10 helical springs are employed out of the 18 available seats, as illustrated in the two figures below (Figure A.6 & Figure A.6.

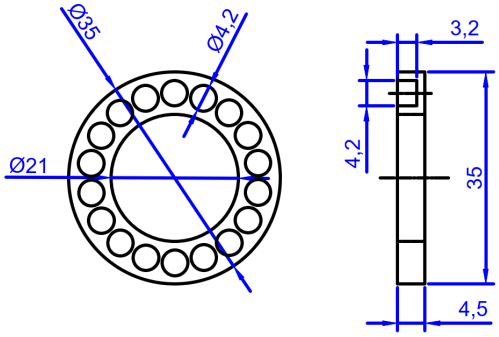


Figure A.6: Caption

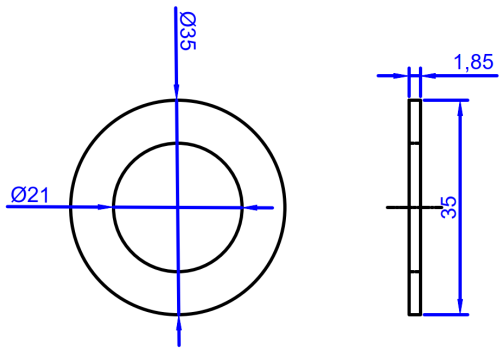


Figure A.7: Front and side view of the ring

A.7 Shaft

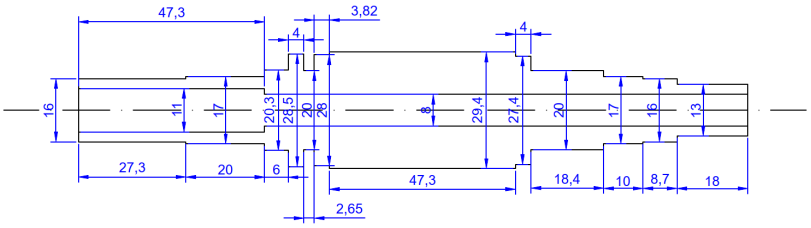


Figure A.8: Cross section of the shaft

Section (x in mm)	Diameter (mm)	Bore diameter (mm)
$0 < x < 21{,}6$	16	11
$21{,}6 < x < 27{,}3$	16	11
$27{,}3 < x < 47{,}3$	17	11
$47{,}3 < x < 53{,}3$	20.3	8
$53{,}3 < x < 57{,}3$	28.5	8
$57{,}3 < x < 59{,}95$	20	8
$59.95 < x < 63.77$	28	8
$63{,}77 < x < 111.07$	29.4	8
$111.07 < x < 115{,}07$	27,4	8
$115{,}07 < x < 133{,}47$	20	8
$133{,}47 < x < 143{,}47$	17	8
$143{,}47 < x < 145{,}37$	16	8
$145{,}37 < x < 152{,}17$	16	8
$152{,}17 < x < 170{,}17$	13	8

Total length 170,17 mm and **Weight:** 376,81 g

A.8 Casing

The casing has a cylindrical shape and is composed by three sub-units, namely a cup, a cylinder and an electric motor.

A.8.1 Cup

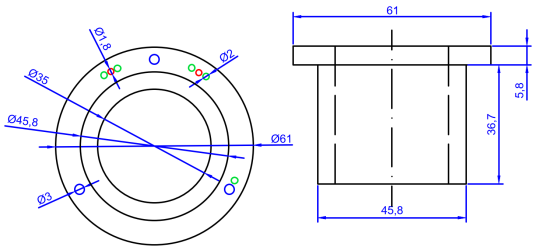


Figure A.9: Front and side view of the cup

Parameter	**Value**
Outer Diameter (D_{out})	61 (mm)
Inner Diameter (D_{in})	35 (mm)
Total Length (L_{tot})	42.5 (mm)
s_1	5.8 (mm)
Median Diameter (D_{m})	45.8 (mm)
Weight	308.73 (g)

Table A.6: Geometrical and Physical Specifications of the Cup

A.8.2 Cylinder

ADD TABLE

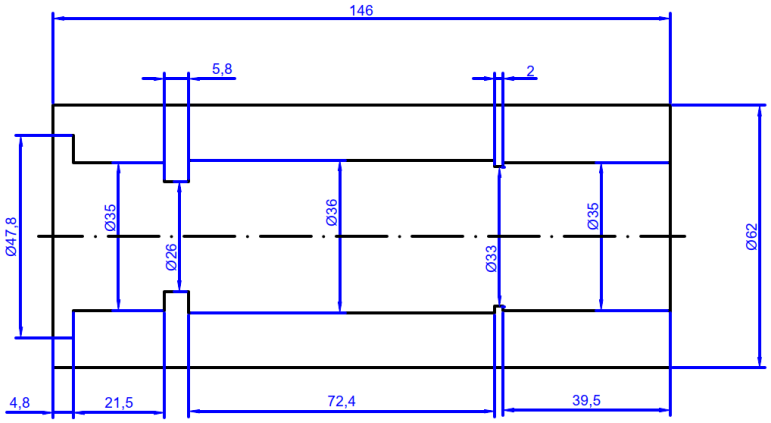


Figure A.10: Cylinder cross section

A.8.3 Electric Motor

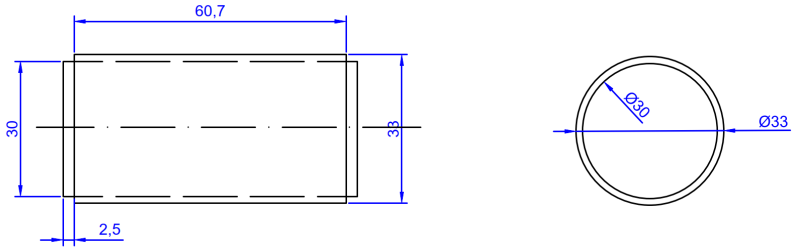


Figure A.11: Side and top view of the electric motor

Parameter	**Value**
Length (L)	65.7 (mm)
L_1	– (mm)
Inner Diameter (D_{in})	47.85 (mm)
Outer Diameter (D_{out})	29.5 (mm)
Number of Bars (n_{bars})	24
Weight	387.56 (g)

Table A.7: Geometrical and Physical Specifications of the Electric Motor

Bibliography

[1] *Analisi modali: spettro di risposta e risposta in frequenza*. Pagina tecnica. Astra Research s.r.l. URL: https://www.astraresearch.it/modali-risposta-in-frequenza/ (visited on 02/05/2026) (cit. on p. 15).

[2] D. J. Ewins. *Modal Testing: Theory, Practice and Application*. 2nd ed. Baldock, Hertfordshire: Research Studies Press, 2000 (cit. on p. 15).

[3] N. M. M. Maia and J. M. M. Silva. *Theoretical and Experimental Modal Analysis*. Baldock, Hertfordshire: Research Studies Press, 1997 (cit. on p. 15).

[4] *Model 352A25 ICP® Accelerometer – Datasheet*. Technical Datasheet. PCB Piezotronics, Inc. 2023. URL: https://www.pcb.com/contentStore/docs/pcb_corporate/vibration/products/specsheets/352a25_b.pdf (visited on 02/05/2026) (cit. on p. 21).

[5] *KS78C100 Miniature IEPE Accelerometer – Datasheet*. Technical Datasheet. MMF – Metra Mess- und Frequenztechnik. 2023. URL: https://mmf.de/wp-content/uploads/2023/08/ks78c100_en.pdf (visited on 02/05/2026) (cit. on p. 22).

[6] *Impact Hammers – Selection Guide and Technical Manual*. Product Technical Manual. PCB Piezotronics, Inc. 2022. URL: https://www.pcb.com/contentstore/MktgContent/LinkedDocuments/Force-Torque/TM-FRC-Impact-Hammers_Lowres.pdf (visited on 02/05/2026) (cit. on p. 23).

[7] Jeroen Anton Wensing. «On the Dynamics of Ball Bearings». Ph.D. dissertation. PhD thesis. Enschede, The Netherlands: University of Twente, Dec. 1998. ISBN: 90-36512298. URL: https://ris.utwente.nl/ws/portalfiles/portal/6075232/t000000d.pdf (cit. on p. 62).

[8] S. Berrada. «Développement d'une approche axée sur l'application pour établir une nouvelle spécification vibratoire des roulements appliquée au powerpack des véhicules électriques». French. Ph.D. dissertation. France: INSA Centre Val de Loire, 2024. URL: https://theses.fr/2024ISAB0007 (visited on 02/05/2026) (cit. on p. 70).